STATE ESTIMATION FOR AUTONOMOUS FLIGHT IN CLUTTERED ENVIRONMENTS

A DISSERTATION
SUBMITTED TO THE DEPARTMENT OF AERONAUTICS AND ASTRONAUTICS
AND THE COMMITTEE ON GRADUATE STUDIES
OF STANFORD UNIVERSITY
IN PARTIAL FULFILLMENT OF THE REQUIREMENTS
FOR THE DEGREE OF
DOCTOR OF PHILOSOPHY

Jacob Willem Langelaan
March 2006

I certify that I have read this dissertation and that, in my opinion, it is fully adequate in scope and quality as a dissertation for the degree of Doctor of Philosophy.

Stephen M. Rock
(Principal Adviser)

I certify that I have read this dissertation and that, in my opinion, it is fully adequate in scope and quality as a dissertation for the degree of Doctor of Philosophy.

Sanjay Lall

I certify that I have read this dissertation and that, in my opinion, it is fully adequate in scope and quality as a dissertation for the degree of Doctor of Philosophy.

Claire Tomlin

Approved for the University Committee on Graduate Studies.

Abstract

SAFE, AUTONOMOUS OPERATION in complex, cluttered environments is a critical challenge facing autonomous mobile systems. The research described in this dissertation was motivated by a particularly difficult example of autonomous mobility: flight of a small Unmanned Aerial Vehicle (UAV) through a forest. The focus was on enabling the three critical tasks that comprise flight: (1) maintaining controlled flight while avoiding collisions (*aviate*); (2) flying from a known start location to a known goal location (*navigate*); and (3) providing information about the environment– a map– to a human operator or other robots in the team (*communicate*).

In cluttered environments (such as forests or natural and urban canyons) signals from navigation beacons such as GPS may be frequently occluded. Direct measurements of vehicle position are therefore unavailable. Additionally, payload limitations of small UAVs restrict both the mass and physical dimensions of sensors that can be carried on board.

This dissertation describes the development and proof-of-concept demonstration of a navigation system that uses only a low-cost inertial measurement unit and a monocular camera. Micro electromechanical inertial measurements units (IMUs) are well suited to small UAV applications and provide measurements of acceleration and angular rate. However, they do not provide information about nearby obstacles (needed for collision avoidance) and their noise and bias characteristics lead to unbounded growth in computed position. A monocular camera can provide bearings to nearby obstacles and landmarks. These bearings can be used both to enable obstacle avoidance and to aid navigation.

Presented here is a solution to the problem of estimating vehicle state (its position, orientation and velocity) as well as the positions of obstacles or landmarks in the environment using only inertial measurements and bearings to landmarks. This is a highly nonlinear estimation problem, and standard estimation techniques such as the Extended Kalman Filter (EKF) are prone to divergence in this application. In this dissertation a Sigma Point Kalman Filter (SP-KF) is implemented, resulting in an estimator which is able to cope with the significant nonlinearities in the system equations and uncertainty in state estimates while remaining tractable for real-time operation. In addition, the issues of data association and landmark initialization are addressed. Estimator performance is examined through Monte Carlo simulations in both two and three dimensions for scenarios involving UAV flight in cluttered environments. Hardware tests and simulations demonstrate navigation through an obstacle-strewn environment by a small Unmanned Ground Vehicle.

To Maggie.

Acknowledgments

> No man is an island, entire of itself; every
> man is a piece of the continent, a part of the
> main. *John Donne, Meditation XVII*

Very few people perform their work in isolation. Over the five and a half years I spent at Stanford I have relied on the help of many people, without whom this project would never have been finished.

First I thank my advisor, Professor Stephen Rock. By allowing us to find our own research projects he sends us off on a long, tangled journey. At first glance it seems we wander randomly, but in reality he guides us with careful hints and suggestions. This Socratic approach is both frustrating and incredibly rewarding, and in the end it makes better researchers of all of us. Most importantly I am grateful for the family-friendly environment he fosters, encouraging all of us with children to take the time to watch them grow.

I am very grateful to my reading committee, Professor Claire Tomlin and Professor Sanjay Lall. Thanks also to Professor Gunter Niemeyer for acting as defense committee chair. I greatly appreciate all of their comments and suggestions.

The final member of my defense committee was Professor Robert Cannon, who founded the ARL in 1984 with the idea of “putting smart people in a room, then standing back to watch what happens”. It is an extraordinary place and I am grateful to have been a part of it.

Without the help of the ARL’s staff I would never have finished. Godwin Zhang’s expertise with all things electronic is truly amazing. Sherann Ellsworth and Dana Parga made sure the lab was running smoothly: without them all research in the Guidance and Controls groups would grind to a halt. I also thank the Department’s graduate student services staff, Lynn Kaiser and Robin Murphy, for making sure all my paperwork was completed on time.

One of the greatest aspects of the ARL is the spirit of cooperation that exists among its students. It was obvious as soon as I began the process of joining the lab. The senior grad students were always available to talk about their research: the problems they were having, what they saw as good next steps and how it complemented the work of other students in the lab. I am especially grateful to Eric Frew, Andreas Huster, Hank Jones, and Jason Rife, four of the previous generation, for helping me get started in the lab. Later, when I was in the midst of my research, Chris Clark and

Tim Bretl could always ask the question that made me examine my work more carefully. Of my generation, Aaron Plotnik and Kristof Richmond have helped enormously both with practical items (without their image processing code I would have been here for months longer) and with many many discussions of research direction.

While the working environment in the lab was wonderful, the best part of my day was coming home to my family. My two daughters Hannah (now aged 3 3/4) and Ava (age 1) made the worst days into good days. I once asked Hannah, “Where would I be without you?” She thought about it for a second or two and then answered, “Lost.” I laughed and I cried– she spoke the truth.

Finally the greatest thanks go to my wife Maggie. She left her family and friends to drive 2600 miles with me as we started our adventure in far-off California. She will soon leave her friends in California as we travel to a new adventure in Pennsylvania. She is my wife, my partner, my best friend. I am ever-blessed with her and with the family that we have together.

Contents

Abstract iv

Acknowledgments vii

1 Introduction 1

1.1 Motivation 2

1.2 A Framework for Integrated Control and Navigation 4

1.3 The Estimation Problem 6

1.3.1 Preventing Estimator Divergence 7

1.3.2 Data Association 8

1.3.3 Landmark Initialization 8

1.3.4 Additional Issues 9

1.4 Related Work 10

1.4.1 Vision Based Navigation and Structure from Motion 10

1.4.2 Simultaneous Localization and Mapping 12

1.4.3 Data Association 12

1.4.4 Landmark Initialization 13

1.4.5 Sigma Point Kalman Filters 13

1.5 Summary of Contributions 14

1.6 Reader's Guide 15

2 The State Estimation Problem 16

2.1 Problem Statement 17

2.2 Sensor and System Models 19

2.2.1 Coordinate Frames 19

2.2.2 Vehicle Kinematic Model 19

2.2.3 Inertial Measurement Model 21

2.2.4 Vision Model 22

2.3 Nonlinear Estimation 23

2.3.1 Particle Filters . . . 24
2.3.2 Extended Kalman Filter . . . 25
2.3.3 Sigma Point Filters . . . 26
2.3.4 Comparison of Techniques . . . 27
2.4 Summary: The Estimation Problem . . . 30

3 Estimator Design 32
3.1 Inertial/Vision Navigation Filter . . . 33
3.1.1 Prediction Step . . . 33
3.1.2 Vision Update . . . 35
3.1.3 Choice of States . . . 35
3.2 Data Association . . . 36
3.3 Landmark Initialization . . . 38
3.4 Estimate Smoothing . . . 40
3.5 Data Flow . . . 41

4 UAV Simulation Results 44
4.1 Navigation in a Plane . . . 45
4.1.1 Estimate Consistency . . . 46
4.1.2 System Equations for the Planar Case . . . 46
4.1.3 Monte Carlo Simulation Results . . . 47
4.1.4 Navigation and Obstacle Avoidance . . . 51
4.2 3D Simulations . . . 51
4.2.1 Estimator Performance . . . 54
4.2.2 Effect of Explicit Data Association and Landmark Initialization . . . 56
4.2.3 Discussion of 3D Simulation Results . . . 59
4.3 Summary . . . 62

5 Ground Vehicle Results 64
5.1 Hardware Implementation . . . 65
5.1.1 Vision Subsystem . . . 65
5.1.2 Inertial Subsystem . . . 67
5.1.3 Path Planning and Control . . . 67
5.2 Test Description . . . 68
5.3 Vehicle State Estimation . . . 69
5.4 Obstacle relative position estimation . . . 73
5.5 Mapping . . . 74
5.5.1 Map Correction . . . 82

5.6 Summary 82

6 Conclusion 84

6.1 Summary of Contributions 87

6.1.1 Framework for Inertial/Visual Control and Navigation 87

6.1.2 Estimator Design 87

6.1.3 Performance Verification: Simulation 87

6.1.4 Performance Verification: Hardware 87

6.2 Recommendations for Future Work 88

6.2.1 Observability Analysis 88

6.2.2 Trajectory Generation 88

6.2.3 Alternate State Representations 88

6.2.4 Additional Sensors/Data 89

6.2.5 Other Vehicles and Other Environments 90

6.2.6 Multiple Vehicles 91

6.3 Some Very Informal Final Thoughts 91

A Information Required for Flight Control 94

B Estimator Summary 97

B.1 Estimator Equations 97

B.1.1 Kinematics 98

B.1.2 Vision Measurements 99

B.2 Simulation Parameters 100

Bibliography 102

List of Tables

2.1 Required information. 18

4.1 IMU initialization parameters for 2D simulations. 48
4.2 Maximum and minimum standard deviation ratios 50
4.3 Error growth parameters 61

5.1 Typical 1σ measurement noise for IMU portion of Phoenix-AX autopilot module. . 67
5.2 Results of vehicle state estimation 73

A.1 Longitudinal modes for Dragonfly UAV. 96
A.2 Lateral modes for Dragonfly UAV 96

List of Figures

1.1 Forest for autonomous navigation 2

1.2 Schematic of mission scenario. 3

1.3 Framework for a vision/inertial measurement navigation system 5

1.4 Schematic of data association problem. 8

1.5 Schematic of landmark initialization. 9

2.1 Schematic of estimation problem. 17

2.2 Coordinate frames. 19

2.3 Projection models. 23

2.4 Particle representing a Gaussian PDF propagated through sine function. 25

2.5 Linearized propagation of random variable through sine function 26

2.6 Unscented transform 27

2.7 Algorithm for Unscented Kalman Filter. 28

2.8 Single time update for non-holonomic vehicle. 29

3.1 Frame to frame data association. 37

3.2 Landmark initialization. 38

3.3 Flow of estimation. 41

4.1 Nominal data for 2D Monte Carlo simulations. 47

4.2 Estimator consistency for 2D navigation. 49

4.3 Change in estimate error over course of run. 50

4.4 Obstacle avoidance and navigation in 2D environment. 52

4.5 Exploration versus station keeping 53

4.6 Exploration vehicle position estimate error, known data association and landmark initialization. 55

4.7 Station keeping vehicle position estimate error, known data association and landmark initialization. 57

4.8 Exploration vehicle position estimate error, explicit data association and landmark initialization. 58

4.9 Station keeping vehicle position estimate error, explicit data association and landmark initialization. 60
4.10 Effect of landmark density on vehicle position estimate error. 61

5.1 The autonomous ground vehicle *Squirrel* used as testbed. 66
5.2 Schematic of mapping/navigation system. 66
5.3 The artificial “forest” used for hardware tests. 69
5.4 Estimated vehicle states, run 1. 70
5.5 Estimated vehicle states, run 2. 71
5.6 Estimated vehicle states, run 3. 72
5.7 Sequence of relative position estimates, run 1 75
5.8 Sequence of relative position estimates, run 2 76
5.9 Sequence of relative position estimates, run 3 77
5.10 Absolute position estimates, run 1 78
5.11 Absolute position estimates, run 2 79
5.12 Absolute position estimates, run 3 80
5.13 Simulation of error due to unmodeled camera pitch offset. 81
5.14 Simulation of error due to poor initial estimate of accelerometer bias. 81
5.15 Map corrected using updated vehicle position. 82

A.1 The Stanford DragonFly UAV. 95

Chapter 1

Introduction

THIS DISSERTATION DESCRIBES the development of a self-contained control and navigation system which uses only a low cost inertial measurement unit aided by monocular vision. This research was motivated by the problem of autonomous flight through an unknown, cluttered environment (such as a forest) by a small unmanned aerial vehicle (UAV). The payload limitations of a small UAV greatly restrict both the weight and physical dimensions of sensors that can be carried, complicating the problems of maintaining controlled flight (which generally requires knowledge of aircraft state) and of avoiding collisions with obstacles (which requires knowledge of obstacle relative position). Furthermore, direct measurements of vehicle position will only be sporadically available, since obstructions such as buildings, canyon walls or trees obstruct signals from navigation beacons such as GPS.

Operations in cluttered environments require advances in sensing, perception, estimation, control and planning. Of these, this dissertation focuses on the problem of estimation: computing the state of the vehicle (its position, orientation and velocity) and the positions of obstacles in the surrounding environment. Combined with a flight control system and a trajectory planner, the data from the estimator can enable safe flight in complex environments.

This estimation problem is difficult. First, the limited sensor suite greatly reduces the information that can be directly obtained about the system as a whole (i.e. the vehicle and its surroundings). Second, the equations which govern the system and measurements are highly nonlinear. The combination of the limited observability with the significant nonlinearities inherent to the system and the potential for significant uncertainties lead to an estimation problem that cannot reliably be solved using standard techniques.

This dissertation: (a) describes a framework for control and navigation using only an IMU and monocular vision; (b) presents a solution to the state estimation problem based on an Unscented Kalman Filter; (c) presents simulation results demonstrating the accuracy and consistency of the

Figure 1.1: Forest for autonomous navigation

Although this is a rather benign forest with well-defined trunks, no underbrush and no low branches it is still extremely challenging to navigate a path safely through.

estimator; and (d) presents results of hardware tests demonstrating real-time control and navigation through an artificial forest using a small autonomous ground vehicle as the test bed.

1.1 Motivation

Small autonomous Unmanned Aerial Vehicles (UAVs) are a particularly challenging subset of mobile robots and autonomous vehicles. They undergo six degree of freedom motion, are subject to significant external disturbances, require high bandwidth control, and have limited on-board sensing due to their small payload capacity. At the same time the missions envisioned for such vehicles are very challenging, involving low-altitude flight in obstacle-strewn terrain such as natural and urban canyons or forests (such as the one shown in Figure 1.1). The cluttered environment further complicates the problem of control and navigation by greatly reducing the reliability of GPS signals. A system which enables obstacle avoidance and navigation using only on-board sensing is therefore required.

This dissertation describes the development of a self-contained system to enable both control and navigation of small autonomous vehicles using only a low-cost MEMS IMU and monocular vision.

Micro electromechanical inertial measurement units (IMUs) have been commercially available for some time and have been used for sensing and stabilization in many applications. Their small size and low power requirements make them well suited to small UAV applications. However, two factors preclude purely inertial navigation solutions: first, IMUs do not provide information about

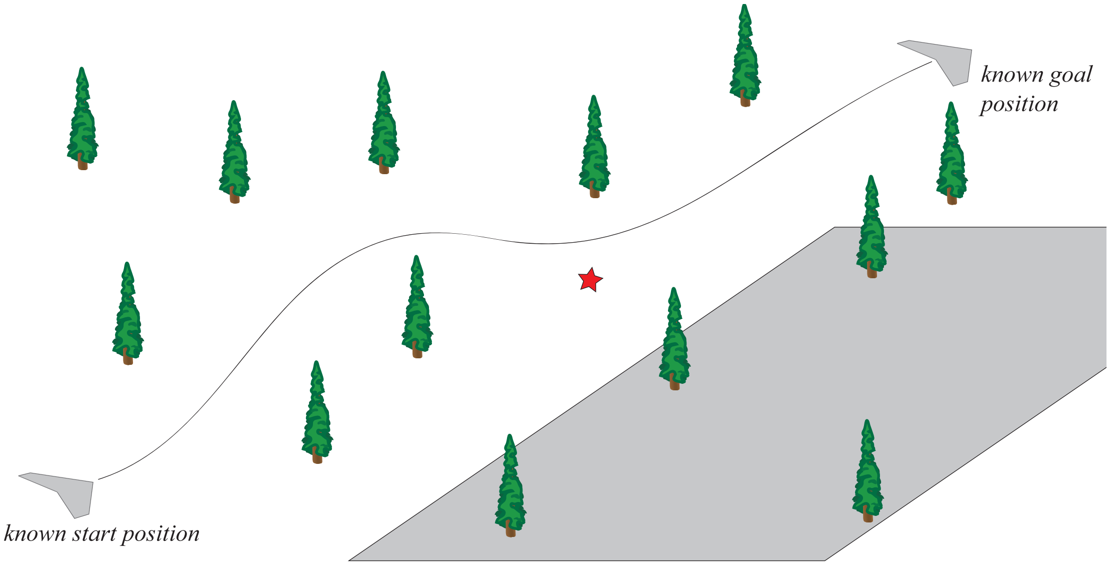

Figure 1.2: Schematic of mission scenario.

The aircraft must maintain controlled flight while avoiding collisions with trees and navigating from a known start position to a known goal. Additionally no-fly zones (shown in gray) must be avoided and any objects of interest (shown as a red star) must be mapped.

nearby obstacles; second, their noise and bias characteristics lead to rapid unbounded drift in the computed position. Additional sensors are therefore required.

Vision is a particularly rich stream of data suitable both for sensing and providing data to a human operator. CCD cameras have become very small and lightweight, and are thus suitable for use as a sensor on small vehicles. Vision systems can provide measurements to obstacles or landmarks in the environment to enable obstacle avoidance and to aid in computing vehicle position, orientation and velocity for navigation. A monocular vision system provides bearings to landmarks. By itself, a single bearing to a landmark does not provide enough information to localize it.[1] However, multiple bearings taken from disparate vantage points allow triangulation to determine the landmark's position.

While the technology is general to control and navigation of any type of vehicle operating without the assistance of absolute position measurements such as GPS (examples include autonomous

[1] A stereo pair provides depth information. However, the accuracy of the depth information is proportional to the separation of the cameras (baseline) and inversely proportional to the *square* of the actual distance to the feature. The size of the vehicle limits the baseline, hence range information to distant features will be highly uncertain. For example, a stereo pair with 30cm baseline, 640 pixel horizontal resolution, 70° field of view, 600mm focal length cameras has 1σ depth uncertainty of 1m at 10m, 1σ depth uncertainty of 4m at 20m.

underwater vehicles, unmanned ground vehicles operating in caves, indoors or on Mars), the motivating mission is exploratory flight of a small UAV through a previously unsurveyed forest (see Figure 1.2 for a schematic).

1.2 A Framework for Integrated Control and Navigation

Autonomous flight through a forest is an extremely challenging problem. In general successful operation of a UAV (in any environment, cluttered or clear) involves three basic tasks:

1. The vehicle must maintain controlled flight while avoiding collisions with obstacles (the vehicle must *aviate*). This requires a means to determine the state of the vehicle and to detect and localize obstacles with enough accuracy that appropriate action can be taken.

2. It must find its way from the starting point to a goal location in a finite amount of time (the vehicle must *navigate*). This requires a means to localize the vehicle relative to the goal.

3. It must convey information about the environment to a human operator or other robots in the team (the vehicle must *communicate*). This requires a means of presenting data in a useful way to human operators or other robots in the team.

These tasks are complicated by the payload limitations imposed by small vehicles (both mass and dimensions of the total sensing payload are constrained) and by the environments where the vehicle operates. The unavailability of GPS in cluttered environments means that direct measurements of vehicle position are unavailable. Furthermore, the environment is unsurveyed, hence obstacle positions are initially unknown.

The task of *aviation* could be accomplished by flying reactively: the vehicle maintains heading until an obstacle is detected, the vehicle maneuvers to avoid the obstacle and then attempts to reacquire the desired heading. However, while this reactive flight is adequate for small numbers of well-spaced obstacles, intuition suggests that the limited field of view of most sensors will cause this approach to fail in more complex environments with densely packed obstacles. Some means of accounting for obstacles which are outside of the field of view must be provided to plan safe maneuvers.

While it is certainly aviating, purely reactive flight can hardly be said to be *navigation*: without knowledge of aircraft position there is no guarantee of reaching the goal. Thus in order to navigate in an obstacle-strewn environment some means of obtaining the position of the vehicle must be provided.

The ultimate purpose of exploratory flight is to *communicate* knowledge of the environment (i.e. a map) to a human operator or to other robots in the team. If the map is generated in real time as the vehicle flies through the environment it can also be used to aid aviation (because obstacle locations are computed) and navigation (because vehicle position in the map is computed).

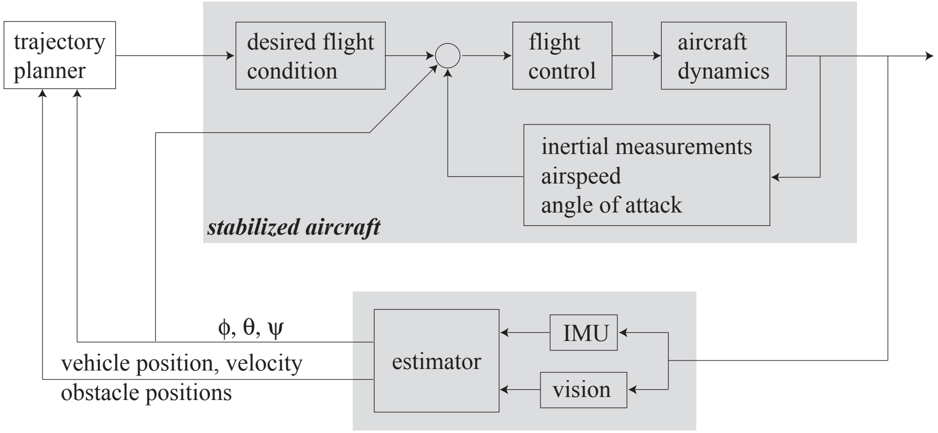

Figure 1.3: Framework for a vision/inertial measurement navigation system

A stabilized aircraft *is an aircraft that can maintain a desired flight condition. This may require measurements such as angular rates, angle of attack, sideslip angle and airspeed. In addition bank and pitch angles are required to stabilize certain longer-period dynamic modes, and more complex functions such as altitude hold require a measurement of altitude.*

A framework which enables aviation, navigation and communication is introduced in Figure 1.3. It comprises three parts: a trajectory planner; a stabilized aircraft; and an estimator. The trajectory planner uses knowledge of vehicle position and orientation and of the positions of nearby obstacles to compute a safe trajectory to the goal. A stabilized aircraft is one that can maintain a desired flight condition (determined based on the trajectory). This is enabled through measurements of variables such as angular rate and acceleration. Note that knowledge of other variables (such as angle of bank to control spiral divergence) may be necessary to maintain controlled flight. Finally the estimator uses available sensing (in this research, an IMU and a monocular camera) to compute the data required for flight control and trajectory planning[2].

The framework presented in Figure 1.3 can be generalized to other vehicles (such as autonomous underwater vehicles, or AUVs, and unmanned ground vehicles, or UGVs).

Significant advances in sensing, perception, estimation, planning and control must be realized before flight in cluttered environments can be successfully performed. Loosely defined, sensing and perception includes obtaining data about the vehicle and its environment and extracting useful information from the data. In the context of computer vision, perception is the problem of extracting relevant features in a stream of images. This is an extremely complex problem, especially in natural environments. Estimation is the process of extracting information about variables of interest from measurements that are noisy and may be related to these variables through complex mathematical

[2] In crewed aircraft the pilot provides the additional information required to maintain controlled flight and acts as trajectory planner. Position knowledge may be provided to the pilot by maps or navigation beacons such as GPS.

models. In this application (flight through a forest), the variables of interest include: vehicle orientation and velocity (to maintain controlled flight); obstacle relative position (to avoid collisions); and vehicle position (to enable navigation to a goal). Planning involves finding a safe, dynamically feasible path through the forest to a goal location, and finally control involves both stabilizing the vehicle and following the path computed by the planning algorithm.

The problem of state estimation is directly tied to enabling a small UAV to aviate and navigate through the environment and to communicate its acquired knowledge. Hence, the primary contribution of this dissertation is an estimator which computes the variables necessary for control, obstacle avoidance, navigation and mapping. Nonlinearities in the system models (both vehicle kinematics and the vision model) coupled with potentially large uncertainties in system states make this a particularly difficult estimation problem. This is further exacerbated by the lack of observability in the system: a monocular vision system provides only bearings to obstacles, making multiple measurements from different vantage points necessary to localize it.

1.3 The Estimation Problem

The critical technology described is the design of a recursive estimator which fuses inertial and vision measurements to determine aircraft states and landmark positions. The estimation problem is highly nonlinear due to the kinematics of the vehicle and the measurement model. The nonlinearities combined with the lack of observability inherent to the problem (due to bearings-only measurements to landmarks) and the noise and bias errors inherent to low-cost IMUs results in an estimation problem which can not reliably be solved using standard techniques.

Estimating vehicle state as well as the positions of obstacles or landmarks in the environment is a Simultaneous Localization and Mapping (SLAM) problem, a field of research which has received significant attention by the mobile robotics community in recent years. In a typical SLAM implementation the vehicle obtains measurements of ego motion (sometimes called *proprioceptive* measurements) and relative measurements (generally range and bearing) to nearby landmarks (called *exteroceptive* measurements).

The first paper to define landmark positions as states to be estimated was written by Smith and Cheeseman [50]. Their implementation of an Extended Kalman Filter (EKF) to estimate vehicle and landmark states was based on a nonlinear vehicle motion model and the nonlinear range and bearing measurements to landmarks, and this has become a standard approach for SLAM. Kim [27, 25, 26] describes an EKF-based implementation on a medium-sized UAV (10kg payload capacity) using inertial measurements along with range and bearings to landmarks. The difficulties of implementing SLAM on UAVs include highly nonlinear system dynamics, the limits imposed on landmark observability by trajectory constraints and the high accelerations and roll rates undergone by the vehicle.

The research presented in this dissertation is concerned with SLAM on a small UAV operating in a cluttered environment. Since a monocular camera is the only exteroceptive sensor, range measurements are unavailable. This leads to a more difficult case of SLAM: the reduced observability complicates the estimation process. Furthermore, in cluttered, obstacle-strewn environments the vehicle operates in close proximity to the landmarks used as navigation references, increasing the sensitivity to uncertainties. In this case the uncertainty in the predicted vehicle state and predicted landmark positions combined with the nonlinearities inherent to the system often cause EKF-based approaches to diverge.

The bearings-only exteroceptive measurements also complicate the problems of data association (correctly associating a bearing with its corresponding landmark) and landmark initialization (computing an initial estimate of range given only bearing measurements).

This dissertation presents solutions to three challenges inherent to the estimation problem: preventing estimator divergence, data association, and landmark initialization.

1.3.1 Preventing Estimator Divergence

The first problem addressed is estimator divergence, a well known problem which can affect nonlinear estimators. An Extended Kalman Filter (EKF) approximates the system equations by a first order Taylor series expansion about the current best estimate. The estimate mean and covariance are then propagated through the linearized system equations. This has proven to be an extremely powerful technique but there are situations where assumptions inherent to the EKF are not applicable, causing divergence of the estimated states.

The linearization step of an EKF inherently assumes that uncertainty is small (i.e. it assumes that the system equations are well approximated by a first order Taylor series expansion over the span of the uncertainty). If this assumption is invalid there are two effects: first the estimate mean and covariance may be propagated incorrectly; and second is the (unmodeled) error introduced by linearizing about the best estimate of the state and not about true state.

When vehicles operate in cluttered environments they are in close proximity to the landmarks used as navigation references. Because of nonlinearities in the system equations, this close proximity increases the sensitivity of the estimation process to uncertainties. As a result, the estimation problem described in this dissertation cannot reliably be solved using an EKF because of this increased sensitivity to uncertainties.

This dissertation presents an implementation of SLAM using an Unscented Kalman Filter (UKF). The UKF implementation is shown to generate consistent estimates of vehicle state and obstacle positions, enabling navigation in a cluttered environment without aids such as GPS.

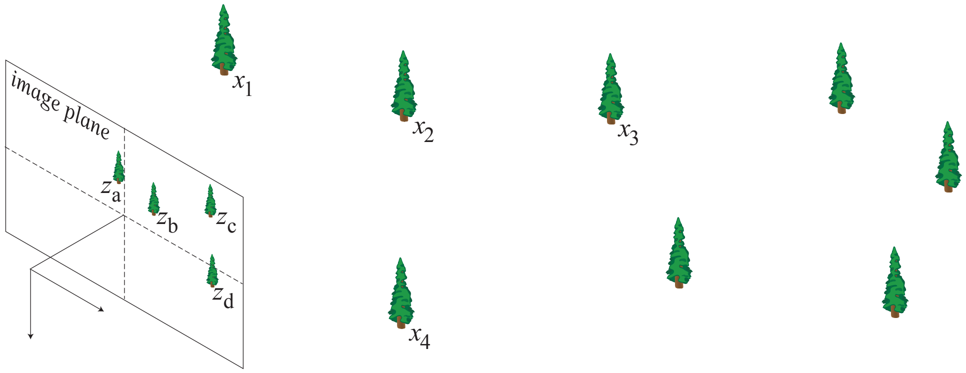

Figure 1.4: Schematic of data association problem.

Data association is the process of associating measurements $\{z_a\ z_b\ z_c\ z_d\}$ *with landmarks* $\{x_1\ x_2\ x_3\ x_4\}$.

1.3.2 Data Association

Inherent in any Kalman filter is an assumption of known data association. However, in many SLAM implementations landmarks are indistinguishable from one another, hence this must be computed explicitly (see Figure 1.4). It consists of associating measurements $\{z_a\ z_b\ z_c\ z_d\}$ with landmarks $\{x_1\ x_2\ x_3\ x_4\}$.

Data association must be robust to losses of individual features (which may be due to occlusions or may occur when a landmark is on the edge of the sensor's detection envelope) and losses of an entire measurement cycle. It is particularly difficult here because of the small size of the measurement subspace (the 2D image plane as opposed to the 3D physical space). It is especially difficult when landmarks have not yet been localized to a high degree of accuracy.

In Chapter 3 this dissertation proposes a two stage process for data association: first, the current bearings are compared with those obtained in a previous frame to check frame to frame correspondence; second, bearings to features not seen in the previous frame are compared with predicted bearings obtained from landmarks in the map to check if the features have been seen earlier in the run. Those bearings that are not associated in either step are assumed to come from a new, previously unseen landmark.

1.3.3 Landmark Initialization

The third problem is landmark initialization, a critical component of SLAM. It consists of computing an initial estimate of range given only the measurements to a landmark. In this research it is complicated by the lack of information provided by a single bearing (see Figure 1.5). When a landmark is initialized its position and covariance must be close enough to truth that the filter does not diverge.

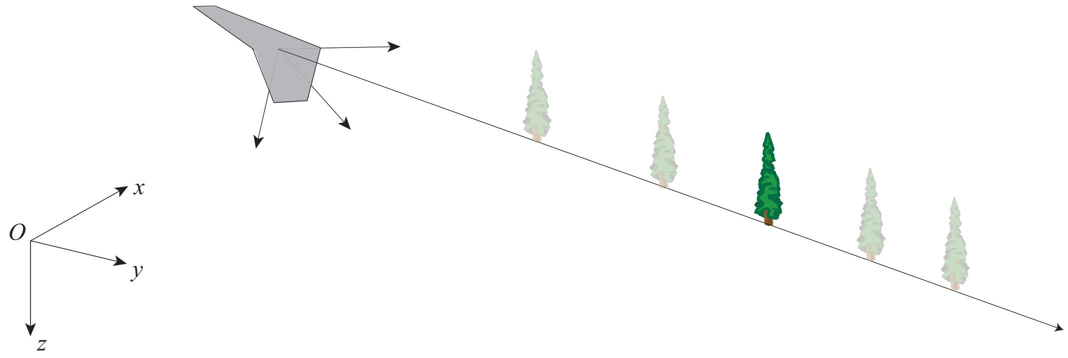

Figure 1.5: Schematic of landmark initialization.

Landmark initialization consists of computing an initial estimate of range given only bearings to a landmark.

In this dissertation landmarks are assumed to lie on a flat ground plane. Using the estimate of vehicle altitude a new landmark is initialized at the intersection of the bearing to the landmark and the ground plane. This can be generalized to non-planar ground with the addition of a digital elevation map (DEM): landmarks can be initialized at the intersection of the bearing to the feature and the ground as defined by the DEM.

1.3.4 Additional Issues

Two additional issues inherent to the estimation problem considered here are drift of the estimate and the effect of vehicle trajectory on the estimate.

Drift

Bearing measurements provide no information about vehicle absolute position or about landmark absolute position. Absolute position is therefore unobservable, and unless additional information in the form of absolute measurements are available the estimates of vehicle and landmark absolute position will drift. If there are no unmodeled dynamics or biases this drift can be modeled as a random walk.

In most SLAM implementations (including this one) the uncertainty in all the states becomes highly correlated over the course of vehicle motion. Hence additional information about any of the states can be used to improve the estimates of all the states. This information may come from many sources: loop closure, which consists of revisiting previously explored terrain; observation of a priori known landmarks; or sporadic GPS updates. With this additional information a smoothing algorithm can correct the drift in absolute vehicle and landmark positions. Using loop closure to limit error growth is a standard technique in SLAM.

Trajectory Considerations

Since only bearings to obstacles are available, the motion of the camera (i.e. the trajectory flown by the UAV) greatly affects the utility of the information gained by subsequent bearing measurements. During motion directly towards or away from an object (along the bearing) there is no new information which improves range estimate. Transverse motion is required to produce a useful estimate of object position. In the case of obstacle avoidance, transverse motion has the added benefit of ensuring that a collision is avoided, but the presence of multiple obstacles places conflicting demands on the trajectory which must be flown.

The choice of trajectory can therefore have a significant effect on the uncertainty associated with the state estimate. This suggests that trajectories which optimize parameters such as uncertainty in vehicle position estimate can be designed in addition to the "standard" considerations of obstacle avoidance or minimum time to reach the goal.

1.4 Related Work

There has been a tremendous amount of research relating to the problem of navigation and state estimation for mobile robots (flight, ground and undersea). The previous section presented some references specifically related to a UAV based SLAM implementation, this section presents a more detailed discussion of research in the related fields of vision based navigation, SLAM, and Sigma Point Kalman Filters.

1.4.1 Vision Based Navigation and Structure from Motion

Vision has been extensively studied for use as a sensor in estimation related applications. However past work has not dealt with estimating all the states necessary for flight in cluttered environments (i.e. vehicle state and obstacle states). Examples include structure from motion, vision augmented inertial navigation, real time benthic navigation and relative position estimation.

Structure from motion attempts to reconstruct the trajectory of the video camera and an unknown scene. An example of an application is given in [42], which describes reconstruction of archaeological sites using video from a hand-carried camera. However, structure from motion algorithms are typically formulated as batch processes, analyzing and processing all images in the sequence simultaneously. While this will give the greatest accuracy of both the reconstructed scene and camera path, it does not lend itself to real-time operation.

Research into vision augmented inertial navigation [47, 31, 37] is primarily concerned with estimating the vehicle state by fusing inertial measurements either with bearings to known fiducials or data from optical flow algorithms. A variant is presented by Diel [11], who uses epipolar constraints for vision-aided inertial navigation. Positions of unknown obstacles are not estimated.

Real time benthic navigation using vision as the primary sensor is described in Marks [32]. Distance from a planar surface (i.e. the ocean floor or a canyon wall) is obtained using a sonar proximity sensor and texture correlation is used to determine position offsets relative to a reference image. This capability has been adapted to enable underwater station keeping [29] and has been extended to incorporate additional sensors [45]. However this technique only estimates vehicle position, not the position of obstacles in the environment.

Huster [18] demonstrated fusion of inertial and monocular vision measurements for an underwater object retrieval task. In this case only one object in the environment was considered and relative position estimation (between the vehicle and object) was performed, not absolute vehicle and obstacle position estimation.

The use of vision for aiding UAV navigation has become an active area of research. In many cases vision is not the primary navigation/control sensor but is used in conjunction with inertial navigation systems and GPS to increase situation awareness. For example, Amidi [1] describes vision aided navigation for an autonomous helicopter where a stereo pair is used to aid in station keeping. Sinopoli [49] describe a system that uses data from fused GPS/INS and a digital elevation map to plan coarse trajectories which are then refined using data from a vision system. Roberts [46] describes a flight control system for a helicopter that uses a stereo pair to determine altitude and optical flow to determine ground speed. Vision aided landing on a pad of known size and shape is described in [48]. A more complex system for identifying suitable terrain for landing an autonomous helicopter is described in [33], which uses fused GPS/INS for control and navigation and a stereo pair for determining local terrain characteristics.

Vision-based state estimation for UAVs based on techniques derived from structure from motion are described in [56, 43]. Structure from motion is able to recover scene information and camera motion up to a scale factor, and an accurate dynamic model of the vehicle is required to help solve for the scale factor. These techniques are specific to the vehicle carrying the camera, and it is unclear how external disturbances will affect the result.

Proctor [44] describes a vision-only landing system that performs relative state estimation with respect to a set of known fiducials. A constant velocity motion model is used to model camera motion. Wu [58] describes a vision-aided inertial navigation system that relies on measurements to a known target for vehicle state estimation. Both are examples of terrain aided navigation (TAN), where measurements to known landmarks are used to aid navigation. Initially unknown environments are not addressed.

None of the vision aided navigation research described above addresses the problem of simultaneously estimating vehicle state and obstacle positions using only monocular vision and inertial measurements.

1.4.2 Simultaneous Localization and Mapping

Simultaneous Localization and Mapping (SLAM, sometimes called Concurrent Mapping and Localization) is the process of simultaneously estimating the state of an autonomous vehicle and landmarks in the environment. It permits vehicle navigation in an initially unknown environment using only on-board sensing, and therefore can be used in situations where signals from navigation beacons such as GPS is unavailable. This dissertation addresses the case of bearings as the only exteroceptive measurement and a low-cost IMU providing proprioceptive measurements for a 6DOF vehicle operating in close proximity to obstacles.

EKF implementations of SLAM using range and bearing measurements have been applied both in simulation and on hardware in many scenarios including indoor navigation of small robots [52], subsea navigation by Autonomous Underwater Vehicles (AUVs) [57] , outdoor navigation by wheeled robots [30] and navigation by aircraft [25, 26, 27]. In these cases range measurements to landmarks are available.

Bearings-only SLAM using cameras mounted on wheeled ground vehicles is described in [28, 15, 35]. In these cases only pure 2D motion is considered and estimation is performed for the planar environment.

Davison [10] describes a bearings-only SLAM implementation using only a monocular camera. Again an EKF is used to recursively estimate the state of the camera and of landmarks, and a constant velocity model with unknown acceleration is used to describe camera motion. By itself this system will be able to estimate motion and landmark positions up to a scale factor. To determine the scale factor the system is initialized by viewing a set of known landmarks. In unexplored environments, however, there are no known landmarks that can be used to determine the scale and some other means must be employed.

Burschka [8] describes a fused vision/inertial navigation system for off-road capable vehicles. Here the main focus is on vehicle pose estimation: a map of the environment is not maintained. Foxlin [16] describes a wearable vision/inertial system for self-tracking that uses unique coded fiducials for indoor tracking of humans. A range estimate is computed based on the size of the fiducial in the image plane.

The research described above does not address the combination of only bearings combined with inertial measurements, 6DOF estimation for a vehicle flying among obstacles.

1.4.3 Data Association

Typical data association algorithms are based on using a χ^2 test to compare an actual measurement with a prediction. After computing likelihoods of possible associations either a gated nearest neighbor approach is used to determine association on a landmark-by-landmark basis or a joint compatibility test [36] is used to determine the most likely overall set of associations.

Previous work has proposed using additional information (e.g. in an indoor SLAM implementation described by Neira [35] the lengths of the vertical lines used as features is used as additional information for data association; Fitzgibbons [15] uses color) to assist in the process of data association. In this research additional identifying information is not available: the vision system provides only a bearing to a landmark.

1.4.4 Landmark Initialization

Methods for feature initialization can be characterized as undelayed or delayed. Undelayed approaches [10, 19, 28] represent the conical probability distribution function of a single bearing as a series of Gaussians which are then pruned as more measurements become available. Delayed methods collect several bearings to a feature from different vehicle poses and compute a landmark position. It is difficult, however, to obtain an initial landmark position and covariance which is sufficiently Gaussian to prevent divergence of Kalman-type filters. Bailey [2] describes a method for constrained initialization which computes the “Gaussian-ness” by calculating the Kullback-Leibler distance. However this is expensive to compute and a threshold value had to be determined experimentally. Another approach is described in Fitzgibbons [15] and in Montesanto [34], where particle filters are used for landmark placement until the distribution is sufficiently Gaussian to permit a switch to an EKF framework.

1.4.5 Sigma Point Kalman Filters

Rather than approximating the system equations, particle filters instead approximate the *distribution* of the estimated states with a randomly generated set of points that are propagated through the full nonlinear system equations [53]. No assumptions regarding the distribution are made and no assumptions about the characteristics of the noise are made. Therefore they lend themselves very well to situations where the EKF is not applicable (e.g. due to noise characteristics or the degree of nonlinearity of the system). However, the number of particles required to adequately model a distribution is strongly dependent on both the dimension of the state vector and on the uncertainty of the distribution which is being approximated [53]. Thus in problems with large numbers of states particle filters quickly become intractable for real-time operation.

Sigma Point Kalman Filters (SP-KF, sometimes called Unscented Kalman Filter, or UKF) can be viewed as a special case of particle filter that occur when the estimated states and system and measurement noise obey a Gaussian probability distribution [21, 23, 54]. Rather than a large number of randomly generated points, a small set of deterministically chosen *Sigma Points* are used to approximate the distribution. The Sigma Points are propagated through the system equations and then the estimate mean and covariance are recovered. A Sigma Point Kalman Filter is a relatively new estimation and sensor fusion technique, albeit one that is rapidly gaining acceptance in the research community.

Variants have been proposed such as the Square Root Unscented Kalman Filter [54], which propagates the square root of the covariance rather than the covariance itself and a reduced-order UKF [22], which propagates fewer Sigma Points.

Sigma Point Kalman Filters are being applied to a wide variety of estimation problems. An SP-KF implementation for integrated GPS/INS navigation is described in [55]. Huster [18] describes an SP-KF implementation for relative position estimation using a monocular camera and IMU.

1.5 Summary of Contributions

The main contributions of this dissertation are summarized below:

- **Framework for Integrated Control and Navigation using only Vision and Inertial sensors**
  A framework which enables control and navigation of a small autonomous vehicle has been developed and implemented. This new system fuses data from a low-cost, low power MEMS inertial measurement unit and a light-weight CCD camera to reduce drift associated with pure inertial navigation solutions and to address the technical issues associated with monocular vision only navigation solutions.

- **Estimator Design**
  An estimator based on the Sigma Point Kalman Filter was developed in the context of this framework. Vehicle state (position, orientation, velocity), IMU biases and obstacle positions are estimated. This information was used by a trajectory planner to compute safe paths through a cluttered environment.

- **Performance Verification: Simulation**
  Results of Monte Carlo simulations of UAV flight in obstacle-strewn environments show that the UKF-based implementation provides a solution to the estimation problem. Mean error is small and the error covariance is accurately predicted. Monte Carlo simulations investigating error growth characteristics were conducted for two classes of flight: exploration (where new terrain is being explored) and station keeping (where a set of landmarks may be in continuous view). For exploration flight the estimated vehicle position estimate error is an approximately constant percentage of distance traveled, for station keeping flight vehicle position estimate error varies cyclically with each orbit. For both classes the magnitude of the error varies inversely with square root of the number of landmarks in view.

- **Performance Verification: Hardware**
  Navigation in a cluttered environment by a small Unmanned Ground Vehicle using only a

low cost IMU and vision sensor was demonstrated. This showed successful state estimation on an operational system, with real sensor measurements and model and calibration errors. In addition, the hardware tests demonstrated real-time integration of the estimation algorithm with an obstacle avoidance and navigation algorithm.

1.6 Reader's Guide

The remainder of this dissertation is organized as follows:

Chapter 2: The State Estimation Problem begins with a brief discussion of the information required for flight control, obstacle avoidance and navigation. It then defines the state variables and develops models for vehicle kinematics, inertial measurements, and vision measurements. It also includes a discussion of techniques for nonlinear estimation which motivates the application of a Sigma Point Kalman Filter.

Chapter 3: Estimator Design describes the estimation problem, outlining the difficulties associated with the nonlinearities and uncertainty in this application. It then describes the solution to the estimation problem.

Chapter 4: UAV Simulation Results presents results of Monte Carlo simulations of UAV flight in unsurveyed environments. Accuracy of state estimates are addressed through 2D simulations. Vehicle position estimate error growth characteristics and dependence on the number of landmarks in view are addressed through 3D simulations.

Chapter 5: Ground Vehicle Results describes a hardware implementation using a small autonomous ground vehicle as test bed. Results of tests demonstrating navigation in an cluttered environment are presented.

Chapter 6: Conclusion summarizes results of this research and discusses areas for future work.

Chapter 2

The State Estimation Problem

THIS SECTION DEFINES the estimation problem introduced in the previous chapter. It has three purposes: (a) define the state estimation problem; (b) develop equations for plant and sensor models; (c) provide some justification for applying a Sigma Point Kalman Filter to this estimation problem. The estimator is then designed and implemented in Chapter 3, and Chapter 4 shows that the SP-KF-based implementation does indeed result in a convergent, consistent estimator.

The choice of variables used to describe the state of the vehicle and its environment is an important factor in the design of a solution and its eventual complexity. The state variables must be sufficient to enable control of the vehicle, avoid obstacles and allow navigation to a goal. At the same time the choice of state variables has a strong effect on the complexity of the models used to describe the system. For example, a particular choice of state variables may lead to a very simple model for the vision system but complex models for vehicle and landmark dynamics. This trade off must be made in consideration of the limitations imposed by real-time operation of the resulting estimator.

The equations describing vehicle kinematics, inertial measurements and vision measurements are highly nonlinear. To provide some intuition into the difficulties associated with nonlinear estimation this chapter includes a brief discussion of methods and provides an example comparing the behavior of three types of nonlinear estimator: the Particle Filter, the Extended Kalman Filter (EKF), and the Sigma Point Kalman Filter (SP-KF). This motivates the application of a Sigma Point Kalman Filter to solve the estimation problem.

Section 2.1 defines the estimation problem and state variables. Section 2.2 derives models for vehicle kinematics, inertial sensors and vision sensors. Section 2.3 discusses three techniques for nonlinear estimation (Particle Filter, EKF and SP-KF). Finally Section 2.4 provides a summary.

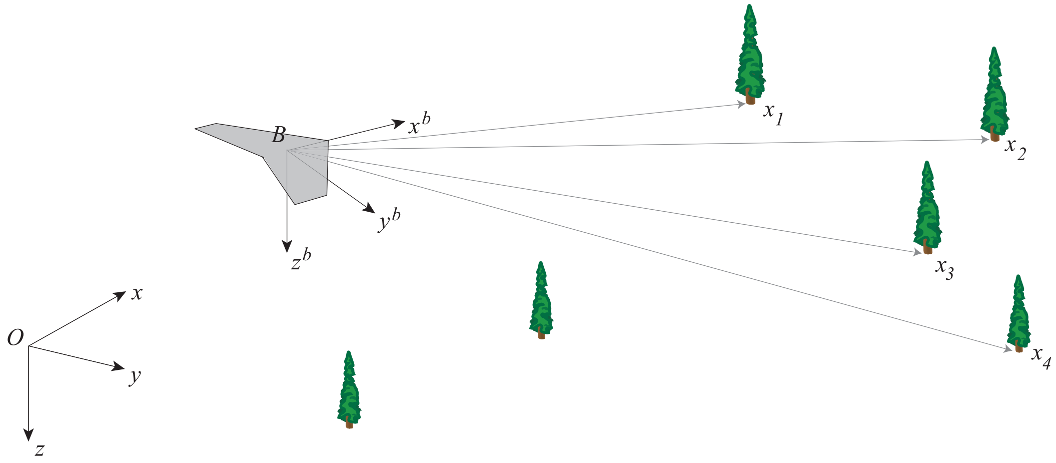

Figure 2.1: Schematic of estimation problem.

The aircraft obtains bearings to fixed landmarks (tree trunks) and measurements of acceleration and angular rate. Using these measurements an estimate of aircraft position, orientation, and velocity as well as obstacle positions must be obtained.

2.1 Problem Statement

As discussed in Chapter 1 the scenario considered here consists of a small UAV flying through an unsurveyed forest (Figure 2.1) using only an inertial measurement unit and a monocular camera. The on-board camera obtains bearing measurements to obstacles (tree trunks) and the inertial measurement unit provides accelerations and angular rates in the body-fixed frame.

For the purpose of this dissertation, flight control is taken to refer only to the maintenance of steady, controlled flight (the first part of the *aviate* task: the second part is obstacle avoidance). Navigation refers to directed motion towards a goal. In general the information required for flight control differs from that required for navigation, and often the computations and actions required for flight control occur at much higher rate than those for navigation. Flight control systems have been the subject of enormous amounts of research and have been covered in numerous textbooks (e.g. Blakelock [4], Bryson [7], or Etkin [13]). In general angular rate, orientation and speed are required for flight control (see Appendix A for an illustrative example), vehicle position is required for navigation and obstacle relative position is required for obstacle avoidance. This is summarized in Table 2.1.

In addition to vehicle position, orientation and speed, low cost IMUs are subject to scale factor and bias errors that can drift with time, thus estimates of scale factor and bias are also required. The vehicle state vector is

$$\mathbf{x}_v = \begin{bmatrix} x & y & z & \phi & \theta & \psi & u & v & w & \boldsymbol{\alpha}^T & \mathbf{b}_a^T & \mathbf{b}_\omega^T \end{bmatrix}^T \tag{2.1}$$

Table 2.1: Required information.

description	purpose	source
angular rate	flight control	measured by IMU
orientation	flight control and navigation	estimated
speed	flight control and navigation	estimated
vehicle position	navigation	estimated
obstacle relative position	collision avoidance	estimated

Referring to Figure 2.1, ($x\ y\ z$) represents position in the inertial frame, ($\phi\ \theta\ \psi$) represent Euler angles with respect to the inertial frame, ($u\ v\ w$) represents velocity expressed in the body frame, $\boldsymbol{\alpha}^T$ represents IMU scale factor error, $\mathbf{b}_a^T$ represents accelerometer bias, and finally $\mathbf{b}_\omega^T$ represents rate gyro bias.

In addition to vehicle state, obstacle relative positions are required. In this dissertation absolute obstacle positions in the inertial frame are estimated. This simplifies the mapping process and, as will be further discussed in Chapter 3, simplifies the computational requirements of the resulting estimator. Obstacle relative position can easily be computed from the absolute obstacle position and vehicle absolute position.

The final state vector is

$$\mathbf{x} = \begin{bmatrix} \mathbf{x}_v^T & \mathbf{x}_1^T & \mathbf{x}_2^T & \cdots & \mathbf{x}_m^T \end{bmatrix}^T \tag{2.2}$$

where $\mathbf{x}_v$ is the vehicle state defined in Equation 2.1 and $\mathbf{x}_i = [x_i\ y_i\ z_i]^T$, the position of the i^{th} obstacle in the inertial frame.

Given the noisy, limited measurements available from the IMU and vision system, the problem is to obtain the information required to control the aircraft, avoid collisions with obstacles and to permit navigation. That is, the problem is to compute an estimate $\hat{\mathbf{x}}$ and covariance $\mathbf{P}$ of the state vector $\mathbf{x}$ given a process model

$$\dot{\mathbf{x}} = f(\mathbf{x}, \mathbf{u}) \tag{2.3}$$

and a measurement model

$$\mathbf{z}_{imu} = g_1(\mathbf{x}, \mathbf{u}) \tag{2.4}$$

$$\mathbf{z}_{cam} = g_2(\mathbf{x}) \tag{2.5}$$

Here $\mathbf{u}$ represent inputs to the plant, $\mathbf{z}_{imu}$ represent inertial measurements, and $\mathbf{z}_{cam}$ represents bearing measurements. The process model f is developed in Section 2.2.2, the inertial measurement model g_1 is developed in Section 2.2.3 and the vision model g_2 is developed in Section 2.2.4. Chapter 3 integrates the models to form the prediction equations and the vision update equations. A

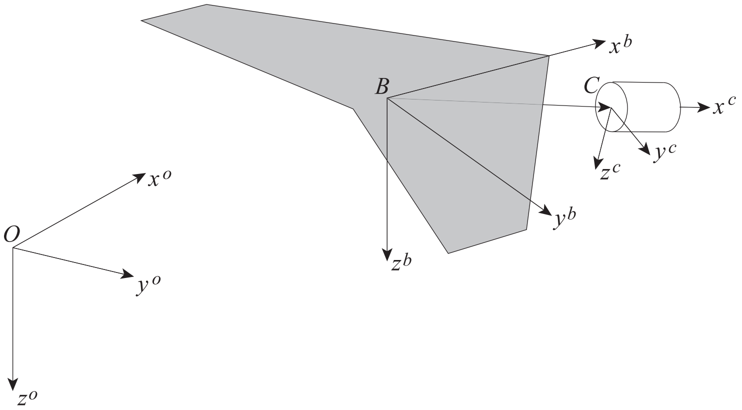

Figure 2.2: Coordinate frames.

Frame O is an inertial NED frame. B is the vehicle body-fixed frame, the matrix $\mathbf{T}$ defines the transformation of a vector in O to its representation in B. Frame C is the camera-fixed frame, with the camera's optical axis aligned with x^c. The transformation $\mathbf{T}_{cam}$ between the camera frame and the body frame B is assumed known and the axes of the inertial measurement unit are assumed to be aligned perfectly with the body frame B.

complete summary of the equations used in the estimator prediction and correction steps is given in Appendix B.

2.2 Sensor and System Models

2.2.1 Coordinate Frames

Navigation is done with respect to an inertial North-East-Down (NED) coordinate frame O. Sensors are fixed to the vehicle with known position and angular offsets with respect to a body-fixed frame B. Acceleration and angular rate are measured using a strapdown inertial measurement unit in the body frame B, bearings to landmarks are obtained in a camera frame C. Transformation matrices $\mathbf{T}$ and $\mathbf{T}_{cam}$ define the transformation of a vector expressed in O to B and a vector expressed in B to C, respectively. Coordinate frames are shown schematically in Figure 2.2.

2.2.2 Vehicle Kinematic Model

A dynamic model requires knowledge of all inputs, including disturbances. For small UAVs there is a very high degree of uncertainty associated with disturbances which act on the vehicle[1]. In this

[1] Disturbances would consist of gusts, which are extremely difficult to characterize in cluttered environments.

case a standard technique is to use a kinematic model driven by inertial measurements as a process model.

Vehicle position x, y, z is expressed in the inertial frame, rotations are expressed as Euler angles ϕ, θ, ψ relative to the inertial frame and velocity u, v, w are in expressed in the body frame. The coordinate transform $\mathbf{T}$ (defined in Equation 2.11) projects a vector expressed in the inertial frame O into the body frame B. Vehicle kinematics are:

$$\begin{bmatrix} \dot{x} \\ \dot{y} \\ \dot{z} \end{bmatrix} = \mathbf{T}^{-1} \begin{bmatrix} u \\ v \\ w \end{bmatrix} \tag{2.6}$$

The transformation matrix $\mathbf{T}$ is defined by the Euler angles of the aircraft with respect to the inertial frame. Following a roll-pitch-yaw convention,

$$\mathbf{T} = \mathbf{T}_\phi \mathbf{T}_\theta \mathbf{T}_\psi \tag{2.7}$$

where

$$\mathbf{T}_\phi = \begin{bmatrix} 1 & 0 & 0 \\ 0 & \cos\phi & \sin\phi \\ 0 & -\sin\phi & \cos\phi \end{bmatrix} \tag{2.8}$$

$$\mathbf{T}_\theta = \begin{bmatrix} \cos\theta & 0 & -\sin\theta \\ 0 & 1 & 0 \\ \sin\theta & 0 & \cos\theta \end{bmatrix} \tag{2.9}$$

$$\mathbf{T}_\psi = \begin{bmatrix} \cos\psi & \sin\psi & 0 \\ -\sin\psi & \cos\psi & 0 \\ 0 & 0 & 1 \end{bmatrix} \tag{2.10}$$

Therefore,

$$\mathbf{T} = \begin{bmatrix} \cos\theta\cos\psi & \cos\theta\sin\psi & -\sin\theta \\ \sin\phi\sin\theta\cos\psi - \cos\phi\sin\psi & \sin\phi\sin\theta\sin\psi + \cos\phi\cos\psi & \sin\phi\cos\theta \\ \cos\phi\sin\theta\cos\psi + \sin\phi\sin\psi & \cos\phi\sin\theta\sin\psi - \sin\phi\cos\psi & \cos\phi\cos\theta \end{bmatrix} \tag{2.11}$$

Body angular rates can be expressed as Euler angle rates by:

$$\begin{bmatrix} \dot{\phi} \\ \dot{\theta} \\ \dot{\psi} \end{bmatrix} = \begin{bmatrix} 1 & \sin\phi\tan\theta & \cos\phi\tan\theta \\ 0 & \cos\phi & -\sin\phi \\ 0 & \frac{\sin\phi}{\cos\theta} & \frac{\cos\phi}{\cos\theta} \end{bmatrix} \begin{bmatrix} p \\ q \\ r \end{bmatrix} \tag{2.12}$$

Expanding Equations 2.6 and 2.12 gives

$$\dot{x} = \cos\theta\cos\psi\,u + (\sin\phi\sin\theta\cos\psi - \cos\phi\sin\psi)\,v + (\cos\phi\sin\theta\cos\psi + \sin\phi\sin\psi)\,w \quad (2.13)$$

$$\dot{y} = \cos\theta\sin\psi\,u + (\sin\phi\sin\theta\sin\psi + \cos\phi\cos\psi)\,v + (\cos\phi\sin\theta\sin\psi - \sin\phi\cos\psi)\,w \quad (2.14)$$

$$\dot{z} = -\sin\theta\,u + \sin\phi\cos\theta\,v + \cos\phi\cos\theta\,w \quad (2.15)$$

$$\dot{\phi} = p + \sin\phi\tan\theta\,q - \cos\phi\tan\theta\,r \quad (2.16)$$

$$\dot{\theta} = \cos\phi\,q - \sin\phi\,r \quad (2.17)$$

$$\dot{\psi} = \frac{\sin\phi}{\cos\theta}q + \frac{\cos\phi}{\cos\theta}r \quad (2.18)$$

2.2.3 Inertial Measurement Model

The inertial measurement unit includes accelerometers and rate gyros. The accelerometers measure specific force, which includes the acceleration of the vehicle and the projection of the acceleration due to gravity onto the body frame. The rate gyros measure the rotational velocity of the vehicle. Both sensors include sensor biases and zero mean Gaussian random noise. Using the vehicle state vector defined in Equation 2.1, the IMU measurement model g_1 can be written as:

$$\mathbf{z}_a = \text{diag}(\boldsymbol{\alpha})\left[\frac{\text{d}}{\text{d}t}\mathbf{u}_a - \mathbf{T}\mathbf{g}\right] + \mathbf{b}_a + \mathbf{n}_a \quad (2.19)$$

$$\mathbf{z}_\omega = \boldsymbol{\omega} + \mathbf{b}_\omega + \mathbf{n}_\omega \quad (2.20)$$

where $\mathbf{z}_{imu} = \left[\mathbf{z}_a^T\ \mathbf{z}_\omega^T\right]^T$ is the IMU measurement vector and $\mathbf{u}_a$ represents the velocity of the accelerometer. The accelerometer scale factor correction is represented by $\text{diag}(\boldsymbol{\alpha}) \approx \mathbf{I}_{3\times3}$. The angular velocity $\boldsymbol{\omega}$ represents the components p, q, r of the vehicle angular velocity, expressed in the body frame.

The IMU is offset from the aircraft CG by a known amount $\boldsymbol{\rho}$, hence

$$\mathbf{u}_a = \mathbf{u}_v + \boldsymbol{\omega} \times \boldsymbol{\rho} \quad (2.21)$$

where $\mathbf{u}_v = [u\ v\ w]^T$ denotes the velocity of the aircraft CG expressed in the body frame B. Taking the time derivative,

$$\frac{\text{d}}{\text{d}t}\mathbf{u}_a = \dot{\mathbf{u}}_v + \boldsymbol{\omega} \times \mathbf{u}_v + \dot{\boldsymbol{\omega}} \times \boldsymbol{\rho} + \boldsymbol{\omega} \times \boldsymbol{\omega} \times \boldsymbol{\rho} \quad (2.22)$$

The terms containing ρ can be collected into a single expression representing the accelerations induced by the offset of the IMU from the aircraft CG:

$$\frac{\mathrm{d}}{\mathrm{d}t}\mathbf{u}_a = \dot{\mathbf{u}}_v + \boldsymbol{\omega} \times \mathbf{u}_v + \mathbf{b}(\boldsymbol{\rho}) \tag{2.23}$$

Finally the accelerometer measurement model can be written as:

$$\mathbf{z}_a = \mathrm{diag}(\boldsymbol{\alpha})\left[\dot{\mathbf{u}}_v + \boldsymbol{\omega} \times \mathbf{u}_v + \mathbf{b}(\boldsymbol{\rho}) - \mathbf{T}\mathbf{g}\right] + \mathbf{b}_a + \mathbf{n}_a \tag{2.24}$$

Sensor biases and the accelerometer scale factor are assumed to vary by a random walk model with zero mean Gaussian driving terms.

$$\dot{\boldsymbol{\alpha}} = \mathbf{n}_\alpha \tag{2.25}$$

$$\dot{\mathbf{b}}_a = \mathbf{n}_{b_a} \tag{2.26}$$

$$\dot{\mathbf{b}}_\omega = \mathbf{n}_{b_\omega} \tag{2.27}$$

i.e. $\mathbf{n}_{(\cdot)} \sim \mathcal{N}(0, \boldsymbol{\Sigma}_{(\cdot)})$.

2.2.4 Vision Model

The camera is assumed to be fixed to the aircraft with known offset $\triangle\mathbf{s}$ from the CG and known angular offset from the body-fixed frame, defined by a transformation $\mathbf{T}_{cam}$. The camera x-axis is perpendicular to the image plane (coordinate frames are defined in Figure 2.2).

A pinhole camera model (Figure 2.3) describes the projection of a vector onto the image plane as

$$\mathbf{z} = \frac{f}{x}\begin{bmatrix} y \\ z \end{bmatrix} \tag{2.28}$$

where f is the focal length and $[x\ y\ z]^T$ is the vector (expressed in the camera frame). The focal length f can be normalized without loss of generality.

For cameras with “standard” field of view (less than approximately $70°$) this model is sufficient. In wide field of view cameras ($\gtrsim 90°$) this model becomes problematic. The pinhole projection model becomes ill-conditioned for vectors which are close to $90°$ away from the optical axis (the component x of the vector expressed in the camera frame approaches 0). To improve conditioning and to express bearings as azimuth and depression (in the coordinate frames used here a positive angle is down with respect to the optical axis) measurements are modeled as arctangents of the projection onto the image plane (Figure 2.3). For the i^{th} landmark the vision measurement model $g_{2,i}$ is:

$$\mathbf{z}_{cam,i} = \begin{bmatrix} \arctan\frac{s_{i,y}}{s_{i,x}} \\ \arctan\frac{s_{i,z}}{s_{i,x}} \end{bmatrix} + \mathbf{n}_c \tag{2.29}$$

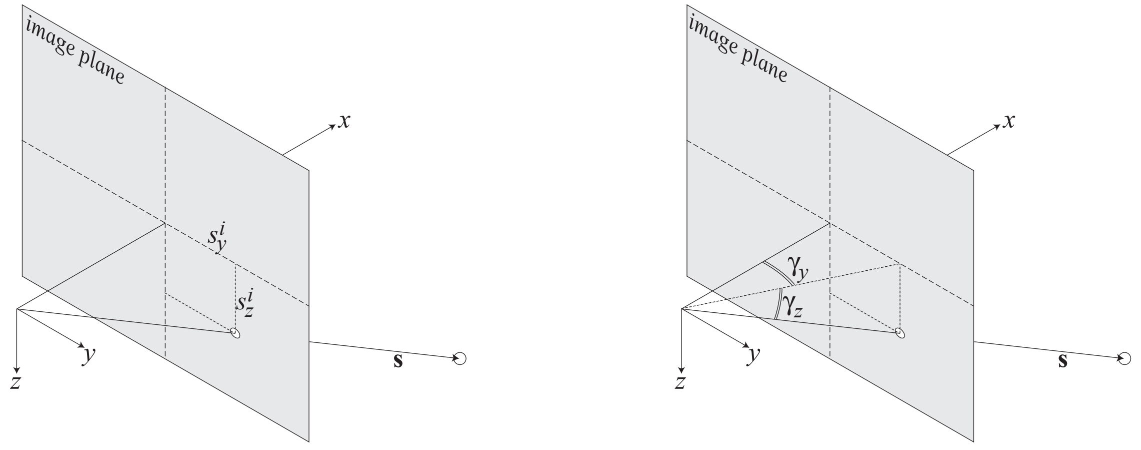

(a) Pinhole model.

(b) Modified pinhole model.

Figure 2.3: Projection models.

Rather than express the pinhole projection as vector components in the image plane (left image), the projection is expressed as an azimuth and depression to the feature (right image). This leads to better conditioning of the measurement model.

The measurement is corrupted by zero-mean Gaussian noise $\mathbf{n}_c$. $\mathbf{s}_i$ represents the vector from the camera to the i^{th} tree, expressed in the camera frame:

$$\mathbf{s}_i = \mathbf{T}_{cam}\left[\mathbf{T}\begin{bmatrix} x_i - x \\ y_i - y \\ z_i - z \end{bmatrix} - \triangle\mathbf{s}\right] \tag{2.30}$$

When vision measurements to several landmarks are available the vision measurement vector is formed by concatenating the available measurements, i.e. $\mathbf{z}_{cam} = \left[\mathbf{z}_{cam,1}^T\ \mathbf{z}_{cam,2}^T\ \dots\ \mathbf{z}_{cam,m}^T\right]^T$.

2.3 Nonlinear Estimation

In general estimators follow a recursive process of prediction (governed by a plant model) followed by correction (governed by a measurement model). The equations describing vehicle kinematics and the available measurements are highly nonlinear. In addition, the uncertainty in estimated states is likely to be significant due to the noise characteristics of low-cost IMUs. The combination of significant nonlinearities and large uncertainty greatly complicates the state estimation problem. This section briefly discusses and compares three techniques for nonlinear estimation: the Particle Filter, the Extended Kalman Filter and the Sigma Point Kalman Filter (sometimes called the Unscented Kalman Filter). Its purpose is to motivate the application of a SP-KF to an estimation problem with the types of nonlinearities as those seen in this research (i.e. trigonometric functions).

For linear systems subject to Gaussian noise and whose state variables can be accurately described with Gaussian probability distribution functions the Kalman Filter is the optimal solution to the estimation problem. The Kalman Filter has been extensively described in the literature, and textbooks such as Kailath [24] provide in-depth derivations.

However, optimal solutions to nonlinear estimation problems have proven to be difficult to obtain. In most cases approximations are required, and these approximations greatly reduce any claims of optimality or in some cases even convergence. These approximations can be categorized into *probability distribution approximations* or *system approximations*. For example, Particle Filters approximate the distribution with a large group of particles, Extended Kalman Filters approximate the system with a linearization.

It is often assumed that random variables obey a Gaussian probability distribution. In Kalman filters it is further assumed that the probability distribution remains Gaussian after propagation through the system equations (for linear systems this is true). For nonlinear functions that have extrema (for example trigonometric functions such as $\sin\theta$) the assumption of preservation of Gaussian-ness is false at the extrema.

Trigonometric functions appear in coordinate transformations in both the inertial measurement model described in Section 2.3.3 and the vision model described in Section 2.3.4. The remainder of this section uses the function $f(\theta) = -\sin\theta$ as an example to illustrate the propagation of a Gaussian random variable $\theta \sim \mathcal{N}(\bar{\theta}, \sigma_\theta)$ through a trigonometric function using a Particle Filter, linearization (as would occur in an EKF) and a sigma point transform (as would occur in a SP-KF). The effect of assuming that $f(\theta)$ is Gaussian and of linearization of $\sin\theta$ will be illustrated.

These techniques are then compared in a single time-update step for a planar non-holonomic vehicle, a simplified model of the aircraft kinematic model used in this research.

2.3.1 Particle Filters

A particle filter represents a probability distribution as a family of particles sampled randomly from the desired probability distribution function (PDF). In principle any PDF can be modeled, avoiding the necessity of assuming a specific PDF. In addition noise can have an arbitrary PDF.

In the prediction step the particles are propagated through the nonlinear process equations. When measurements are available each particle is assigned a weight based on how closely the measurement prediction for that particle matches the actual measurement (i.e. a close match means the particle is likely to represent the true system state). These weights are then used to resample the family of particles: those with high weight are likely to be selected for continued propagation, those with low weight are not likely to be selected.

The accuracy of the particle filter is directly related to the number of particles used to represent the PDF. In principle it becomes arbitrarily accurate as the number of particles is increased (in practice there are still some issues being researched) at the cost of increased computation. For

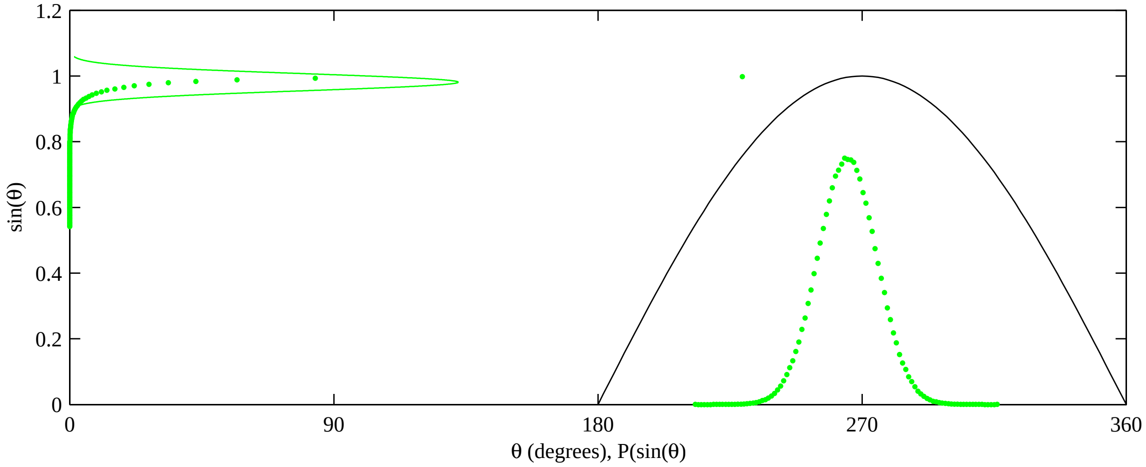

Figure 2.4: Particle representing a Gaussian PDF propagated through sine function.

The black solid line represents $-\sin\theta$*, the dotted green "bell" represents a histogram of a Gaussian* PDF *with mean* $265°$ *and standard deviation* $10°$ *(scaled to fit plot). The dotted green curve along the vertical axis represents a histogram of the Gaussian* PDF *propagated through* $f(\theta) = -\sin\theta$ *(scaled to fit plot). The solid green "bell" represents a Gaussian* PDF *with the same mean and standard deviation as the* PDF *of* $-\sin\theta$*.*

systems with many states the number of particles required to adequately model the PDF generally precludes real time implementation, but they serve as a useful benchmark by which the EKF and SP-KF can be judged.

Figure 2.4 shows the propagation of a Gaussian PDF $\theta \sim \mathcal{N}(265°, 10°)$ through the function $f(\theta) = -\sin\theta$ using a particle representation with 10^6 particles. Note that the resulting distribution is not Gaussian, and that a Gaussian approximation to the resulting PDF is not particularly accurate. However, for values of $\bar{\theta}$ sufficiently far from the extrema of f (i.e. several standard deviations) the assumption of Gaussian-ness of $f(\theta)$ will be approximately true.

The assumption that Gaussian PDFs remain Gaussian after propagation through the system equations is in common practice and in most cases performance of the resulting estimators is good.

2.3.2 Extended Kalman Filter

An Extended Kalman Filter approximates nonlinear system models with a first-order Taylor series approximation about the current best estimate. This linearization introduces errors in several ways: first, a potentially highly nonlinear system is approximated with a linear model; second, the linearization occurs about an uncertain state, hence the linearization itself may be incorrect. In estimation problems the linearization error becomes problematic when the system cannot be accurately approximated by a first order Taylor series over the span of uncertainty in the states.

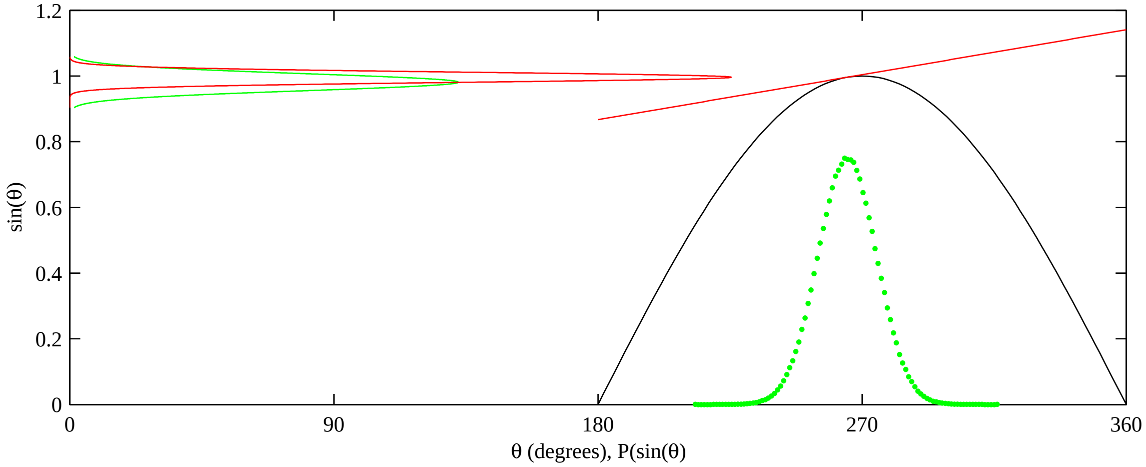

Figure 2.5: Linearized propagation of random variable through sine function

The black solid line represents $-\sin\theta$*, the dotted green "bell" represents a histogram of a Gaussian* PDF *with mean* $265°$ *and standard deviation* $10°$ *(scaled to fit plot). The straight red line denotes the linearization of* $f(\theta) = -\sin\theta$ *at* $265°$*. The solid red "bell" represents the mapping of* $\theta \sim \mathcal{N}(265°, 10°)$ *through the linearization of* $-\sin\theta$*. For comparison, the solid green "bell" is the Gaussian approximation of the particle filter.*

Figure 2.5 shows the propagation of $\theta \sim \mathcal{N}(265°, 10°)$ through the linearized model of the function $f(\theta) = -\sin\theta$. In comparison with the Gaussian approximation of the particle filter, the system linearization shows both a bias in the mean and smaller uncertainty. This bias and smaller uncertainty will be exacerbated both as θ approaches the extrema of the sine function and as the uncertainty in θ is increased.

This indicates that in some cases linearization of the system equations results in both a bias and an artificial increase in the certainty associated with an estimate.

2.3.3 Sigma Point Filters

Rather than approximate the nonlinear system equations, an UKF [23] [55] instead approximates the probability distribution of the state which is to be estimated. In contrast with a particle filter, which makes no assumption about the PDF, Sigma Point Filters assume a Gaussian PDF of the state variables, which allows a greatly reduced set of particles to model the PDF. The probability distribution is represented by a set of *Sigma Points* which capture the mean and covariance of a random vector $\mathbf{x} = \mathcal{N}(\bar{\mathbf{x}}, \mathbf{P})$:

$$\mathbf{X} = \left[\begin{array}{ccc} \bar{\mathbf{x}} & \bar{\mathbf{x}} + \eta\sqrt{\mathbf{P}} & \bar{\mathbf{x}} - \eta\sqrt{\mathbf{P}} \end{array} \right] \tag{2.31}$$

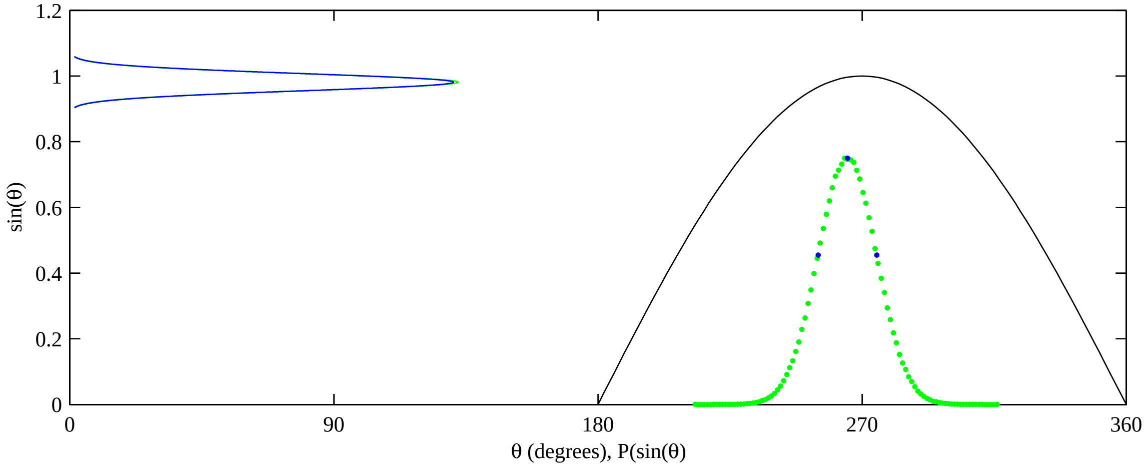

Figure 2.6: Unscented transform

The black solid line represents $-\sin\theta$*, the dotted green "bell" represents a histogram of a Gaussian* PDF *with mean* $265°$ *and standard deviation* $10°$ *(scaled to fit plot). The three blue dots on the bell denote the three Sigma points which represent* θ*. The solid blue bell on the vertical axis denotes the* PDF *recovered from the propagated Sigma points. It almost exactly covers the solid green "bell" representing the Gaussian approximation of the particle filter.*

Here η is a scale factor and $\sqrt{\mathbf{P}}$ is an orthogonal matrix square root of the covariance of the distribution [2]. These Sigma Points are propagated through the full nonlinear system equations and the estimate mean and covariance are then recovered.

Figure 2.6 shows the propagation of $\theta \sim \mathcal{N}(265°, 10°)$ through $-\sin\theta$ using three Sigma points. With only three Sigma points the Gaussian approximation of the particle filter is captured almost exactly.

Sigma point Kalman filters follow the familiar pattern of prediction followed by correction. The algorithm in [54] is reproduced in Figure 2.7.

2.3.4 Comparison of Techniques

The effect of both the assumption of preservation of Gaussian-ness and the EKF's linearization error can be seen using a single prediction step for the motion of a 2D non-holonomic vehicle (a simplified

[2] Note that this matrix square root is not unique: it can be chosen based on issues such as numerical stability, computational cost or to exploit known structure in the problem (Huster [18] makes use of this property: he chooses sigma points so that the range to the target is always positive).

initialize with $\hat{\mathbf{x}}_0$ and $\mathbf{P}_{0|0}$.

For t_k, $k \in (1, \ldots, \infty)$ compute sigma points:

$$\mathbf{X}_{k-1|k-1} = \left[\begin{array}{ccc} \hat{\mathbf{x}}_{k-1|k-1} & \hat{\mathbf{x}}_{k-1|k-1} + \eta\sqrt{\mathbf{P_{k-1|k-1}}} & \hat{\mathbf{x}}_{k-1|k-1} + \eta\sqrt{\mathbf{P_{k-1|k-1}}} \end{array} \right] \quad (2.32)$$

Time update (prediction):

$$\mathbf{X}_{k|k-1} = f(\mathbf{X}_{k-1|k-1}, \mathbf{u}_{k-1}) \quad (2.33)$$

$$\hat{\mathbf{x}}_{k|k-1} = \mathbf{X}_{k|k-1}\mathbf{w}_m \quad (2.34)$$

$$\mathbf{P}_{k|k-1} = \left[\mathbf{X}_{k|k-1} - \hat{\mathbf{x}}_{k|k-1}\mathbf{1}\right]^T \mathbf{W}_c \left[\mathbf{X}_{k|k-1} - \hat{\mathbf{x}}_{k|k-1}\mathbf{1}\right] + \mathbf{Q} \quad (2.35)$$

Measurement update (correction):

$$\mathbf{Z}_{k|k-1} = h(\mathbf{X}_{k|k-1}) \quad (2.36)$$

$$\hat{\mathbf{z}}_{k|k-1} = \mathbf{Z}_{k|k-1}\mathbf{w}_m \quad (2.37)$$

$$\mathbf{P}_{zz} = \left[\mathbf{Z}_{k|k-1} - \hat{\mathbf{z}}_{k|k-1}\mathbf{1}\right]^T \mathbf{W}_c \left[\mathbf{Z}_{k|k-1} - \hat{\mathbf{z}}_{k|k-1}\mathbf{1}\right] + \mathbf{R} \quad (2.38)$$

$$\mathbf{P}_{xz} = \left[\mathbf{X}_{k|k-1} - \hat{\mathbf{x}}_{k|k-1}\mathbf{1}\right]^T \mathbf{W}_c \left[\mathbf{Z}_{k|k-1} - \hat{\mathbf{z}}_{k|k-1}\mathbf{1}\right] \quad (2.39)$$

$$\mathbf{K} = \mathbf{P}_{xz}\mathbf{P}_{zz}^{-1} \quad (2.40)$$

$$\hat{\mathbf{x}}_{k|k} = \hat{\mathbf{x}}_{k|k-1} + \mathbf{K}(\mathbf{z}_k - \hat{\mathbf{z}}_{k|k-1}) \quad (2.41)$$

$$\mathbf{P}_{k|k} = \mathbf{P}_{k|k-1} - \mathbf{K}\mathbf{P}_{zz}\mathbf{K}^T \quad (2.42)$$

There are $2N + 1$ sigma points, where N is the dimension of the state vector. In this algorithm η is a weight factor, $\mathbf{w}_m$ is a vector of weights, $\mathbf{W}_c$ is a diagonal matrix of weights, $\mathbf{1}$ is a $(1 \times 2N + 1)$ matrix of ones, $\mathbf{Q}$ is process noise and $\mathbf{R}$ is measurement noise. The weight factors are calculated as

$$\eta = \alpha\sqrt{N} \quad (2.43)$$

The constant α is a parameter which determines the spread of the sigma points. Typically $10^{-4} \leq \alpha \leq 1$. The weight vector $\mathbf{w}_m$ and weight matrix $\mathbf{W}_c$ are

$$\mathbf{w}_{m,1} = \tfrac{\alpha^2 - 1}{\alpha^2} \qquad \mathbf{w}_{m,i} = \tfrac{1}{2N\alpha^2} \quad (2.44)$$

$$\mathbf{W}_{c,1} = \tfrac{\alpha^2 - 1}{\alpha^2} + (1 - \alpha^2 + \beta) \qquad \mathbf{W}_{c,ii} = \tfrac{1}{2N\alpha^2} \quad (2.45)$$

where $i = 2, \ldots, (2N + 1)$. The parameter β incorporates prior knowledge of the distribution of the state vector. For Gaussian distributions $\beta = 2$ is optimal [54].

Figure 2.7: Algorithm for Unscented Kalman Filter.

reproduced from Rudolph van der Merwe and Eric Wan, ”The Square Root Unscented Kalman Filter for State and Parameter Estimation”, IEEE International Conference on Acoustics, Speech and Signal Processing, *Salt Lake City, UT, 2001.*

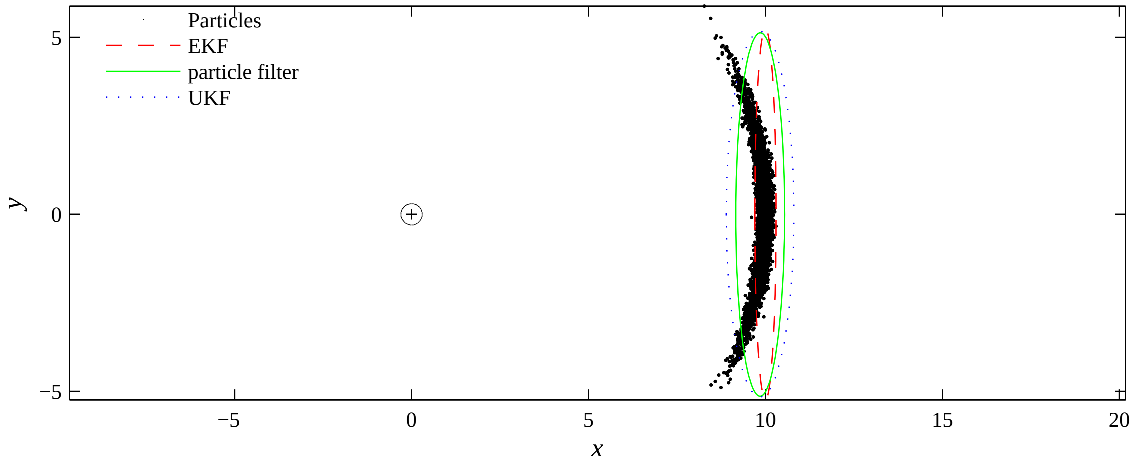

Figure 2.8: Single time update for non-holonomic vehicle.

Nominal initial vehicle position is at the origin, aligned with x axis. Initial uncertainty is 1cm in position and 10° in heading. Black dots show particles propagated through motion equations, solid green ellipsoid shows 3σ uncertainty of Gaussian approximation of particles. Dashed red ellipsoid shows EKF *computation of motion, dotted blue ellipsoid shows Sigma Point computation of motion.*

model of the aircraft kinematics used in this dissertation). Vehicle motion is modeled as

$$\begin{bmatrix} x_{k+1} \\ y_{k+1} \\ \psi_{k+1} \end{bmatrix} = \begin{bmatrix} x_k + u\Delta t \cos\psi \\ y_k + u\Delta t \sin\psi \\ \psi_k + \dot{\psi}\Delta t \end{bmatrix} \tag{2.46}$$

It is assumed that perfect odometry is available (i.e. $u\Delta t = 10$ and $\dot{\psi}\Delta t = 0$ are known precisely).

Figure 2.8 shows a single time-update step for a particle filter, a Gaussian approximation to the particle filter, an EKF, and a SP-KF. The vehicle begins at the origin with initial position uncertainty of 1cm and initial heading uncertainty of 10°. The particle filter results show the distinct 'banana' shape of the PDF of the predicted vehicle position. Ellipses show 3σ uncertainty for the Gaussian approximation (solid green), EKF (dashed red), and SP-KF (dotted blue).

The propagation of the mean and covariance through the linearized equations of the EKF introduces a bias in the vehicle position and causes the uncertainty in vehicle position (i.e. the covariance) to be significantly under predicted. The SP-KF comes significantly closer to the Gaussian approximation, almost exactly computing the mean and slightly over predicting the uncertainty. The computation cost of the SP-KF is similar to the EKF solution.

Another, more detailed, comparison of estimation techniques applied to a bearings-only tracking problem is provided by Huster [18]. That comparison shows that the EKF fails to compute a converged estimate of system state, while the SP-KF implementation computes an estimate almost identical to a particle filter implementation.

2.4 Summary: The Estimation Problem

To operate successfully in cluttered environment the UAV must maintain controlled flight, avoid collisions with obstacles and navigate to a goal location. This requires knowledge of vehicle orientation and speed, obstacle relative position and vehicle position. This must be computed using information provided by the IMU (i.e. noisy, biased measurements of acceleration and angular rate) and the vision system (noisy measurements of bearings to obstacles). Because of the possibility of drift, IMU biases must also be computed.

This can be performed with a recursive estimator which computes an estimate of system state (i.e. the vehicle state as defined in Equation 2.1 and obstacle positions) and the associated covariance:

$$\hat{\mathbf{x}} = \begin{bmatrix} \hat{\mathbf{x}}_v \\ \hat{\mathbf{x}}_o \end{bmatrix} \tag{2.47}$$

$$\mathbf{P} = \begin{bmatrix} \mathbf{P}_{vv} & \mathbf{P}_{vo} \\ \mathbf{P}_{ov} & \mathbf{P}_{oo} \end{bmatrix} \tag{2.48}$$

Because of the high degree of uncertainty associated with the disturbances acting on a small UAV a kinematic model driven by inertial measurements is used as the plant model. The use of an inertial-measurement driven kinematic model means that the same sensor package and estimator can, in principle, be used with different classes of vehicle (for example autonomous ground vehicles or underwater vehicles).

Both the inertial measurement model and the vision model are highly nonlinear. Vehicle orientation (expressed as Euler angles) accounts for nonlinearities in both the inertial model and the vision model due to the transformations of vectors between coordinate frames. The modified pinhole model which projects the three-dimensional world onto the camera's two dimensional image plane causes further nonlinearities in the vision model.

The linearized system equations used by the EKF causes a bias in the propagated mean of a Gaussian PDF and computes a decreased propagated covariance. This suggests that EKF-based estimators are likely to fail when trigonometric functions are a significant source of nonlinearities in the system equations.

In contrast, the mean and covariance of a Gaussian PDF propagated through the nonlinear equations using Sigma Points accurately models the true mean and covariance. This suggests that a SP-KF is a good candidate for solving estimation problems which contain trigonometric functions.

A solution of the estimation problem using the SP-KF is given in Chapter 3 and simulation results presented in Chapter 4 verify the consistency of the estimator.

Chapter 3

Estimator Design

THIS CHAPTER DESCRIBES in detail the inertial/vision navigation filter developed in this research. The process of computing vehicle state and obstacle positions using inertial measurements and bearings is a Simultaneous Localization and Mapping (SLAM) problem. It is complicated by three factors: the nonlinearities in the system and measurement models (described in Chapter 2); the lack of observability inherent to the bearings-only measurements provided by the vision system; and by the significant uncertainty in state estimates. This chapter presents: (a) a Sigma Point Kalman Filter based implementation to solve the estimation problem; (b) a solution to the problem of data association; (c) a solution to the problem of landmark initialization; and (d) a method to incorporate absolute position measurements which may occasionally be available.

Using the system models derived in the previous chapter, a SP-KF is implemented in Section 3.1. The SP-KF is able to cope with the system nonlinearities while being tractable for real-time operation.

Data association must be computed explicitly. A two step approach is described in Section 3.2, where the first step seeks to associate features observed in the current image frame with those observed in the previous frame and the second step associates features in the current image frame with predictions obtained from the current map.

Section 3.3 describes a method for landmark initialization, where a new landmark is initialized at the intersection of the bearing to a previously unseen landmark and the ground plane.

Estimating vehicle state and obstacle positions using the techniques described here is a standalone process. However, an absolute position measurement may be sporadically available (either through a GPS measurement or because the known goal has been reached). Since errors in estimates are fully correlated, additional information about any state can be used to improve the estimates of all states. This is addressed in Section 3.4, which describes a correction step of the map.

Section 3.5 concludes this chapter with a summary of data flow in the full estimation process, including data association, landmark initialization, and estimate smoothing/correction. Results of simulations of UAV flight in cluttered environments are presented in Chapter 4 to demonstrate estimator performance, results of hardware and simulation tests using a small Unmanned Ground Vehicle are presented in Chapter 5.

3.1 Inertial/Vision Navigation Filter

As stated in Chapter 2 the vector of states to be estimated is

$$\mathbf{x} = \left[\begin{array}{ccccc} \mathbf{x}_v^T & \mathbf{x}_1^T & \mathbf{x}_2^T & \cdots & \mathbf{x}_m^T \end{array} \right]^T \tag{3.1}$$

where $\mathbf{x}_i = [x_i \; y_i \; z_i]^T$, the position of an obstacle in the inertial frame and

$$\mathbf{x}_v = \left[\begin{array}{cccccccccccc} x & y & z & \phi & \theta & \psi & u & v & w & \boldsymbol{\alpha}^T & \mathbf{b}_a^T & \mathbf{b}_\omega^T \end{array} \right]^T \tag{3.2}$$

The process model

$$\dot{\mathbf{x}} = f(\mathbf{x}, \mathbf{u}) \tag{3.3}$$

and the measurement model

$$\mathbf{z}_{imu} = g_1(\mathbf{x}, \mathbf{u}) \tag{3.4}$$

$$\mathbf{z}_{cam} = g_2(\mathbf{x}) \tag{3.5}$$

were developed in Chapter 2. This section integrates the models to form the prediction equations and the vision update equations. A summary of the estimator prediction and correction equations is given in Appendix B.

In general estimators follow a recursive process of prediction followed by correction. In many cases the prediction step is driven by a dynamic model of the system driven by known inputs and unknown disturbances, where it is assumed that the disturbances can be adequately modeled by random process noise. In this dissertation the prediction step is performed by a kinematic model driven by accelerometer and angular rate measurements. Noise in these measurements is treated as process noise.

The correction step is driven by the bearing measurements obtained from the vision system.

3.1.1 Prediction Step

Incorporating the rate gyro measurement model (Equation 2.20) into Equations 2.16–2.18 relates measurements of angular rate to the Euler angle rates:

$$\dot{\phi} = (z_p - b_p) + \tan\theta \sin\phi (z_q - b_q) - \tan\theta \cos\phi (z_r - b_r) \tag{3.6}$$

$$\dot{\theta} = \cos\phi(z_q - b_q) - \sin\phi(z_r - b_r) \tag{3.7}$$

$$\dot{\psi} = \frac{\sin\phi}{\cos\theta}(z_q - b_q) + \frac{\cos\phi}{\cos\theta}(z_r - b_r) \tag{3.8}$$

where b_p, b_q, and b_r are the rate gyro biases. The vehicle acceleration is obtained from the accelerometer model (Equation 2.24) and the rate gyro model (Equations 2.20):

$$\dot{u} = \frac{z_x}{\alpha_x} - g\sin\theta - b_x - (z_q - b_q)w + (z_r - b_r)v - b_x(\boldsymbol{\rho}) \tag{3.9}$$

$$\dot{v} = \frac{z_y}{\alpha_y} + g\cos\theta\sin\phi - b_y - (z_r - b_r)u + (z_p - b_p)w - b_y(\boldsymbol{\rho}) \tag{3.10}$$

$$\dot{w} = \frac{z_z}{\alpha_z} + g\cos\theta\cos\phi - b_z - (z_p - b_p)v + (z_q - b_q)u - b_z(\boldsymbol{\rho}) \tag{3.11}$$

$z_{(\cdot)}$ and $b_{(\cdot)}$ represent the inertial measurement and bias, respectively, along a body-fixed axis. $\alpha_{(\cdot)}$ is the accelerometer scale factor error along a body-fixed axis, g is the acceleration due to gravity and $b_{(\cdot)}(\boldsymbol{\rho})$ is the acceleration induced by the (known) offset of the IMU from the vehicle CG.

IMU biases vary as a random walk:

$$\dot{\boldsymbol{\alpha}} = \mathbf{n}_\alpha \tag{3.12}$$

$$\dot{\mathbf{b}}_a = \mathbf{n}_{b_a} \tag{3.13}$$

$$\dot{\mathbf{b}}_\omega = \mathbf{n}_{b_\omega} \tag{3.14}$$

where $\boldsymbol{\alpha} = [\alpha_x\ \alpha_y\ \alpha_z]^T$, $\mathbf{b}_a = [b_x\ b_y\ b_z]^T$ and $\mathbf{b}_\omega = [b_p\ b_q\ b_r]^T$.

Finally, obstacles are assumed to be stationary, hence

$$\dot{\mathbf{x}}_i = 0 \tag{3.15}$$

Equations 2.13–2.15, 3.6–3.8, 3.9–3.11 and 3.12–3.15 represent the kinematics of the vehicle, inertial measurement unit and obstacles. These can be written in compactly in discrete form as

$$\begin{bmatrix} \mathbf{x}_{v,k+1} \\ \mathbf{x}_{o,k+1} \end{bmatrix} = \begin{bmatrix} f_v^d(\mathbf{x}_{v,k}, \mathbf{z}_{imu,k}) \\ \mathbf{x}_{o,k} \end{bmatrix} + \begin{bmatrix} \mathbf{n}_{ext} \\ 0 \end{bmatrix} \tag{3.16}$$

The nonlinear function f_v^d captures the discrete-form kinematics of the vehicle and the IMU bias states and is driven by the inertial measurements $\mathbf{z}_{imu,k}$. The external noise term $\mathbf{n}_{ext}$ includes the assumed noise of the random walk model for the IMU scale factor and bias drift and may include an additional noise term to cover unmodeled vehicle kinematics. Inertial measurements are assumed to be corrupted by zero mean Gaussian random noise.

The system kinematic equations are used in the prediction step of the UKF algorithm reproduced in Figure 2.7. The process noise for the time update must still be obtained. In this case process noise arises from the noisy measurements of acceleration and angular rate. Process noise is approximated as

$$\mathbf{Q}_k = \begin{bmatrix} \mathbf{F}_z \Sigma_{imu} \mathbf{F}_z^T + \Sigma_{ext} & 0 \\ 0 & 0 \end{bmatrix} \tag{3.17}$$

where $\mathbf{F}_z = \nabla_{\mathbf{z}_{imu}} f_v^d$ (the Jacobian of the discrete process model with respect to the inertial measurements), Σ_{imu} is the covariance matrix describing the IMU measurement noise, and Σ_{ext} is the covariance describing the external noise, including drift of the IMU biases. This is identical to the EKF process noise approximation, and is adequate for the application being considered. Since obstacles (i.e. trees) are assumed to be perfectly stationary only components corresponding to vehicle states have non-zero process noise.

Note that measurements from the IMU are likely to be available at a much higher rate than measurements from the camera, allowing the time update to proceed at a higher rate than the vision correction.

3.1.2 Vision Update

Measurements from the camera are incorporated in the measurement update step of the estimator. The vision model reflects the projection of a vector in 3D (the vector from the vehicle to the feature) onto the 2D image plane and is represented by Equations 2.29 and 2.30. This can be written compactly as

$$\mathbf{z}_{cam,k} = g_2(\mathbf{x}_{v,k}, \mathbf{x}_{o,k}) + \mathbf{n}_c \tag{3.18}$$

Here $\mathbf{z}_{cam}$ represents bearings from the vehicle to stationary features. Measurement noise is represented by the zero-mean Gaussian random variable $\mathbf{n}_c$.

3.1.3 Choice of States

Recall from Chapter 2 that only relative obstacle position is required to avoid collision. A different state vector including vehicle state and range and bearings to obstacles instead of absolute obstacle position would also provide the information required for control and navigation. Since the vision system provides a measurement of bearing to obstacles, this would result in a linear vision update step.

However, while absolute obstacle position is constant, relative position changes continuously and is a nonlinear function of vehicle motion, resulting in a more complex prediction step. The prediction step runs at the IMU measurement rate, which is typically much higher than the vision frame rate. Computationally, estimating obstacle relative position is more expensive than estimating absolute position. Absolute obstacle position estimation has the additional benefit of immediately providing a map of obstacle positions in the inertial frame.

Hence absolute obstacle position is estimated along with vehicle position, orientation, and velocity.

3.2 Data Association

Inherent in any Kalman filter is an assumption of known data association. However, in this application (as in many SLAM implementations) landmarks are indistinguishable from one another[1], hence this must be computed explicitly. In this research it is complicated by the lack of complete measurements (i.e. bearings provide two measurements, range is not available).

A two stage process is used for data association: first, the current bearings are compared with those obtained in a previous frame to check frame to frame correspondence; second, bearings to features not seen in the previous frame are compared with predicted bearings obtained from landmarks in the map to check if the features have been seen earlier in the run. Those bearings that are not associated in either step are assumed to come from a new, previously unseen landmark.

Frame to frame association for point features is used extensively in optical flow algorithms. Typically these operate at high frame rates compared with motion of the vehicle. However, when frame rates are low and vehicle motion (especially angular motion) is large, frame to frame correlation is more complex. However, additional information to aid frame to frame association is available.

Angular rate measurements available from the IMU are integrated to obtain the change in orientation of the camera between frames. The change in orientation is used to calculate predicted bearings for features seen in the previous frame and these are compared with current measurements. While changes in position of the vehicle will also affect the predicted bearings, this is a much smaller effect than changes in orientation. Also, changes in bearing to a feature due to changes in vehicle position require a measurement of range (which is unavailable here) to the feature to compute. Hence bearing changes due to vehicle position change are not calculated but are covered by an increased uncertainty in the predicted bearing.

A bearing from the previous image is expressed as a vector in the camera frame. The rotation $\mathbf{T}_{f-f}$ between the previous frame and the current frame is computed by integrating angular rates and is used to compute the prediction of the bearing in the current frame:

$$\mathbf{c} = \mathbf{T}_{f-f} \begin{bmatrix} 1 \\ z_{y,k-1} \\ z_{z,k-1} \end{bmatrix} \tag{3.19}$$

[1] Here indistinguishable means that landmarks are not uniquely labeled. They are, however, geographically separated. This geographic separation is used to compute data association.

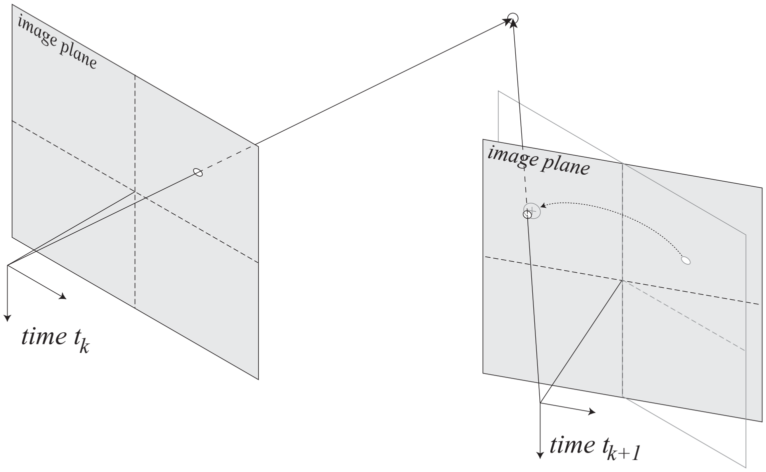

Figure 3.1: Frame to frame data association.

A bearing is obtained at t_k. The camera moves and another bearing is obtained at t_{k+1}. Rate gyro measurements are integrated to compute the camera rotation between frames and the expected bearing for t_{k+1} is computed.

The transformed vector is projected onto the image plane to determine the predicted bearing $\bar{\mathbf{z}}_k$.

$$\bar{\mathbf{z}}_k = \frac{1}{c_x} \begin{bmatrix} c_y \\ c_z \end{bmatrix} \tag{3.20}$$

Finally a gated nearest neighbor approach based on the Mahalonobis distance between the current bearing and predicted bearings is used to determine association:

$$d_{ij} = (\mathbf{z}_i - \bar{\mathbf{z}}_j)^T \mathbf{P}_{jj}^{-1} (\mathbf{z}_i - \bar{\mathbf{z}}_j) \tag{3.21}$$

The matrix $\mathbf{P}_{jj}$ is the covariance associated with the predicted bearing $\bar{\mathbf{z}}_j$ and includes measurement uncertainty, uncertainty induced by the transformation and a term to cover the change in bearing due to vehicle position change, which is not incorporated explicitly.

Features which are not associated with landmarks in the frame-frame association step are passed to the frame-map association step. The frame to map association compares a current bearing with the predicted bearings computed using the current state estimate (Equations 2.36–2.38 in Figure 2.7).

$$d_{ij} = (\mathbf{z}_i - \hat{\mathbf{z}}_j)^T \mathbf{P}_{zz,jj}^{-1} (\mathbf{z}_i - \hat{\mathbf{z}}_j) \tag{3.22}$$

The Mahalanobis distance is computed to assess the likelihood that a bearing is associated with a particular prediction and a gated nearest neighbor approach is used to assign bearings to map landmarks.

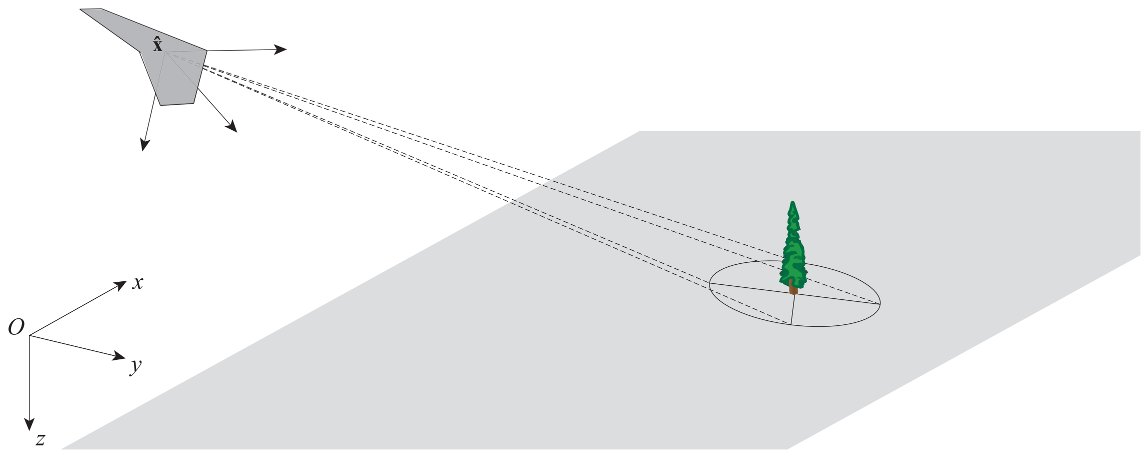

Figure 3.2: Landmark initialization.

A landmark is initialized at the intersection of the vector from the vehicle to the previously unseen landmark and the ground plane. The uncertainty is computed by projecting the uncertainty in the vector onto the ground plane.

This two-step approach to data association is more robust to dropouts of individual features (which may be due to occlusion or to features which are on the edge of the vision system's detection envelope) and enables more accurate association when landmarks have not yet been accurately localized.

3.3 Landmark Initialization

Features which are not associated with known landmarks are assumed to come from new, previously unseen landmarks.

In the current implementation landmarks are assumed to lie on the ground plane. Using the estimate of the vehicle's altitude, a new landmark is initialized at the intersection of the ground plane and a vector from the vehicle along the bearing to the previously unseen landmark (obtained from the vision system). This is shown schematically in Figure 3.2.

In the camera frame, a vector to the landmark is

$$\boldsymbol{\gamma}^C = \begin{bmatrix} 1 \\ \arctan z_y^c \\ \arctan z_z^c \end{bmatrix} \tag{3.23}$$

This can be transformed to the inertial frame by

$$\boldsymbol{\gamma}^O = \mathbf{T}^{-1}\left[\mathbf{T}_{cam}^{-1}\boldsymbol{\gamma}^C + \triangle\mathbf{s}\right] \tag{3.24}$$

where $\mathbf{T}_{cam}$ is known and $\mathbf{T}$ is computed from the estimates of Euler angles. Uncertainty is present in both the bearing measurement $[z_y \; z_z]^T$ and the vehicle orientation (described by $\mathbf{T}$). The vector $\boldsymbol{\gamma}^O$ points from the vehicle to the landmark. The landmark position can now be computed from the intersection of this vector with the ground plane, since

$$\boldsymbol{\gamma}^O = \gamma \begin{bmatrix} x_i - x \\ y_i - y \\ z_i - z \end{bmatrix} \tag{3.25}$$

where $[x \; y \; z]^T$ denotes the vehicle position in the inertial frame, $[x_i \; y_i \; z_i]^T$ denotes the landmark position in the inertial frame and γ is a scale factor. All landmarks are assumed to lie on the ground plane, hence $z_i \sim \mathcal{N}(z_g, \Sigma_g)$. Therefore:

$$\gamma = \frac{\gamma_z^O}{z_g - z} \tag{3.26}$$

$$x_i = \frac{\gamma_x^O}{\gamma} + x \tag{3.27}$$

$$y_i = \frac{\gamma_y^O}{\gamma} + y \tag{3.28}$$

The uncertain parameters leading to the three equations above are: vehicle position x, y, z; ground plane height z_g; vehicle orientation ϕ, θ, ψ (through the transformation in Equation 3.24); and bearings z_y^C, z_z^C.

A sigma-point transform can be used to project the bearing and its associated uncertainty onto the ground plane. First a state vector is assembled from the current estimate of vehicle position and orientation, the ground plane height and the bearing measurements:

$$\boldsymbol{\xi} = \begin{bmatrix} x & y & z & \phi & \theta & \psi & z_g & z_y^C & z_z^C \end{bmatrix}^T \tag{3.29}$$

Similarly a covariance matrix is assembled:

$$\mathbf{P}_\xi = \begin{bmatrix} \mathbf{P}_{vv} & 0 & 0 \\ 0 & \Sigma_g & 0 \\ 0 & 0 & \mathbf{R} \end{bmatrix} \tag{3.30}$$

where $\mathbf{P}_{vv}$ is the 6×6 covariance associated with the current estimate of vehicle position and orientation, Σ_g is the variance of the uncertainty associated with the ground plane height and $\mathbf{R}$ is the covariance of the uncertainty associated with the bearing measurement.

Using this state vector and associated covariance, a set of Sigma Points is computed using Equation 2.32. The Sigma Points are propagated through Equations 3.23–3.28 and finally the estimated landmark position $\hat{\mathbf{x}}_{new}$ and associated covariance $\mathbf{P}_{new}$ are computed using Equations 2.34 and 2.35. The system state vector is then augmented with the new landmark:

$$\hat{\mathbf{x}}_{k|k} = \begin{bmatrix} \hat{\mathbf{x}}_{k|k} \\ \hat{\mathbf{x}}_{new} \end{bmatrix} \qquad \mathbf{P}_{k|k} = \begin{bmatrix} \mathbf{P}_{k|k} & 0 \\ 0 & \mathbf{P}_{new} \end{bmatrix} \tag{3.31}$$

While the augmented state covariance is initially block diagonal, the uncertainty in the new landmark position quickly becomes correlated with both the vehicle state uncertainty and the uncertainty in previously observed landmark positions.

This method of landmark initialization can be extended to non-planar ground if the vehicle has a digital elevation map (DEM) of the surrounding terrain. A landmark would now get initialized at the intersection of the bearing vector and the ground as given by the DEM. There is one caveat however: as the grazing angle between the ground and the bearing becomes small the projected uncertainty will become very large. Additionally, the projected uncertainty will no longer be Gaussian, leading to potential problems when the landmark is added to the estimator.

3.4 Estimate Smoothing

Bearing measurements provide no information about vehicle absolute position or about landmark absolute position. Absolute position is therefore unobservable, and unless additional information in the form of absolute measurements are available the estimates of vehicle and landmark absolute position will drift.

In most SLAM implementations (including this one) the uncertainty in all the states becomes highly correlated over the course of vehicle motion. Hence additional information about any of the states can be used to improve the estimates of all the states. This information may come from many sources: loop closure, which consists of revisiting previously explored terrain; observation of a priori known landmarks; or sporadic GPS updates[2]. With this additional information a smoothing algorithm can correct the drift in absolute vehicle and landmark positions.

Smoothing of the full vehicle trajectory provides the most accurate correction of the map. However, this requires enough data that the vehicle trajectory can be reconstructed: this may consist of all measurements (both inertial and bearings) obtained through the trajectory or it may consist of retaining vehicle state estimates and the associated covariance throughout the trajectory (i.e. rather than only including the current vehicle state estimate in the state vector, the current state and all previous states are included). The state vector will then grow with time, as current vehicle states are

[2] Arguably observation of a priori known landmarks and GPS updates are equivalent: both are measurements to what are effectively beacons.

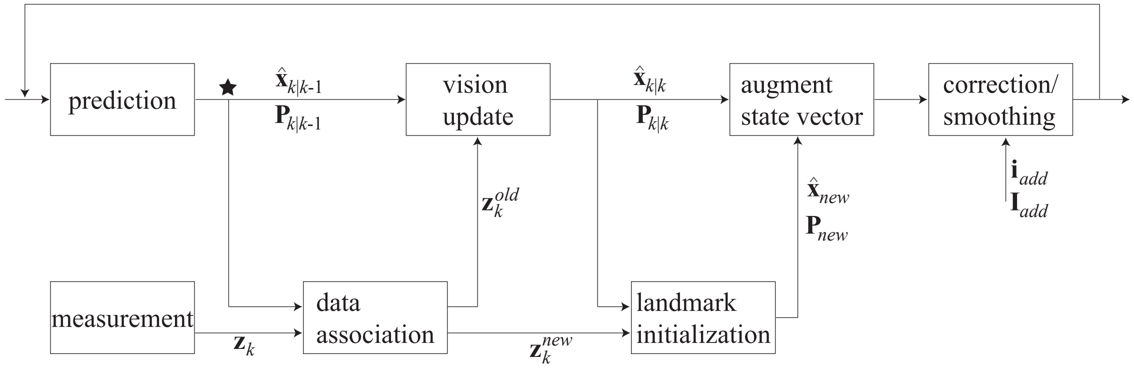

Figure 3.3: Flow of estimation.

The estimation process is initialized at the junction labeled $\star$.

added, as well as with distance, as new landmarks are observed. Both techniques greatly increase both the storage and computational requirements of the smoothing step.

Rather than smoothing the full vehicle trajectory, a correction step can be applied using only the current estimate of vehicle state and obstacle positions. This results in a less effective map correction but does not require storage of all measurements or of all previous vehicle states.

Estimation happens in the state space (i.e. $\mathbf{x}$, $\mathbf{P}$). The correction happens in information space:

$$\mathbf{I} = \mathbf{P}^{-1} \qquad \mathbf{i} = \mathbf{I}\hat{\mathbf{x}} \tag{3.32}$$

where $\hat{\mathbf{x}}$ is the current estimate of the system state and $\mathbf{P}$ is the estimated covariance. The correction step is

$$\mathbf{I}_{corr} = \mathbf{I} + \mathbf{I}_{new} \tag{3.33}$$

$$\mathbf{i}_{corr} = \mathbf{i} + \mathbf{i}_{new} \tag{3.34}$$

where $\mathbf{I}_{new}$ is the information matrix and $\mathbf{i}_{new}$ is the information vector associated with the additional state knowledge. The corrected state and covariance are then recovered:

$$\mathbf{P}_{corr} = \mathbf{I}_{corr}^{-1} \qquad \hat{\mathbf{x}}_{corr} = \mathbf{P}_{corr}\mathbf{i}_{corr} \tag{3.35}$$

3.5 Data Flow

The flow of data through the estimation process is shown schematically in Figure 3.3.

The estimator is initialized at time t_0 with

$$\hat{\mathbf{x}}_{0|-} = \mathbf{x}_0 \tag{3.36}$$

$$\mathbf{P}_{0|-} = \mathbf{P}_0 \tag{3.37}$$

If there are any landmarks known a priori, they are included in $\mathbf{x}_0$ and $\mathbf{P}_0$, otherwise only vehicle states are present in the initial state vector.

At some time t_k:

- Prediction

  Predictions of system state $\hat{\mathbf{x}}_{k|k-1}$ and covariance $\mathbf{P}_{k|k-1}$ are computed using the previous estimates of state and covariance, system kinematics (Equation 3.16) and the UKF prediction step equations (Equations 2.32–2.35).

- Measurement

  Bearings are obtained from the vision system.

- Data Association

  If there are any landmarks in the state vector, data association is performed, following the two-step process described in Section 3.3. Predicted measurements are computed using the vision model (3.18), predicted system state and covariance and UKF correction step equations (Equations 2.36–2.38). Bearings associated with known landmarks (i.e. those already in the state vector) are placed in an array $\mathbf{z}_{old}$, unassociated bearings are placed in an array $\mathbf{z}_{new}$

- Vision Update

  Bearings $\mathbf{z}_{old}$ associated with known landmarks are used to correct the prediction of system state using UKF correction step equations (Equations 2.39–2.42), producing $\hat{\mathbf{x}}_{k|k}$ and the associated covariance $\mathbf{P}_{k|k}$

- Landmark Initialization

  Using the recently corrected system state and covariance and the unassociated bearings $\mathbf{z}_{new}$, initial landmark positions $\mathbf{x}_{new}$ and covariance $\mathbf{P}_{new}$ are computed using the landmark initialization process described in Section 3.4.

- State Augmentation

  The state vector is augmented with the new landmarks so that

$$\hat{\mathbf{x}}_{k|k} = \begin{bmatrix} \hat{\mathbf{x}}_{k|k} \\ \mathbf{x}_{new} \end{bmatrix} \qquad \mathbf{P}_{k|k} = \begin{bmatrix} \mathbf{P}_{k|k} & 0 \\ 0 & \mathbf{P}_{new} \end{bmatrix} \tag{3.38}$$

- Correction/Smoothing

  If additional information is available, correct the current state estimate using Equations 3.33–3.35.

- Return to Prediction

  The process continues recursively.

Chapter 4

UAV Simulation Results

THIS CHAPTER DESCRIBES results of computer simulations of UAV flight in unknown, cluttered environments. The simulations serve two main purposes: first, to demonstrate that standard estimation techniques (i.e. the EKF) often fail to provide a convergent solution to the problem of estimating vehicle and landmark states; second, to examine the performance of the estimator, the data association algorithm and the landmark initialization algorithm presented in Chapter 3. Results of hardware tests and simulations for a small autonomous rover are described in Chapter 5.

Simulation results are presented to address: (a) estimate consistency; (b) fusion of state estimates with a trajectory planner; (c) vehicle position estimate error growth characteristics.

Results of Monte Carlo simulations of flight in a planar environment show that *consistent* estimates of system state (i.e. vehicle position, orientation and velocity, IMU biases, and obstacle positions) are computed by the UKF-based estimator presented in Chapter 3. A consistent estimator is unbiased (i.e. the mean estimate error is zero) and accurately computes the covariance of the estimate error. Conversely, a baseline EKF-based approach fails to provide reliably convergent estimates of vehicle state and obstacle positions.

Next, results of a simulation demonstrating obstacle avoidance in a cluttered planar environment are presented. This requires an obstacle avoidance algorithm. In this case a randomized motion planner used the estimates of state and covariance (i.e. the uncertainty in the estimate) to generate trajectories that minimized the probability of collision while navigating to a goal.

Simulations of UAV flight in three dimensions address the question of error growth of the vehicle position estimate. Two flight conditions are considered: exploration, where new landmarks are continually encountered; and station keeping, where the vehicle orbits a fixed point, either keeping a set of landmarks in continuous view or cyclically revisiting landmarks. For exploration flight error was a percentage of distance traveled, for station keeping flight error varied cyclically with each orbit.

When data association is known a priori the error varied inversely with the square root of the number of landmarks in view. The data association and landmark initialization algorithms presented in Sections 3.2 and 3.3, respectively, were tested by examining their effect on the vehicle position estimate error. Results showed that data association was successful as long as less than approximately five landmarks were in view.

An error in data association has the potential to cause divergence of the state estimate, and increasing the number of landmarks in view increases the likelihood of errors in data association. Moreover, estimated vehicle states are used to aid both data association and landmark initialization, hence significant coupling can be expected. Intuition therefore suggests, and simulations showed, that there is some value of number of landmarks in view which minimizes the estimate error. For the simulations conducted here, an average of 2.6 landmarks in view minimized the position estimate error for exploration flight and an average of 5 landmarks in view minimized the position error for station keeping flight.

Section 4.1 discusses estimate consistency and demonstrates a simulation of flight through a cluttered environment using 2D simulations. Section 4.2 discusses results of 3D simulations investigating vehicle position error and Section 4.3 summarizes results.

4.1 Navigation in a Plane

In this section data association and landmark initialization are assumed to be known a priori. This isolates the estimation problem, allowing a focus on consistency and comparison with an EKF-based implementation. This section shows:

1. Standard estimation techniques (i.e. the Extended Kalman Filter) fails even for the 2D case of this estimation problem.
2. The application of an Unscented Kalman Filter results in a consistent, unbiased estimator.
3. Navigation through a cluttered environment is enabled by using results of the estimator coupled with a trajectory planner.

For ease of visualization, simulations were conducted for navigation in a plane. The state vector $\mathbf{x} = [\mathbf{x}_v^T \ \mathbf{x}_1^T \ \cdots \ \mathbf{x}_m^T]^T$ contains vehicle states and obstacle positions. For the 2D case the vehicle state vector is

$$\mathbf{x}_v = \begin{bmatrix} x & y & \psi & u & v & \alpha_x & \alpha_y & b_x & b_y & b_\psi \end{bmatrix}^T \tag{4.1}$$

where x, y, ψ denote vehicle position and orientation in the inertial frame; u and v denote velocity expressed in the body frame; α_x and α_y denote accelerometer scale factor errors in the body x and y directions; and finally b_x, b_y and b_ψ denote bias errors for the accelerometer x and y

directions and the rate gyro. The obstacle position

$$\mathbf{x}_i = \left[\begin{array}{cc} x_i & y_i \end{array} \right]^T \tag{4.2}$$

includes the obstacle location in the inertial frame.

4.1.1 Estimate Consistency

Kalman filters propagate an estimate of system state and an estimate of the covariance of the estimate error. A *consistent* estimator is both unbiased (i.e. the expected value of the estimate error is zero) and accurately estimates the covariance of the estimate error:

$$\mathbb{E}(\mathbf{x}_k - \hat{\mathbf{x}}_k) = 0 \tag{4.3}$$

$$\mathbb{E}((\mathbf{x}_k - \hat{\mathbf{x}}_k)(\mathbf{x}_k - \hat{\mathbf{x}}_k)^T) = \mathbf{P}_{kk} \tag{4.4}$$

Alternatively,

$$\mathbb{E}((\mathbf{x}_k - \hat{\mathbf{x}}_k)^T(\mathbf{x}_k - \hat{\mathbf{x}}_k)) = Tr(\mathbf{P}_{kk}) \tag{4.5}$$

Hence to evaluate consistency of the navigation solution one can compare the 2-norm of the estimate error with the square root of the trace of the covariance matrix. This can be done using Monte Carlo simulations.

4.1.2 System Equations for the Planar Case

As with the 3D case the time update step is represented by vehicle kinematics, driven by inertial measurements.

$$\dot{x} = \cos\psi u - \sin\psi v \tag{4.6}$$

$$\dot{y} = \sin\psi u + \cos\psi v \tag{4.7}$$

$$\dot{\psi} = z_r - b_r \tag{4.8}$$

$$\dot{u} = \frac{z_x}{\alpha_x} - b_x + (z_r - b_r)v - b_x(\boldsymbol{\rho}) \tag{4.9}$$

$$\dot{v} = \frac{z_y}{\alpha_y} - b_y - (z_r - b_r)u - b_y(\boldsymbol{\rho}) \tag{4.10}$$

Here $[z_x\ z_y\ z_\psi]^T$ represent the measured acceleration and angular rate. $b_{(\cdot)}(\boldsymbol{\rho})$ is the acceleration induced by the (assumed known) offset of the IMU from the vehicle CG and angular rate and angular acceleration.

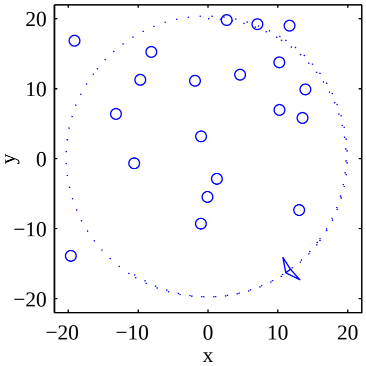

Figure 4.1: Nominal data for 2D Monte Carlo simulations.

Schematic of a single run of the Monte Carlo simulation. Aircraft speed is 10m/s, turn rate is 0.5rad/s, resulting in a turn radius of 20m. The aircraft travels a distance of 200m, approximately 1.6 times around the circular path.

The 2D vision measurement model is

$$z_i = \arctan \frac{s_{i,y}}{s_{i,x}} + n_c \tag{4.11}$$

where n_c is zero mean Gaussian noise and $s_{i,x}$ and $s_{i,y}$ are the components of the vector from the vehicle to the landmark expressed in the camera frame:

$$\mathbf{s}_i = \mathbf{T}_{cam} \left[\mathbf{T} \begin{bmatrix} x_i - x \\ y_i - y \end{bmatrix} - \triangle\mathbf{s} \right] \tag{4.12}$$

The offset between the camera and the vehicle CG is $\triangle\mathbf{s}$. The rotation matrix $\mathbf{T}_{cam}$ transforms a vector from the body frame to the camera frame, the rotation matrix $\mathbf{T}$ transforms a vector from the inertial frame to the body frame:

$$\mathbf{T} = \begin{bmatrix} \cos\psi & \sin\psi \\ -\sin\psi & \cos\psi \end{bmatrix} \tag{4.13}$$

As with the full 3D system equations, the 2D case of state estimation is highly nonlinear.

4.1.3 Monte Carlo Simulation Results

The UAV is flown in a circular trajectory of radius 20m at a velocity of 10m/s through a forest of randomly distributed trees (see Figure 4.1). A new forest was generated for each run. UAV position and velocity was assumed to be known accurately at the start of each run ($\sigma^2 = 1 \times 10^{-6}$) and landmark positions were assumed to be known with a standard deviation of 1m (i.e. an initial, but

Table 4.1: IMU initialization parameters for 2D simulations.

	α_x	α_y	b_x	b_y	b_ψ
mean	1	1	0.15	0.10	0.004
σ	0.01	0.01	0.1	0.1	0.02

uncertain, map was provided for each run). Estimates of IMU biases were initialized with a Gaussian random number using parameters given in Table 4.1.

Since the purpose of the estimator is to determine vehicle state and obstacle positions with an accurate assessment of the estimate error, success of a run is determined by comparing the estimated standard deviation of the error with the true standard deviation of the error. These are:

$$\sigma_{k,est} = \sqrt{Tr\mathbf{P}_{kk}} \tag{4.14}$$

$$\sigma_{k,truth} = \sqrt{(\hat{\mathbf{x}}_k - \mathbf{x}_k)^T(\hat{\mathbf{x}}_k - \mathbf{x}_k)} \tag{4.15}$$

Where for a consistent estimator $\mathbb{E}\sigma_{k,est} = \mathbb{E}\sigma_{k,truth}$ (Equation 4.5).

Results of a 1000 run Monte Carlo simulation are shown graphically in Figure 4.2. Each plot shows the envelope of the true variance of estimate error (i.e. the minimum and maximum values of the 2-norm of the estimate error over all runs at each time step) as a grey region, the mean of the true variance of estimate error at each time step as a blue line and the mean of the estimated error variance (i.e. $\sqrt{Tr\mathbf{P}_{kk}}$) at each time step as a dashed red line. The EKF implementation (upper plot) shows clear divergence of the estimate, with true variance an order of magnitude greater than the estimated variance. Conversely the UKF implementation (lower plot) shows a well-behaved estimator with the expectations of true and estimated variance aligned and a narrow envelope of true variance.

A run is ultimately deemed successful if the estimate error at the end of the run is less than the estimate error at the state of the run (i.e. information has been gained about the vehicle and the environment):

$$\sigma_{K,truth} < \sigma_{1,truth} \tag{4.16}$$

Figure 4.3 shows a cumulative distribution plot of the error ratio $\frac{\sigma_{K,truth}}{\sigma_{1,truth}}$ for the UKF-based implementation (solid blue line) and the EKF-based implementation (dashed red line) for 1000 runs. All of the UKF-based estimators resulted in improved knowledge of the environment, only 205 EKF-based estimators resulted in improved knowledge of the environment.

The estimated state covariance is an assessment of the uncertainty in the estimates of the state variables. It can be used in trajectory planning to generate paths which minimize the probability of collisions with obstacles, hence accurate estimation of the estimate error covariance is an important characteristic of a successful estimator.

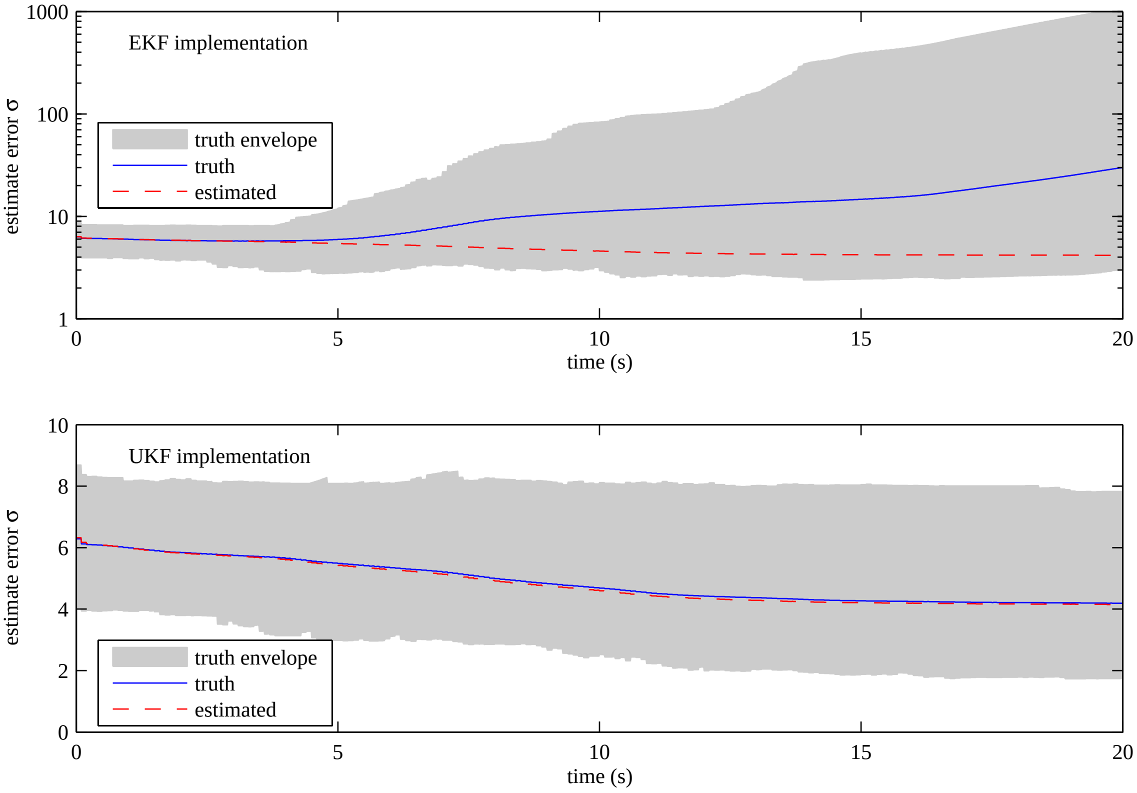

Figure 4.2: Estimator consistency for 2D navigation.

A comparison of estimated standard deviation of the estimate error and true standard deviation of the estimate error for the EKF *implementation (above) and* UKF *implementation (below). Note the difference in scales. Results are from a 1000 run Monte Carlo simulation. The mean of the true standard deviation of estimate error is shown in blue, mean of estimated standard deviation of estimate error is shown in red. The shaded area represents the envelope of the true error variance over 1000 runs.*

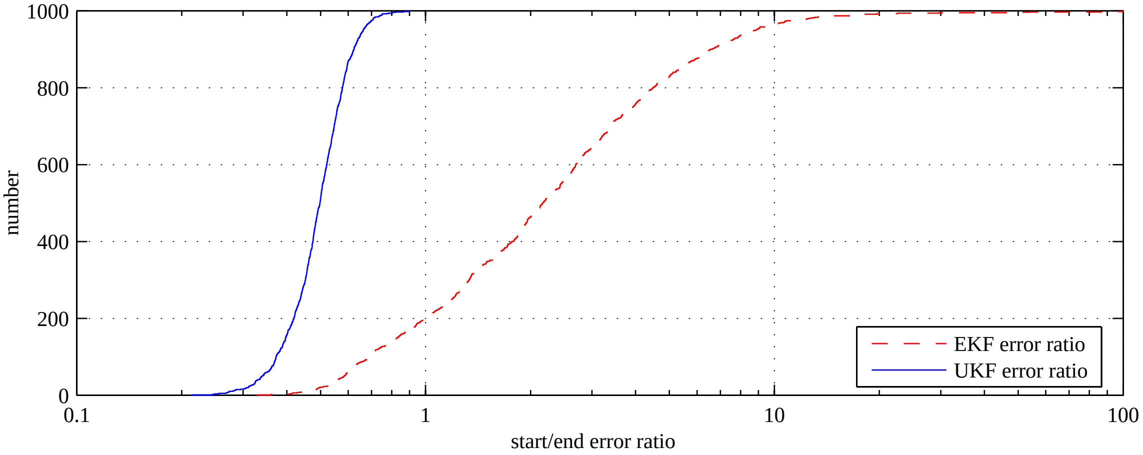

Figure 4.3: Change in estimate error over course of run.

A cumulative distribution plot of the number of runs which resulted in a reduction in estimate error over the course of each run. All UKF *runs resulted in a reduction in true error (i.e. error ratio< 1), only 205* EKF *runs resulted in reduced true error.*

Table 4.2: Maximum and minimum standard deviation ratios

Only results for successful runs (as defined in Equation 4.16) are presented.

	$\max(1+\delta)$	$\min(1+\delta)$	$\text{mean}(1+\delta)$
UKF(1000 runs)	1.73	0.56	1.05
EKF(205 runs)	2.62	0.75	1.46

The standard deviation of the estimate error at the end of a run can be used as an assessment of the best-case and worst-case performance. If a run is successful (i.e. $\sigma_{K,truth} < \sigma_{1,truth}$)

$$\frac{\sigma_{K,truth}}{\sigma_{K,est}} = 1 + \delta \quad \text{where} \quad \delta > -1 \tag{4.17}$$

For a "good" estimator $\delta \approx 0$, indicating that the estimated state uncertainty accurately represents the true state uncertainty. $\delta > 0$ indicates that the estimated state uncertainty underpredicts the true state uncertainty, increasing the likelihood of collisions with obstacles. $\delta < 0$ indicates that the estimated state uncertainty is overpredicted, leading to inefficient trajectories. Note that if the estimate did not converge then δ would continue to grow without bound, and thus would not be a meaningful assessment of performance. In any case, a diverged estimate indicates failure.

Maximum, minimum, and mean values of $(1 + \delta)$ are given in Table 4.2 for successful runs. Figure 4.2 showed that all runs for the UKF-based estimator converged. The largest value of $(1+\delta)$ for the UKF was 1.73, indicating that the end-of-run true standard deviation of the estimate error does not exceed the end-of-run estimated standard deviation of the estimate error by more than

73%. The mean value of $(1+\delta)$ is 1.05, indicating that on average the true error was accurately predicted by the estimated covariance. Conversely, the EKF-based implementation was unsuccessful for 795 runs, indicated by the increase in estimate error. For the remaining 205 successful runs, the worst-case value of $(1+\delta)$ was 2.62, indicating that the true error is 162% greater than the estimated error. On average (for successful runs only) the true error exceeded the estimated error by 46%.

4.1.4 Navigation and Obstacle Avoidance

Section 4.1.3 showed that a UKF-based estimator provides a convergent, consistent estimate of vehicle position, orientation and speed and of obstacle positions. Flight in an obstacle-strewn environment also requires an algorithm for obstacle avoidance and navigation. In this section a Randomized Motion Planner [17] is used: a sequence of random inputs is generated and the cost of each trajectory is computed based on the probability of collision with obstacles (computed from the estimated obstacle positions and the associated covariance) and final distance from the goal.

To illustrate flight in a cluttered environment Figure 4.4 shows a sequence of images of a UAV navigating through a forest to a goal. True obstacle positions are shown as blue dots, true vehicle position is shown as blue ‘wings’. Estimated obstacle positions are shown as red + with associated 3σ error ellipsoid, estimated vehicle position shown as red ‘wings’ with associated 3σ error ellipsoid. The dotted red line shows the planned trajectory, the blue line shows the actual trajectory flown. The planned trajectory only accounts for obstacles that have been “seen” by the camera: unobserved obstacles remain unknown until they enter the field of view.

Early in the flight (upper left image) estimated obstacle positions are highly uncertain, as shown by the large 3σ uncertainty ellipsoids. As the aircraft approaches an obstacle it is localized with greater accuracy, reflecting both the fact that more measurements to that obstacle have been obtained and that the measurement geometry permits more accurate localization at shorter range (the ‘spread’ of the uncertainty in the bearing is smaller at close range). The increase in positioning certainty has the consequence of increased safety during operations close to an obstacle: with greater certainty in obstacle position come greater certainty of that a planned collision-free path is actually collision-free.

4.2 3D Simulations

Results of 2D simulations showed that consistent estimates of vehicle position and landmark positions can be obtained. The focus of this section is on the error growth characteristics of the vehicle position estimate.

Recall from Section 3.4 that bearings only provide information about *relative* position: absolute position measurements are not available. The estimator therefore is effectively computing vehicle odometry using vision and inertial measurements, and growth in estimate error is to be expected.

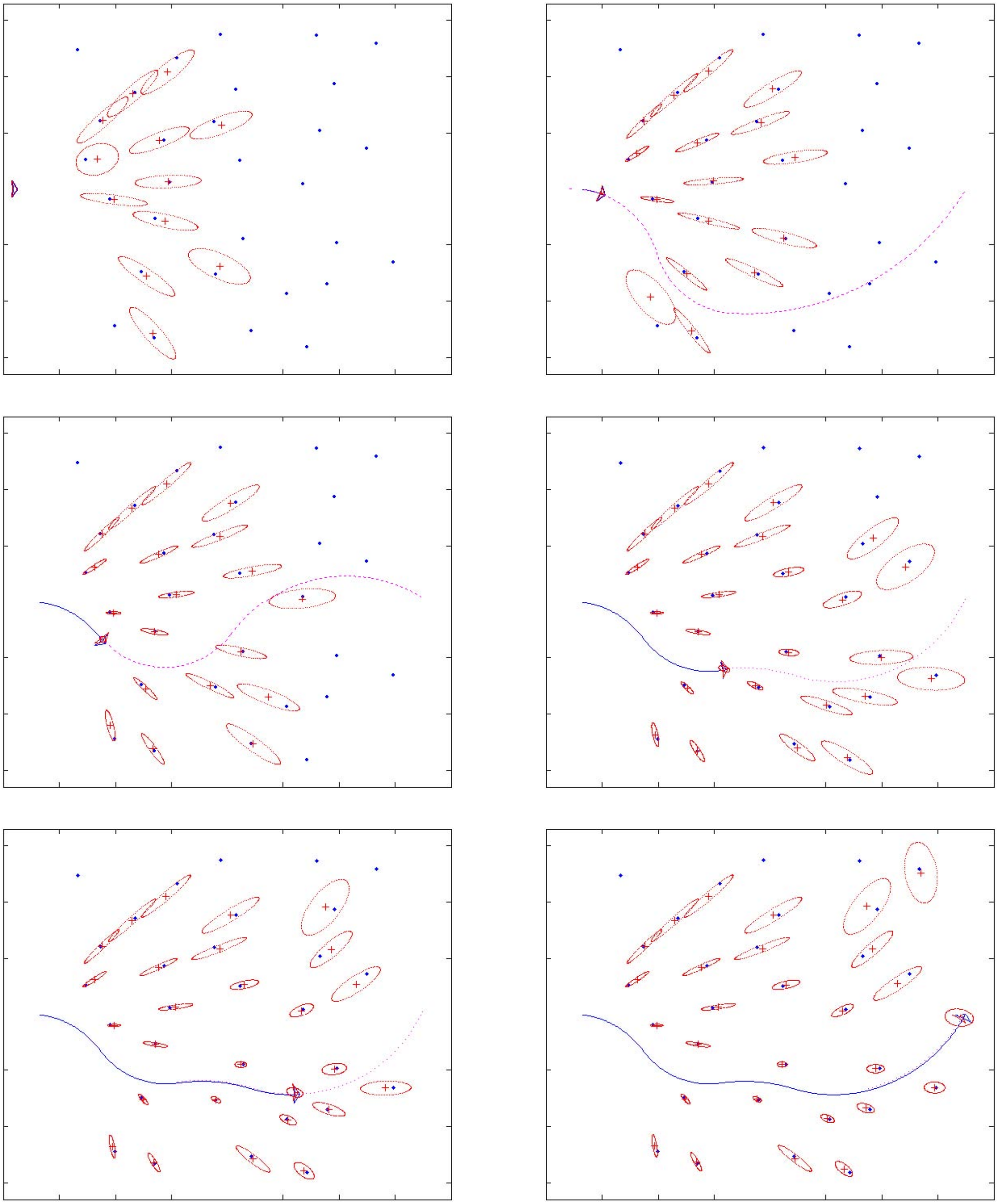

Figure 4.4: Obstacle avoidance and navigation in 2D environment.

The sequence of images shows flight through a 2D forest to a goal position. True obstacle positions are shown as blue dots, true vehicle position is shown as blue 'wings'. Estimated obstacle positions are shown as red + with associated 3σ error ellipsoid, estimated vehicle position shown as red 'wings' with associated 3σ error ellipsoid. The dotted red line shows the planned trajectory, the blue line shows the trajectory flown.

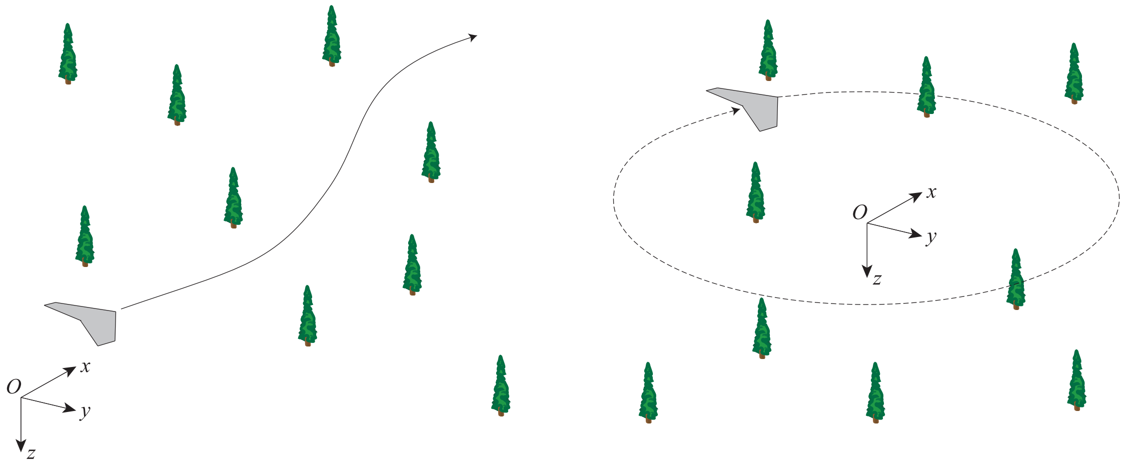

(a) exploration

(b) station keeping

Figure 4.5: Exploration versus station keeping

Exploration (left image) is characterized by flight through unexplored terrain, with new landmarks continually entering and leaving the field of view. Station keeping (right image) is characterized by orbits about a fixed point. Landmarks may cyclically enter and leave the field of view, or, if the camera is pointed inwards, may be in continuous view.

The error in vehicle position estimate can be characterized in several ways, and the choice of characterization is dependent the type of motion undergone by the vehicle (Figure 4.5). In exploratory motion the vehicle traverses through unexplored terrain, with new landmarks entering the field of view as old landmarks leave the field of view. In effect the vehicle navigates using visual odometry, and error is best characterized as a percentage of distance traveled. A second type of flight that may occur is station keeping, where the vehicle follows a roughly circular path orbiting a fixed point. Over several orbits the same landmarks will be seen repeatedly, enabling cyclic reductions in the vehicle position error. Alternatively, if the camera is pointed towards the center of the orbit the same landmarks may remain in view continuously, further reducing position error. In this mode error is best characterized as an absolute error relative to true vehicle position. Note, however, that even when the same features are in constant view the lack of absolute position measurements will lead to cyclically varying errors in absolute vehicle position estimate.

Error growth is affected by many factors: the number of features in view at any given time, the length of time a particular feature remains in view and the video frame rate are all critical parameters. These in turn are affected by feature density, vehicle speed and altitude and camera field of view.

The focus of this section is on error growth characteristics of the vehicle position estimate in both exploratory and station keeping flight. This section examines:

1. The effect of number of landmarks in view on vehicle position estimate error. Here data association and landmark initialization are assumed to be solved.
2. The effect of the both the data association algorithm and the landmark initialization algorithm presented in Sections 3.3 and 3.4, respectively, on the vehicle position estimate.

4.2.1 Estimator Performance

A series of Monte Carlo simulations was conducted for both exploratory and station keeping flight to examine the effect of the number of landmarks in view on the vehicle position estimate. Both data association and landmark initialization were assumed to be known.

Results are presented in Sections 4.2.1 and 4.2.2. A discussion of results is given in Section 4.2.3. Noise and initialization parameters for these simulations are given in Appendix B.

Exploration

The vehicle followed a circular trajectory of radius 40m at an altitude of 5m and a speed of 10m/s for a distance of 200m. Monte Carlo simulations were conducted with varying landmark densities to vary the number of landmarks in view. For each simulation 500 runs were conducted, with a new forest generated for each run. In all cases a minimum tree spacing (dependent on the number of trees) was imposed to minimize “clumping” of landmarks in each forest.

The error in estimated vehicle position is shown in Figure 4.6 for each Monte Carlo simulation. The mean of the position error is shown as a solid line, the median position error is shown as a dashed line, and dotted lines show the 5% and 95% position estimate errors.

All runs showed converged estimates. The mean and median errors are roughly equal and lie midway between the 5% and 95% bounds. As expected, increasing the number of features in view from an average of 1.35 to 7.87 decreases the median estimate error from 0.67% to 0.36% of the distance traveled.

Station keeping

The vehicle followed a circular trajectory of radius 200m at an altitude of 100m and a speed of 20m/s for 240 seconds (performing almost 4 orbits). The camera was pointing towards the center of the orbit, insuring that all features were in continuous view. Seven Monte Carlo simulations were conducted with 1, 2, 3, 5, 7, 9 and 11 landmarks.

As with the exploration case, each Monte Carlo simulation consisted of 500 runs with a new forest generated for each run. Again minimum landmark separations (based on the number of landmarks) were imposed to minimize clumping.

With only one landmark in view the error in vehicle position estimate grew without bound: a single bearing does not provide enough information to localize the vehicle. The error in estimated

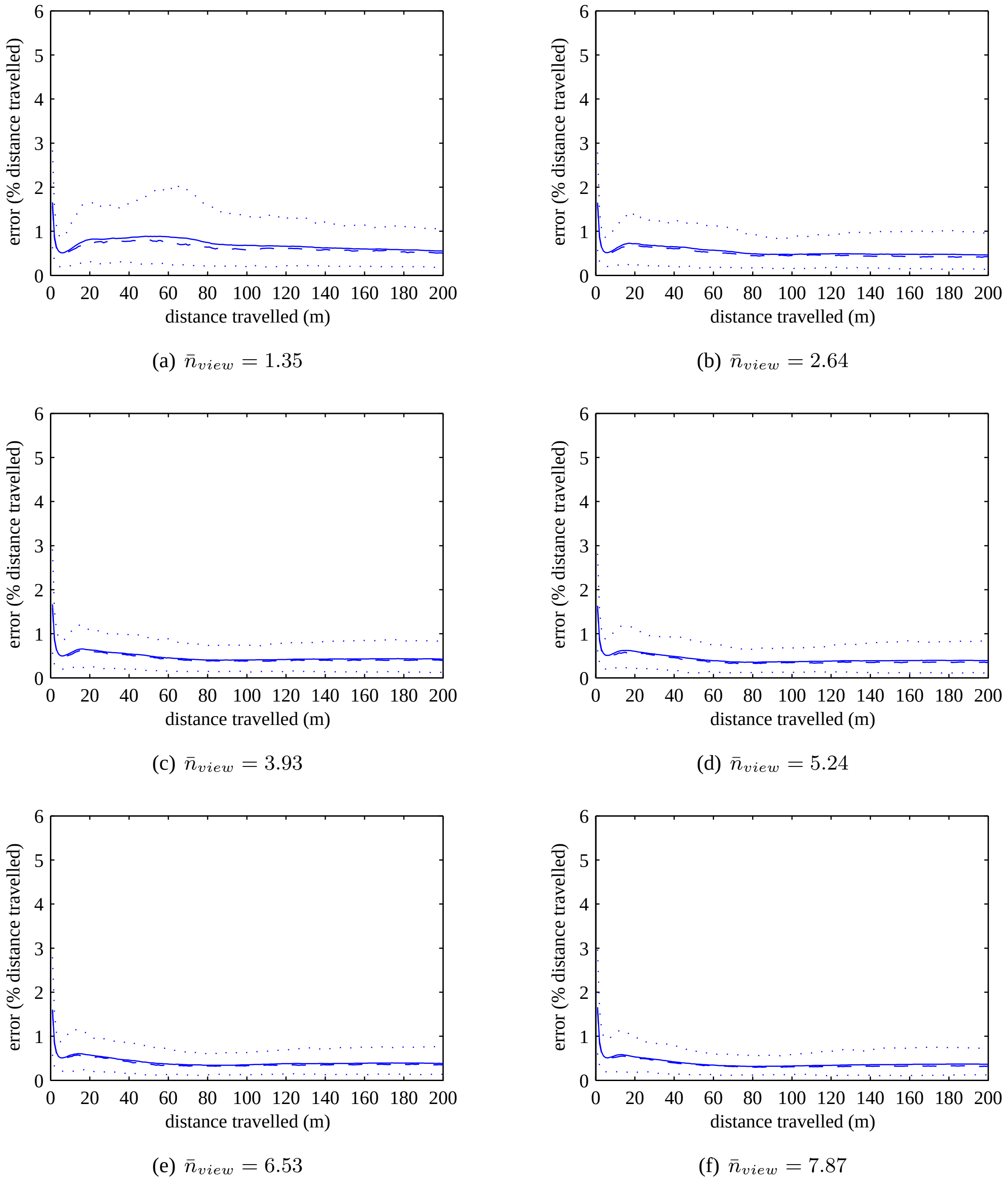

(a) $\bar{n}_{view} = 1.35$

(b) $\bar{n}_{view} = 2.64$

(c) $\bar{n}_{view} = 3.93$

(d) $\bar{n}_{view} = 5.24$

(e) $\bar{n}_{view} = 6.53$

(f) $\bar{n}_{view} = 7.87$

Figure 4.6: Exploration vehicle position estimate error, known data association and landmark initialization.

Mean error shown as solid line, median error shown as dashed line, 5% and 95% bounds shown as dotted lines.

vehicle position is shown in Figure 4.7 for simulations with 2 or more landmarks in view. The mean of the position error is shown as a solid line, the median position error is shown as a dashed line, and dotted lines show the 5% and 95% position estimate errors.

All runs showed converged estimates. The mean and median errors are roughly equal and lie midway between the 5% and 95% bounds. As expected, increasing the number of features in view from 2 to 11 decreases the median estimate error from 1.28m to 0.6m. As expected the estimate error varies cyclically with each orbit.

4.2.2 Effect of Explicit Data Association and Landmark Initialization

A series of Monte Carlo simulations was conducted to assess the effect of explicit data association and landmark initialization on the performance of the estimator. The algorithms of Sections 3.2 and 3.3 were used to compute data association and landmark initialization, respectively.

An error in data association has the potential to lead to estimator divergence. Increasing the number of landmarks in view increases the likelihood of errors in data association. It is therefore expected that divergent estimates will occur as the number of landmarks in view is increased. This will be manifested as an increase in the number and magnitude of outliers in the estimated position error, causing a difference in the median and mean estimate error and potentially causing the 95% bound to increase.

Exploration

As with Section 4.2.1, the vehicle followed a circular trajectory of radius 40m at an altitude of 5m and a speed of 10m/s for a distance of 200m. Monte Carlo simulations were conducted with varying landmark densities to vary the number of landmarks in view. For each simulation 500 runs were conducted, with a new forest generated for each run. In all cases a minimum tree spacing (dependent on the number of trees) was imposed to minimize “clumping” of landmarks in each forest.

The error in estimated vehicle position is shown in Figure 4.8 for each Monte Carlo simulation. The mean of the position error is shown as a solid line, the median position error is shown as a dashed line, and dotted lines show the 5% and 95% position estimate errors.

For small numbers of landmarks in view similar behavior to the known data association and landmark initialization cases were observed, indicating that data association was generally successful. As the average number of landmarks in view increased, however, clear divergence of some runs in each Monte Carlo simulation was observed (indicated by the steadily increasing 95% bound for the cases with $\bar{n}_{view} = 6.56$ and $\bar{n}_{view} = 7.87$).

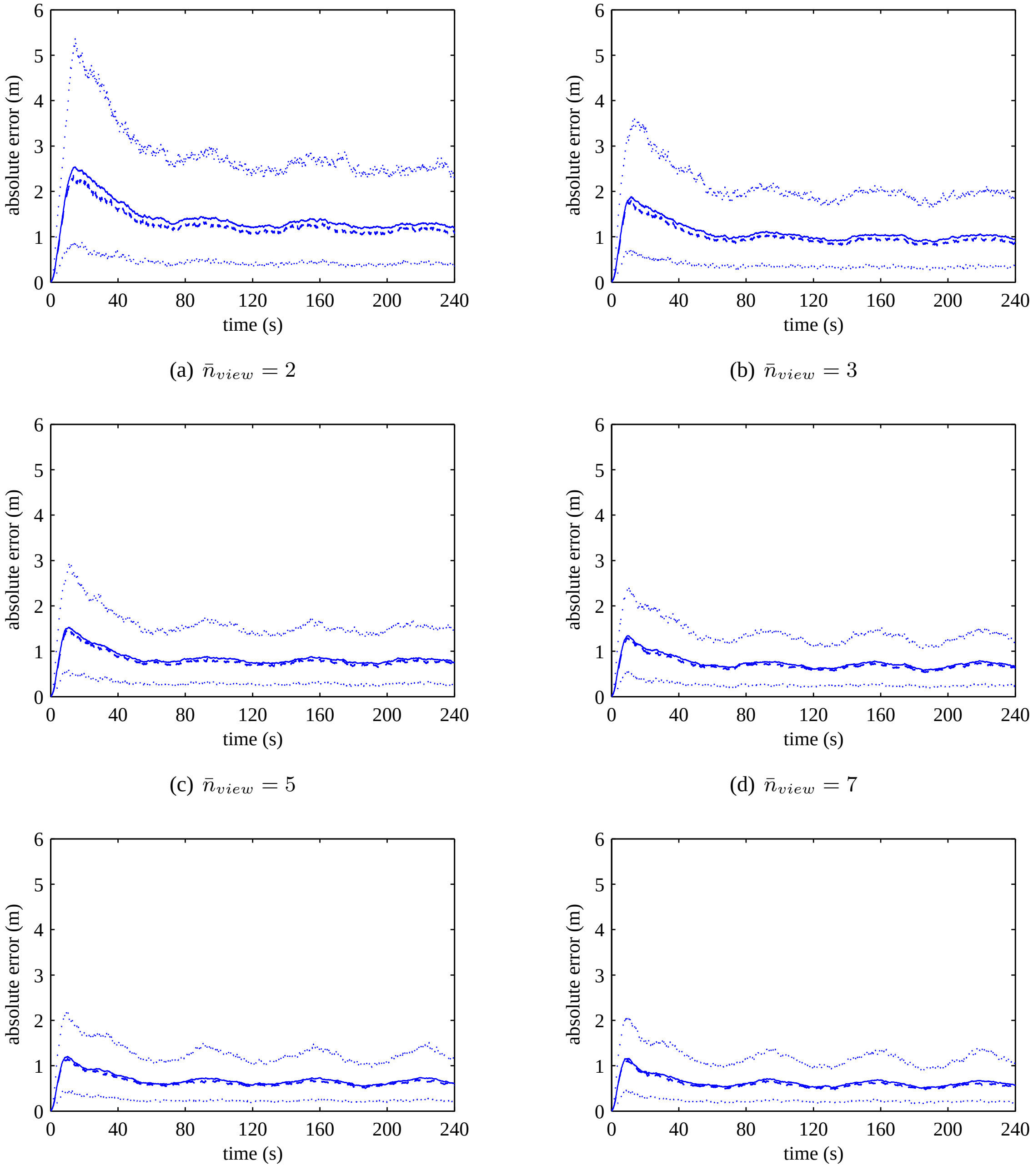

(a) $\bar{n}_{view} = 2$

(b) $\bar{n}_{view} = 3$

(c) $\bar{n}_{view} = 5$

(d) $\bar{n}_{view} = 7$

(e) $\bar{n}_{view} = 9$

(f) $\bar{n}_{view} = 11$

Figure 4.7: Station keeping vehicle position estimate error, known data association and landmark initialization.

Mean error shown as solid line, median error shown as dashed line, 5% and 95% bounds shown as dotted lines.

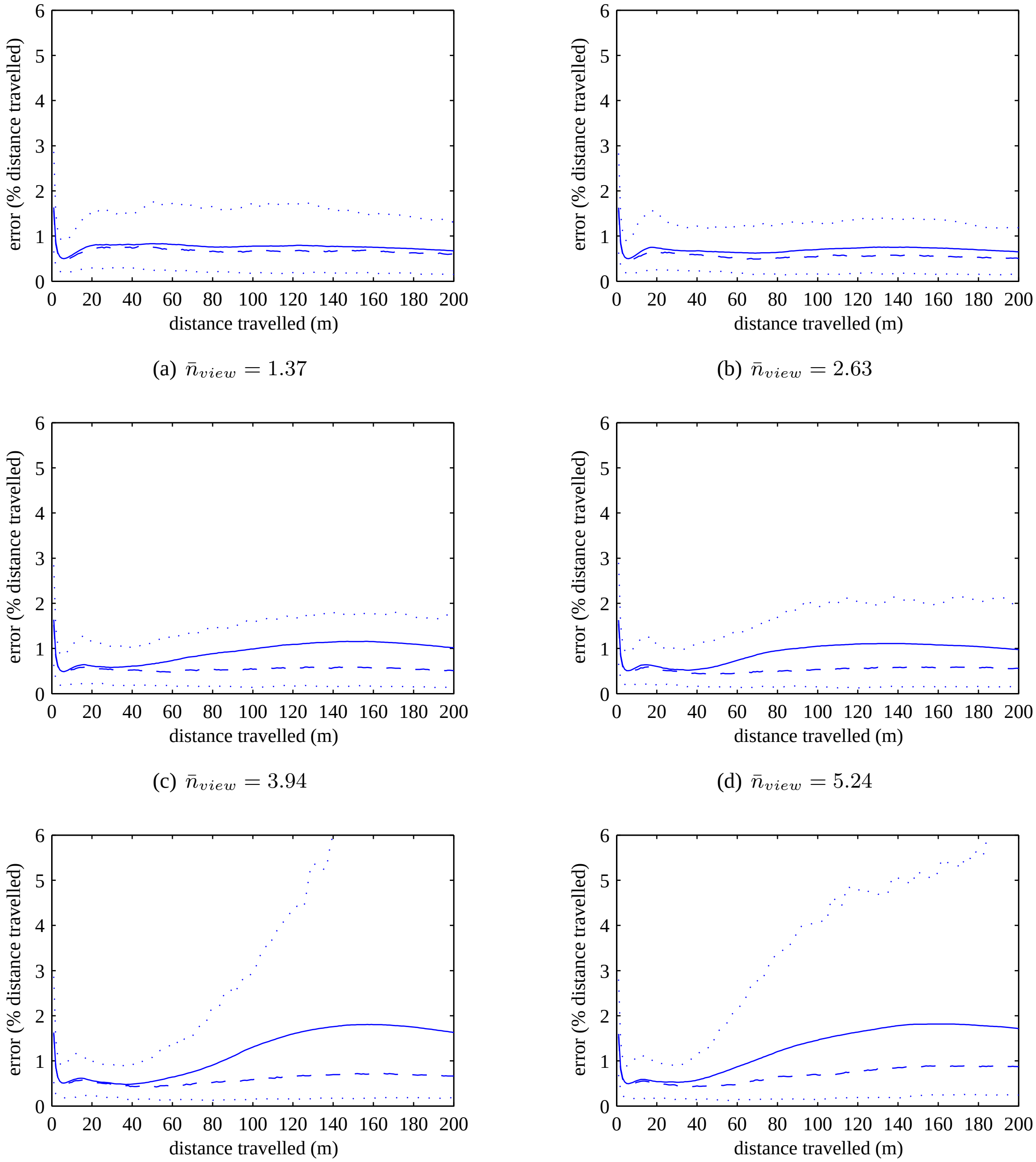

(a) $\bar{n}_{view} = 1.37$

(b) $\bar{n}_{view} = 2.63$

(c) $\bar{n}_{view} = 3.94$

(d) $\bar{n}_{view} = 5.24$

(e) $\bar{n}_{view} = 6.56$

(f) $\bar{n}_{view} = 7.87$

Figure 4.8: Exploration vehicle position estimate error, explicit data association and landmark initialization.

Mean error shown as solid line, median error shown as dashed line, 5% and 95% bounds shown as dotted lines.

Station keeping

As with Section 4.2.1, the vehicle followed a circular trajectory of radius 200m at an altitude of 100m and a speed of 20m/s for 240 seconds (performing almost 4 orbits). The camera was pointing towards the center of the orbit, insuring that all features were in continuous view. Monte Carlo simulations were conducted with 1, 2, 3, 5, 7, 9, and 11 landmarks.

As with the exploration case, each Monte Carlo simulation consisted of 500 runs with a new forest generated for each run. Again minimum landmark separations (based on the number of landmarks) were computed to minimize clumping.

The error in estimated vehicle position is shown in Figure 4.9 for simulations with 2 or more landmarks in view. The mean of the position error is shown as a solid line, the median position error is shown as a dashed line, and dotted lines show the 5% and 95% position estimate errors.

For cases with 5 or fewer landmarks in view similar behavior to the estimator only cases were observed. For $\bar{n}_{view} = 7$ mean error is increasing, indicating that the magnitude of the outliers (but not the number, since both the 95% bound and the median error are still small) is increasing. For $\bar{n}_{view} > 7$ several runs in each Monte Carlo simulation are clearly diverging (note the difference in scale). The median errors, however, are not increasing as significantly, again indicating that the magnitude, but not the number, of outliers in estimated position error is increasing.

4.2.3 Discussion of 3D Simulation Results

Results of the 3D Monte Carlo simulations are summarized in Figure 4.10. Each plot shows the mean and median vehicle position estimate errors for exploration (left image) and station keeping (right image).

The estimator only cases (plotted with $+$) show monotonically decreasing estimate error as the number of landmarks in view increases. Each landmark provides an independent bearing measurement: therefore the estimate error should vary approximately with $\frac{1}{\sqrt{\bar{n}_{view}}}$. To verify this, a least squares fit was conducted for the assumed function

$$e = \frac{a}{\sqrt{\bar{n}_{view} + b}} + c \tag{4.18}$$

where e is the average of the median error of each Monte Carlo simulation. The computed values of the parameters a, b, and c as well as the 2-norm of the residual are given in Table 4.3. The small residual indicates the goodness of the fit: as expected the error in vehicle position estimate varies with $\frac{1}{\sqrt{\bar{n}_{view}}}$.

As expected, results are quite different if data association is not known a priori. When the number of landmarks in view is small similar behavior to the cases with known data association was observed, indicating that the data association algorithm of Section 3.2 was generally successful. For

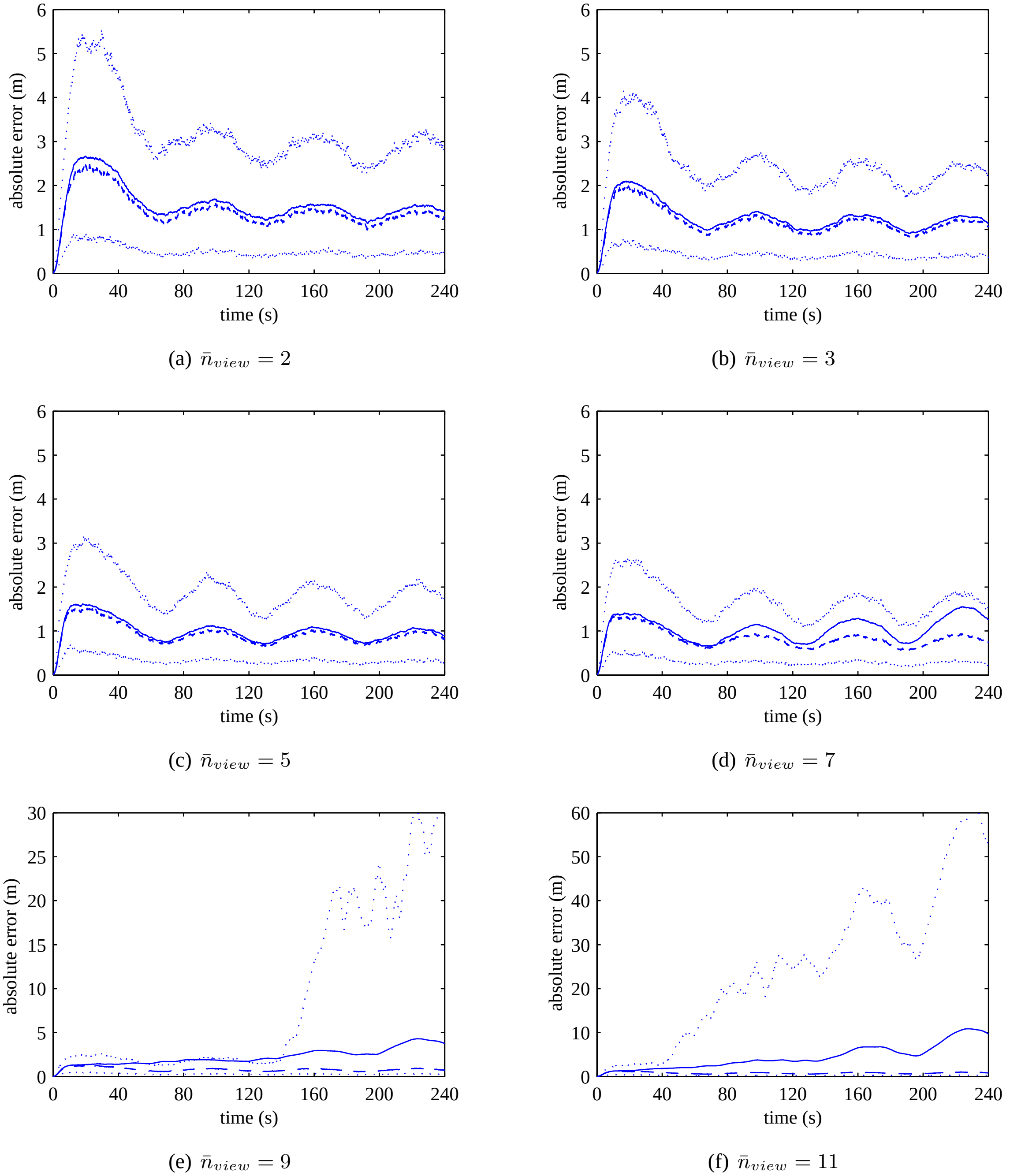

(a) $\bar{n}_{view} = 2$

(b) $\bar{n}_{view} = 3$

(c) $\bar{n}_{view} = 5$

(d) $\bar{n}_{view} = 7$

(e) $\bar{n}_{view} = 9$

(f) $\bar{n}_{view} = 11$

Figure 4.9: Station keeping vehicle position estimate error, explicit data association and landmark initialization.

Mean error shown as solid line, median error shown as dashed line, 5% and 95% bounds shown as dotted lines.

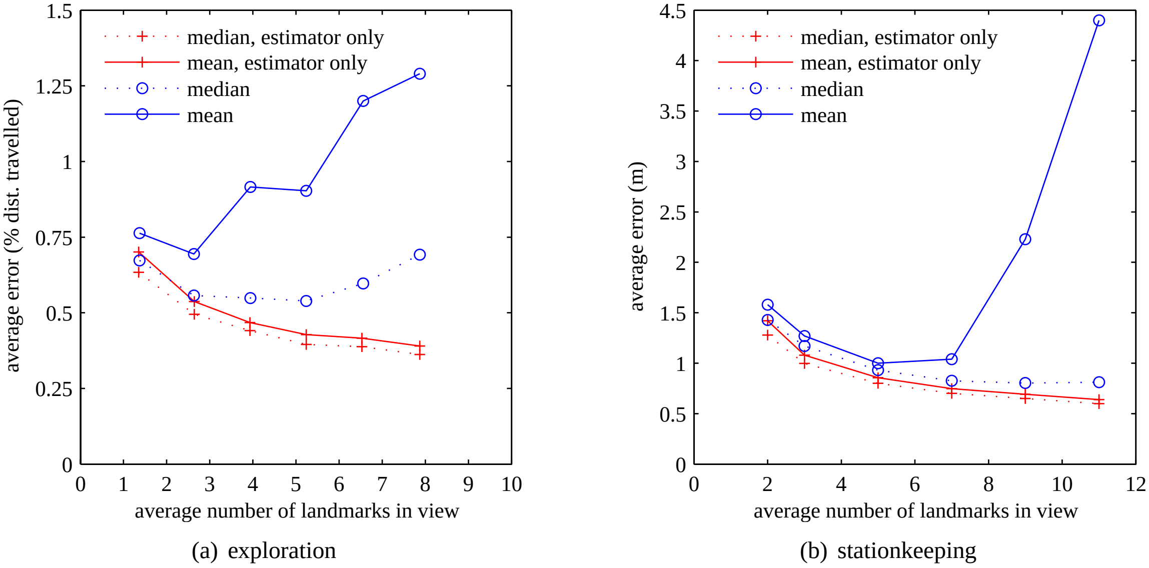

(a) exploration (b) stationkeeping

Figure 4.10: Effect of landmark density on vehicle position estimate error.

For exploration error is plotted as percentage of distance traveled, for station keeping absolute error is plotted.

Table 4.3: Error growth parameters

	a	b	c	$\|r\|_2$
exploration	0.525	-0.0373	0.173	0.013
station keeping	1.12	-0.80	0.25	0.015

larger numbers of landmarks in view errors in data association caused progressively larger errors in position estimate. For the exploration cases the minimum error occurred when the average number of landmarks in view was 2.62, for exploration the minimum error occurred with $\bar{n}_{view} = 5$.

While these results will vary depending on the values of bearing and inertial measurement noise and flight trajectory parameters, they give a clear indication of the number of landmarks that should be actively tracked by the estimator. If data association is not known perfectly, no more than three landmarks should be tracked for exploration and no more than five landmarks should be actively tracked for exploration. Even with perfect data association, a point of diminishing returns in vehicle position estimate error is reached at about 5 landmarks tracked for both exploration and station keeping.

This raises a question of selecting appropriate landmarks when flying through landmark-rich environments. Using all available landmarks is both computationally intense and prone to failure. The problem of selecting an optimal set of landmarks is an interesting one.

Landmarks should be geographically diverse: a landmark on a bearing similar to another will not provide much additional information. In addition, landmarks should be chosen to ensure that bearings change significantly over time, since it is the change in bearing that provides the information necessary to localize the vehicle and the landmark.

4.3 Summary

This chapter has presented results of simulations of UAV flight in unexplored environments.

2D Simulation

- **Estimate consistency:** The UKF-based estimator developed in Chapter 3 provides consistent estimates of vehicle state and obstacle positions.

- **Obstacle avoidance:** Using estimates of system state and the estimated covariance a trajectory planner can compute a safe path through a cluttered environment.

3D Simulation

Two classes of flight were investigated with Monte Carlo simulations: exploration, where new landmarks continually come into view; and station keeping, where the vehicle orbits a fixed point.

- **Vehicle position estimate error:** With known data association the vehicle position estimate varies inversely with the square root of the number of landmarks.

- **Data association and landmark initialization:** As expected, errors in data association generally lead to divergent estimates. Correct data association is therefore critical to successful state estimation. Increasing the number of landmarks in view increases the likelihood of errors in data association. Therefore there exists a number of landmarks in view which minimizes the vehicle position estimate error. For the simulations done here, approximately 3 landmarks in view minimizes vehicle estimated position error for exploration flight and 5 landmarks in view minimizes vehicle estimated position error for station keeping flight.

- **Landmark selection** Even when data association is known perfectly a point of diminishing returns in vehicle position estimate error is quickly reached as the number of landmarks in view is increased. This suggests that the number of actively tracked landmarks in SLAM applications should be limited. The actual number will be implementation dependent, but will have the additional benefit of reducing the computational overhead associated with SLAM.

Chapter 5

Ground Vehicle Results

THE ESTIMATOR DEVELOPED in Chapter 3 and tested in simulation for UAV applications is now applied to the problem of navigating a small Unmanned Ground Vehicle (UGV). Since a kinematic model driven by inertial measurements is used for the prediction step both the algorithms developed earlier and the necessary hardware can in principle be simply “bolted on” to a vehicle and used for obstacle avoidance and navigation. Both hardware and simulation tests are discussed.

The hardware tests demonstrate successful state estimation using the algorithms presented earlier on an operational system. Real time execution is demonstrated in addition to the ability of the algorithms to cope with real sensor measurements and model and calibration errors. Furthermore, the hardware tests provide another example of integration of the estimation algorithm with an obstacle avoidance and navigation algorithm, enabling real-time navigation through a cluttered environment.

The tests presented in this chapter were conducted using a small UGV. Although a ground vehicle nominally has only three degrees of freedom (x and y position and heading), vehicle state estimation was performed for the six degrees of freedom inherent to a UAV (x and y position, altitude z, and Euler angles ϕ, θ, ψ). The hardware tests examined three subjects: (a) accuracy of the estimation of states required for aircraft control (i.e. altitude, roll and pitch); (b) estimation of relative obstacle position; (c) mapping and absolute vehicle localization. Absolute truth data was available for obstacle positions, vehicle start position and final vehicle position (obtained using a tape measure). Since it was a ground vehicle, approximate truth data was available for vehicle altitude, roll and pitch throughout the run.

Results showed that altitude, roll and pitch were estimated accurately (altitude error was generally within the estimated 3σ bound) and the obstacle relative position estimates were accurate within estimated error. As expected, drift was observed in the absolute vehicle localization and landmark mapping. However, the drift was larger than the estimated covariance and was similar in both magnitude and direction for each of the three runs, indicating systemic bias.

Two possible causes for the drift are unmodeled offset in camera orientation and poor initial estimates of accelerometer bias (i.e. initial estimate error significantly greater than the assumed error). Simulations showed that an unmodeled camera pitch offset of $1°$ results in absolute position estimate errors similar in magnitude and direction to those observed in hardware tests. A vehicle pitch of $3°$ during IMU initialization would also give absolute position errors similar to those observed in hardware tests due to the projection of gravity onto the computed initial accelerometer biases.

When additional state information is available (e.g. because the vehicle travels to a known goal location) drift in vehicle localization and the map can be corrected (Section 3.4). In SLAM implementations the uncertainty in vehicle position and landmark positions becomes fully correlated over the course of vehicle motion. Additional knowledge about one of the states (e.g. vehicle position) can therefore be used to correct the estimates of all states. Additional knowledge of vehicle position may be obtained by revisiting previously explored areas (loop closure) or by sporadic GPS updates. The correction step requires the full covariance matrix, which was not available in the hardware tests. Simulation results are used to illustrate map correction.

Section 5.1 describes the hardware implementation and Section 5.2 describes the test setup. Section 5.3 describes results of vehicle state estimation, Section 5.4 describes results of obstacle relative position estimation and Section 5.5 presents results of vehicle absolute position estimation and mapping. Results are summarized in Section 5.6.

5.1 Hardware Implementation

The ground vehicle “Squirrel” (Figure 5.1) is based on an electric RC truck platform. It carries an inertial measurement unit, radio modem, camera and analog video transmitter.

Data from the camera and IMU are transmitted to a ground station via wireless links, where all computation is performed. Commands are subsequently sent to the vehicle through a modified RC transmitter. The ground station consists of a 3.0GHz Xeon dual-processor desktop computer, a Matrox Meteor II frame grabber, a 2.4GHz receiver for analog video, a Maxstream 900MHz radio modem and a modified 72MHz RC transmitter.

The navigation system can be loosely divided into four subsystems: a vision subsystem, which provides bearings to landmarks in the environment; an inertial subsystem, which provides accelerations and angular rates; the estimator; and a path planning and control subsystem (see Figure 5.2).

5.1.1 Vision Subsystem

The camera is a Panasonic KX-131 CCD camera equipped with a $115°$ field of view lens. Resolution is 380 lines by 640 pixels per line. This is converted to NTSC before analog transmission over a

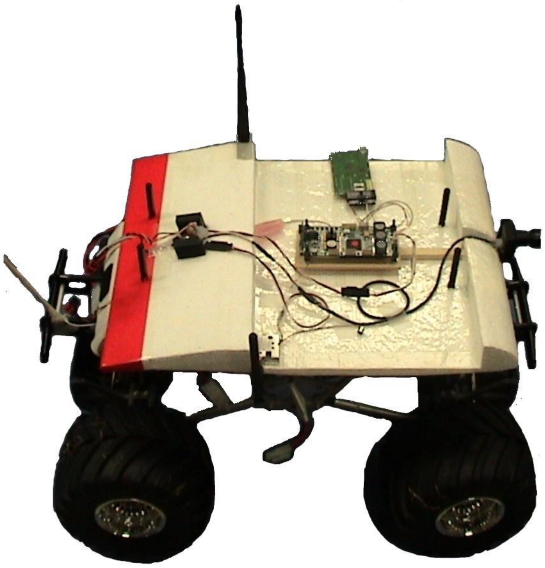

Figure 5.1: The autonomous ground vehicle *Squirrel* used as testbed.

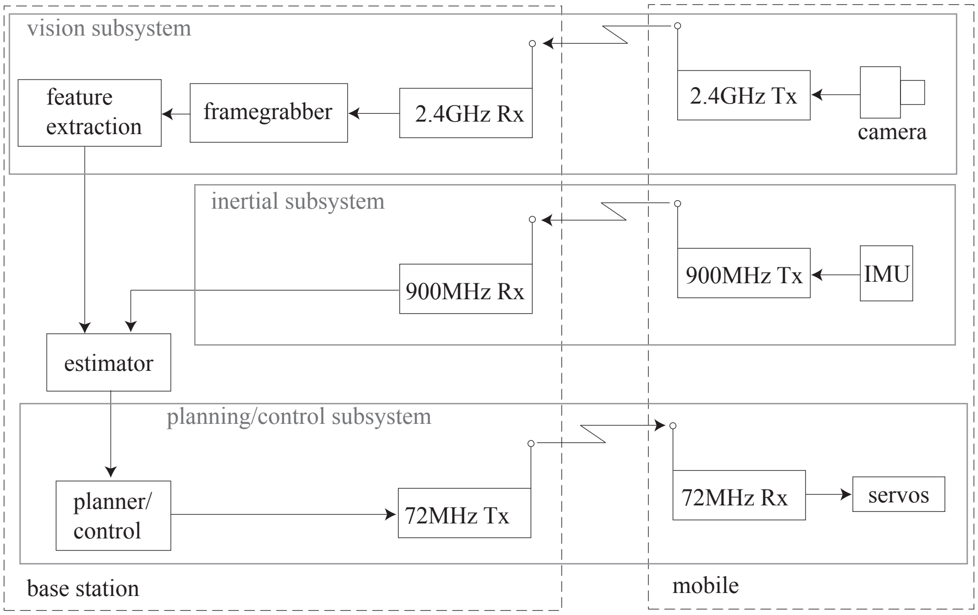

Figure 5.2: Schematic of mapping/navigation system.

Data is collected and transmitted to the ground station using a 2.4GHz analog transmitter for the video and 900MHz radio modem for inertial measurements. Control commands are sent to the vehicle via a modified 72MHz RC transmitter.

Table 5.1: Typical 1σ measurement noise for IMU portion of Phoenix-AX autopilot module.

acceleration (m/s^2)			angular rate (rad/s)		
x	y	z	x	y	z
0.085	0.080	0.062	0.0084	0.0098	0.0078

2.4GHz wireless link to the groundstation. A Matrox Meteor II framegrabber captures frames at 10Hz.

Each frame is blurred using a 5 pixel×5 pixel Gaussian filter and downsampled to 320×240 pixels. The downsampled image is further blurred with a 5 pixel×5 pixel flat filter prior to segmentation. Color segmentation is done in the HSV color space (Hue, Saturation, Value) to recognize red blobs, which have been defined as landmarks/obstacles. Blobs smaller than 15 pixels square are ignored to reduce the effect of noise and spurious feature detection. Blobs which touch the edge of the frame are also ignored. A standard lens distortion correction algorithm [6] is applied to the xy pixel location of the centroid of each blob.

The wireless link is subject to dropouts caused by interference, multipath and occlusion, hence the estimator must be robust to data losses in the vision subsystem.

5.1.2 Inertial Subsystem

The inertial measurement unit is part of the Phoenix-AX Autopilot Module [40] supplied by O-Navi LLC [39]. In this application accelerations and angular rates (along with a packet checksum) are transmitted over an RS-232 link using a 900MHz radio modem to a ground station at a rate of approximately 100Hz. At the ground station this is downsampled to 50Hz by averaging. This reduces the effect of a lost packet.

Noise levels and starting values for biases are obtained prior to each run by keeping the unit approximately level and stationary for a period of time. The mean and standard deviation of the signals provide bias and noise, respectively. Typical noise levels are given in Table 5.1.

5.1.3 Path Planning and Control

Planning and control are not the focus of this dissertation. However, to demonstrate vehicle navigation in a cluttered environment an algorithm for path planning and vehicle control is necessary. Due to its ease of implementation a potential field approach was used for obstacle avoidance and navigation to the goal. A cost function dependent on the distance from the goal and distance from obstacles is computed:

$$c = (\mathbf{x}_g - \hat{\mathbf{x}})^T \mathbf{W}_g (\mathbf{x}_g - \hat{\mathbf{x}}) + \sum_{i=1}^{N} \left[(\hat{\mathbf{x}}_i - \hat{\mathbf{x}})^T \mathbf{P}_{ii}^{-1} (\hat{\mathbf{x}}_i - \hat{\mathbf{x}}) + (\hat{\mathbf{x}}_i - \hat{\mathbf{x}})^T (\hat{\mathbf{x}}_i - \hat{\mathbf{x}}) \right] \tag{5.1}$$

Here $\mathbf{x}_g$ is the goal location in absolute coordinates, $\hat{\mathbf{x}}$ is the current estimate of absolute vehicle position and $\mathbf{W}_g$ is a weighting matrix. Both the Mahalanobis distance and the Euclidean distance from obstacles is used for collision avoidance. $\hat{\mathbf{x}}_i$ is the estimated obstacle position, $\mathbf{P}_{ii}$ is the uncertainty in estimated position. The Mahalanobis distance essentially computes the distance between the vehicle and an obstacle as a number of standard deviations: the inverse of the Mahalanobis distance is a measure of the likelihood of collision. The Euclidean distance is included to insure that separation is maintained even when the uncertainty in obstacle estimated position is small.

The vehicle steering angle is computed based on the cross product of the estimated vehicle velocity (in absolute coordinates) and the gradient of the cost function:

$$\gamma = K \arcsin\left(\frac{\hat{\mathbf{v}}_g \times \nabla c}{|\hat{\mathbf{v}}_g||\nabla c|}\right) \tag{5.2}$$

Here $\hat{\mathbf{v}}_g$ is the estimated vehicle velocity expressed in the inertial frame and K is a gain.

Potential field algorithms are subject to local minima and generally require tuning of parameters to be effective. For the hardware tests described in this chapter no significant tuning was performed.

5.2 Test Description

Figure 5.3 shows the artificial "forest" used for testing. A "tree" consisted of a 2.1m tall pole topped with an red inverted cone. The red cone provided the visual target for landmark identification and the 2.1m height defined the "ground plane" for feature initialization (see Section 3.4). Thirteen trees were placed randomly over an area of approximately 25m×6m. A set of three pylons were placed to define a common coordinate frame and a goal location was defined in relation to the coordinate frame.

At the start of each run the vehicle was placed at (-3,1) in the coordinate frame defined by the three pylons. No attempt was made to level the vehicle. Each run began with the vehicle remaining stationary for 10 seconds while inertial measurements (acceleration and angular rates in three axes) were collected. The average value of acceleration and angular rate in each axis over 10 seconds was computed as an initial estimate of bias, the standard deviation was used for measurement noise. After IMU initialization was completed the vehicle was commanded to drive to the goal location at approximately (22,1.8). Three runs were conducted to investigate: the quality of state estimates that are required for control of a UAV (altitude, roll, pitch); obstacle relative position estimation; absolute vehicle position estimation and mapping.

Because of test limitations truth data was only available for obstacle absolute position (obtained with a tape measure) and vehicle position at the end of the run (obtained with a tape measure). Approximate truth was available for vehicle altitude, roll and pitch angle. True vehicle altitude can be approximated quite well as zero, true vehicle orientation was within a few degrees of zero. While

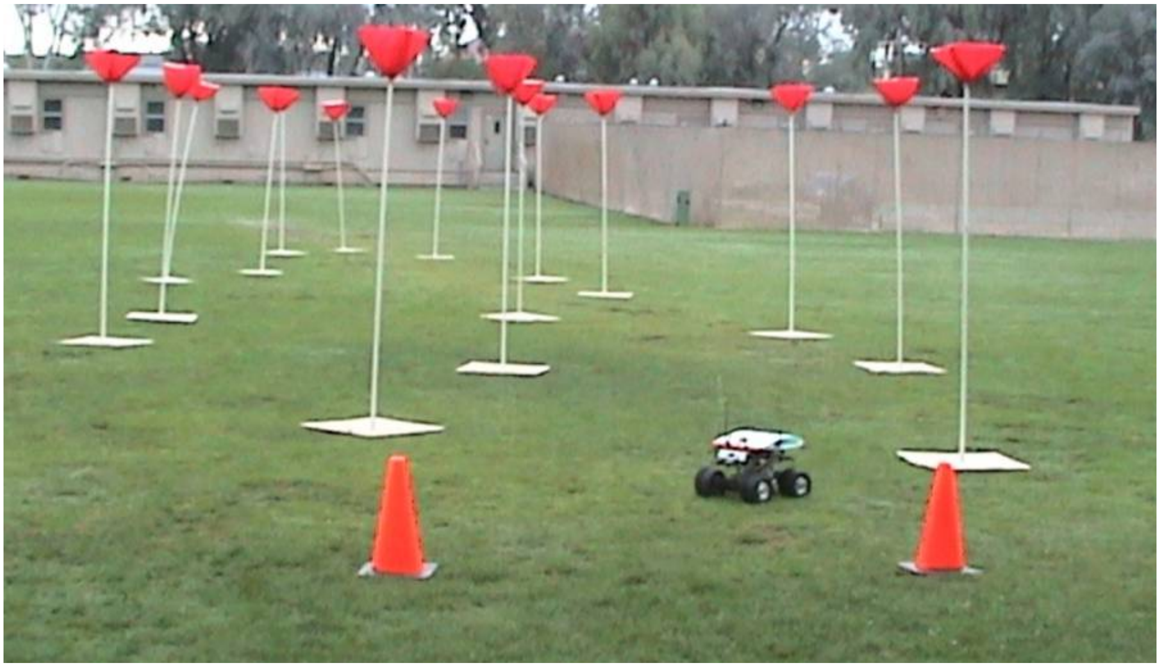

Figure 5.3: The artificial “forest” used for hardware tests.

the vehicle body was nominally flat, a slight roll to the right (positive roll) and pitch up (positive pitch) was observed while the vehicle was in forward motion. This was due to drive train torque. In addition, testing was conducted outdoors on a sports field, which was quite bumpy on the scale of the vehicle. The bumps did not significantly affect altitude but did have a noticeable effect on pitch and roll.

5.3 Vehicle State Estimation

Figures 5.4–5.6 show the number of landmarks in view, altitude estimate error, estimated roll and estimated pitch for the three runs. In each of the runs, on average approximately three landmarks were in view at any time, from a minimum of one to a maximum of six (the brief spike to nine at 37s in run 3 is due to a frame error in the vision system).

The error in estimated altitude ($z - \hat{z}$, where $z = 0$) remains generally within the estimated 3σ bounds for each of the runs. The estimated standard deviation of the altitude estimate error is less than 0.1m for each of the three runs.

Simulation results presented in Chapter 4 showed that the error in position estimate varies inversely with the square root of the number of features in view. This dependence of estimated covariance on number of features in view is also seen in hardware tests: comparing σ_z with the number

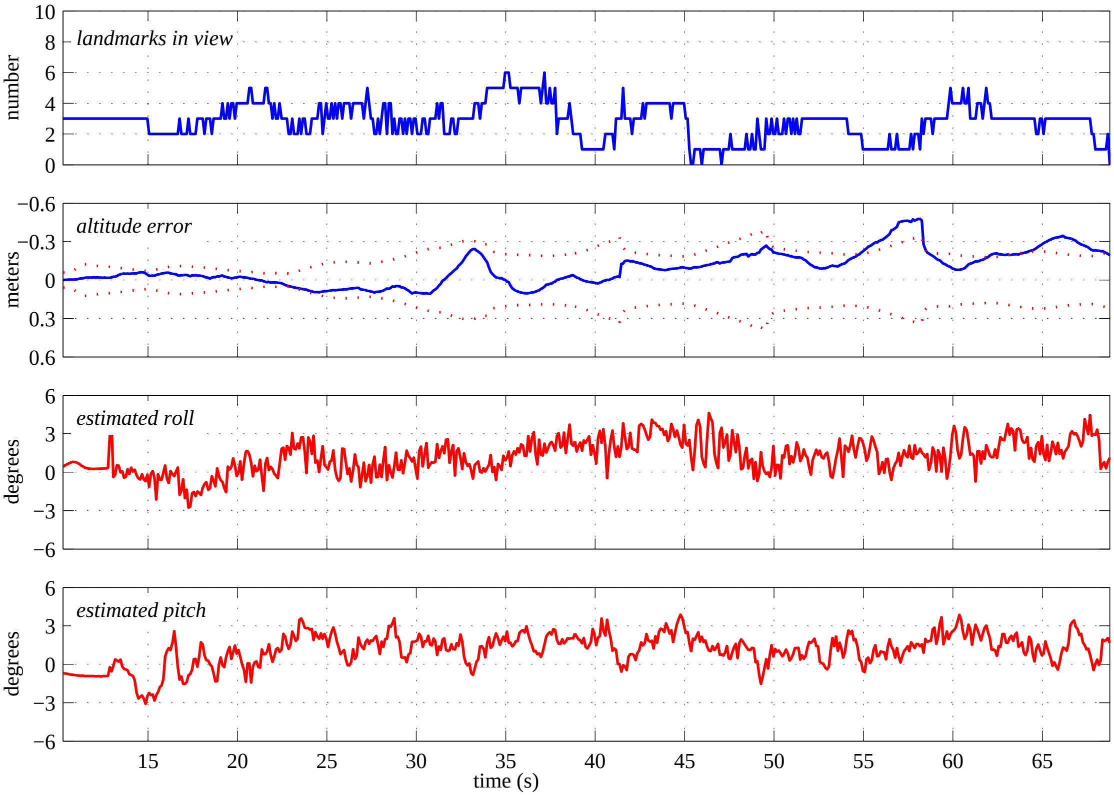

Figure 5.4: Estimated vehicle states, run 1.

The upper plot shows the number of landmarks in view, the second plot shows the error in altitude estimate (blue) along with 3σ bounds (dashed red). The third and fourth plots show estimated roll and pitch, respectively.

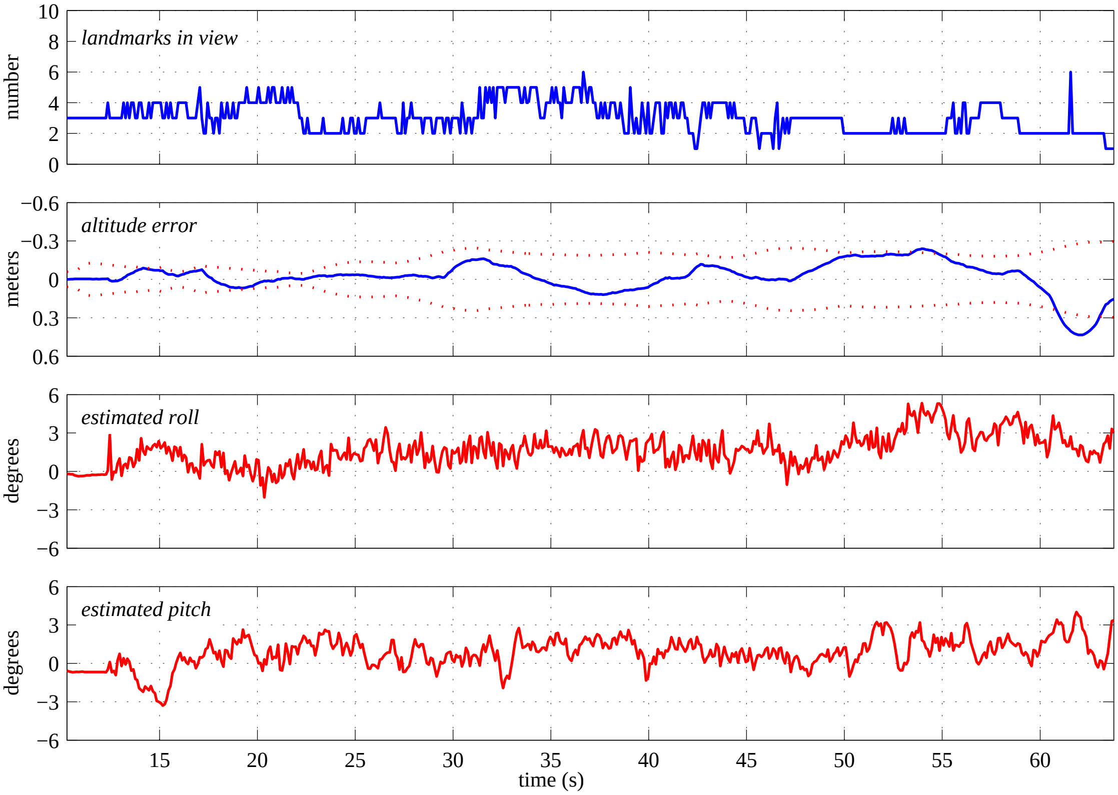

Figure 5.5: Estimated vehicle states, run 2.

The upper plot shows the number of landmarks in view, the second plot shows the error in altitude estimate (blue) along with 3σ *bounds (dashed red). The third and fourth plots show estimated roll and pitch, respectively.*

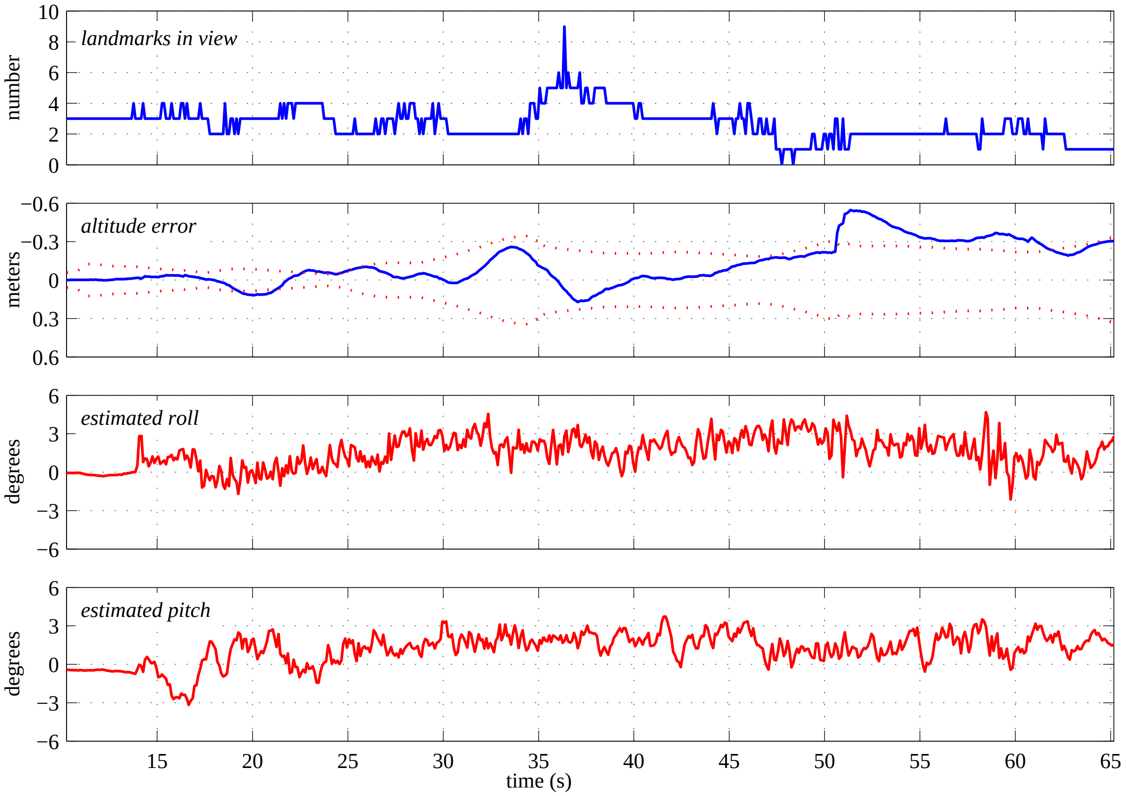

Figure 5.6: Estimated vehicle states, run 3.

The upper plot shows the number of landmarks in view, the second plot shows the error in altitude estimate (blue) along with 3σ bounds (dashed red). The third and fourth plots show estimated roll and pitch, respectively.

Table 5.2: Results of vehicle state estimation

run	$\bar{n}_{view}$	$\overline{\lVert z - \hat{z} \rVert}$	$\bar{\sigma}_z$	$\bar{\sigma}_\phi$	$\bar{\sigma}_\theta$
		m	m	deg.	deg.
1	2.83	0.12	0.063	0.28	0.24
2	3.03	0.083	0.058	0.29	0.24
3	2.66	0.15	0.063	0.29	0.24

of landmarks in view (n_{view}) shows that a decrease in n_{view} leads to an increase in σ_z. Conversely increasing n_{view} leads to a decrease in σ_z.

The number of landmarks in view is generally very ‘noisy’, jumping rapidly as landmarks on the edge of the detection envelope enter and leave.

There is a sharp spike in estimated roll as the vehicle starts moving (at approximately 12s in each run). The vehicle body did in fact roll sharply to the right (positive roll) at the beginning of motion due to drive train torque. After the initial spike a slight positive roll remained throughout the run, caused by drive train torque. This can be seen in the estimated roll. The estimated roll angle is very jagged. This may be partially due to noise in the estimate, but the ground was very bumpy, leading to significant bumps and jogs in the body orientation throughout each run.

Similar behavior can be seen in the pitch estimate. Again a slight positive pitch was observed in the vehicle body while it was underway.

Results are tabulated in Table 5.2.

5.4 Obstacle relative position estimation

Relative obstacle position estimation is critical for obstacle avoidance. To illustrate the accuracy of relative position estimation, Figures 5.7–5.9 show

$$\begin{bmatrix} x_i \\ y_i \end{bmatrix} - \begin{bmatrix} \hat{x}_i - \hat{x} \\ \hat{y}_i - \hat{y} \end{bmatrix} \tag{5.3}$$

for obstacles in the vicinity of the vehicle. Here $[x_i \; y_i]^T$ is the true position of the i^{th} obstacle, $[\hat{x}_i \; \hat{y}_i]^T$ is the estimated position of the i^{th} obstacle and $[\hat{x} \; \hat{y}]^T$ is the estimated vehicle position. In other words, the plots show the estimated relative vehicle position with respect to the true obstacle positions. Blue dots show absolute obstacle positions, the open blue circle shows true final vehicle position. The red $+$ with associated 3σ error ellipsoid shows estimated relative position of the vehicle with respect to an obstacle, where the dotted red line and circle show which obstacle is associated with a particular relative position estimate. Accurate relative position estimates are shown when the estimates of relative vehicle position with respect to each obstacle agree within estimated covariance (i.e. when the error ellipsoids overlap).

For each of the three runs the ellipsoids representing 3σ uncertainty in the relative position estimates generally lie on top of one another, indicating that relative position estimation is accurate within estimated error.

5.5 Mapping

Recall from Chapters 3 and 4 that the lack of absolute position measurements inevitably leads to drift in the absolute vehicle and landmark position estimates. If there are no unmodeled dynamics or biases in the system (e.g. an unmodeled offset in camera orientation) the drift can be characterized as a random walk and will be described by the estimated error covariance. If there are unmodeled biases they will be reflected by a bias in the vehicle position and obstacle position estimates.

Figures 5.10–5.12 show absolute vehicle position estimates and absolute landmark position estimates as a sequence of images over the course of each run. Blue dots show absolute obstacle positions. The open blue circle shows true final vehicle position. The red $+$ with associated 3σ error ellipsoid shows estimated obstacle position, estimated vehicle position is shown by the red “wings” and associated 3σ error ellipsoid. The estimated vehicle path is shown by the red line.

Early in each run absolute obstacle position estimates are quite good, but a bias builds up in all obstacle position estimates as the run progresses. This error is also seen in the final vehicle position estimate, which is offset from the true final vehicle position. The offset is of similar magnitude and direction in all three runs, indicating that a systemic bias is likely.

Effects of some possible error sources

There are many possible sources of systemic bias. Two are an unmodeled offset in camera orientation and a poor initial estimate of bias. Intuitively, an offset in camera orientation should result in a biased map because the camera provides information about the surrounding landmarks. Similarly, a poor estimate of accelerometer bias will result in an error in the estimate of the baseline between successive camera images, leading to an error in both landmark relative position estimates and vehicle position estimates.

To illustrate the effect of these possible error sources simulations of the outdoor tests with unmodeled errors are presented.

Figure 5.13 shows the effect of an unmodeled 1° offset in camera pitch. This offset in camera orientation causes errors in two ways: first, by introducing a bias in the initial landmark position, and second by introducing a bias in the vehicle position correction.

The map generated with camera pitch offset shows similar behavior as observed in the hardware tests: initial map accuracy is good, but the vehicle position estimate and mapped landmark positions

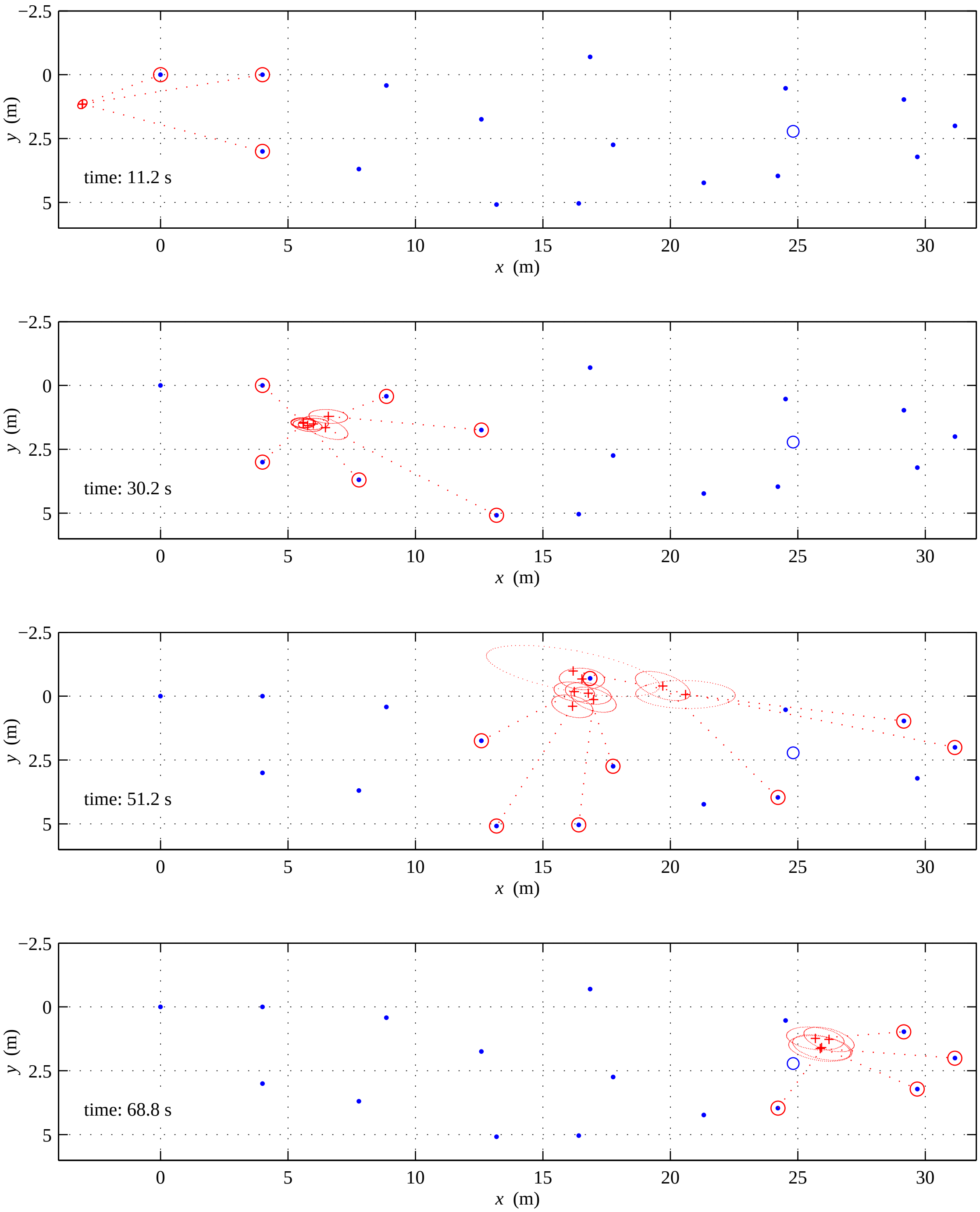

Figure 5.7: Sequence of relative position estimates, run 1

Blue dots show absolute obstacle positions. The open blue circle shows true final vehicle position. The red $+$ with associated 3σ error ellipsoid shows estimated relative position of the vehicle with respect to an obstacle, where the dotted red line and circle show which obstacle is associated with a particular relative position estimate.

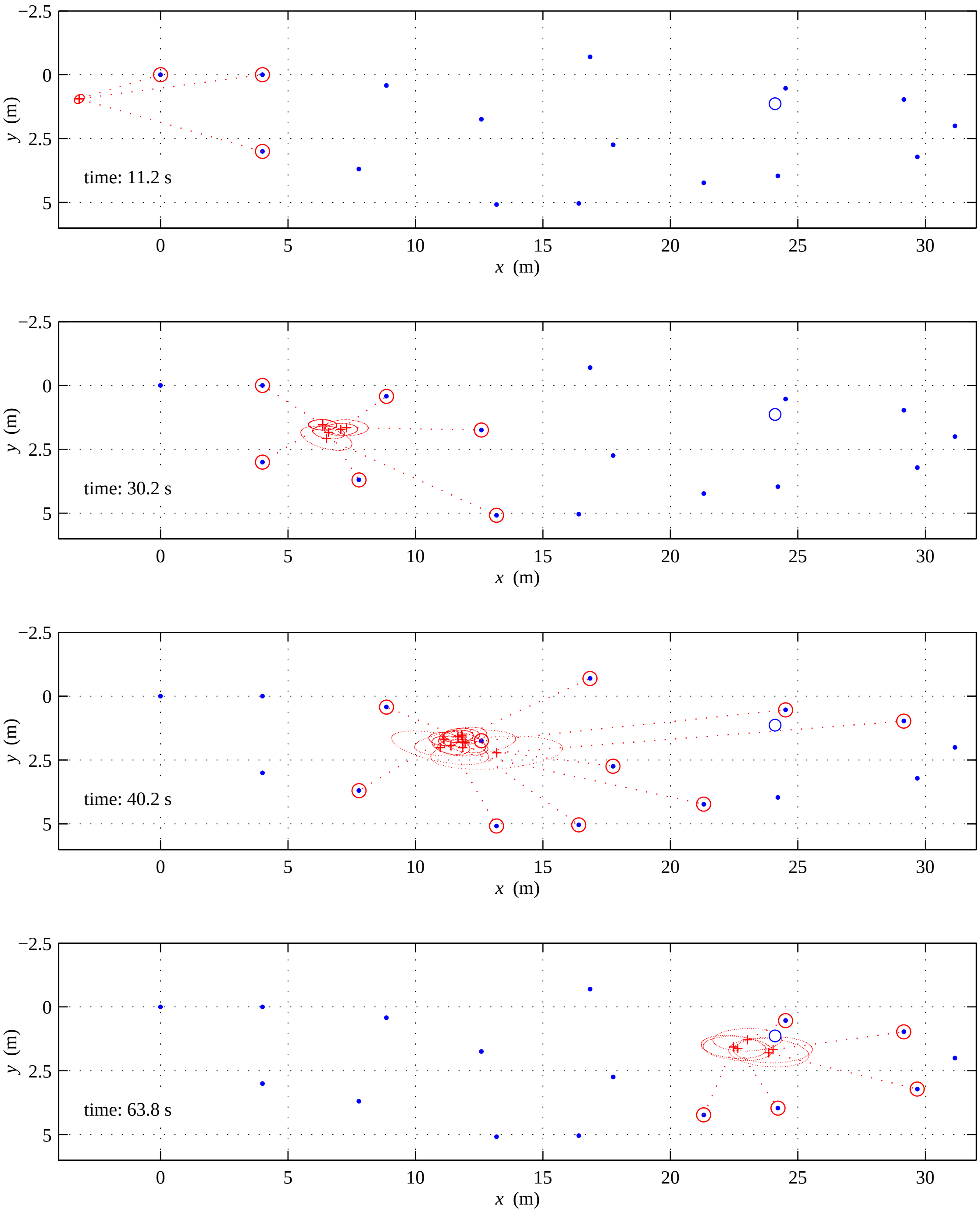

Figure 5.8: Sequence of relative position estimates, run 2

Blue dots show absolute obstacle positions. The open blue circle shows true final vehicle position. The red + with associated 3σ error ellipsoid shows estimated relative position of the vehicle with respect to an obstacle, where the dotted red line and circle show which obstacle is associated with a particular relative position estimate.

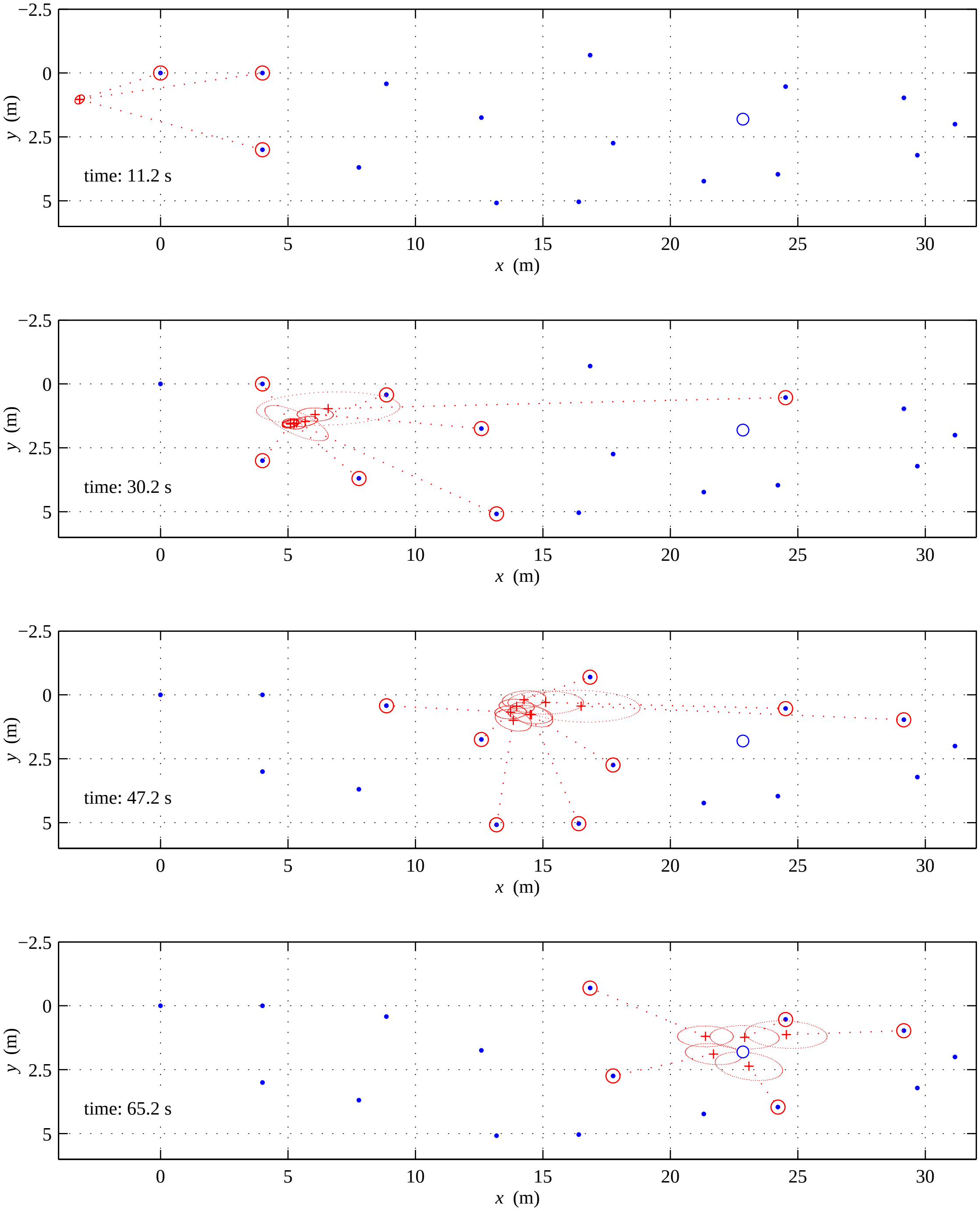

Figure 5.9: Sequence of relative position estimates, run 3

Blue dots show absolute obstacle positions. The open blue circle shows true final vehicle position. The red + with associated 3σ error ellipsoid shows estimated relative position of the vehicle with respect to an obstacle, where the dotted red line and circle show which obstacle is associated with a particular relative position estimate.

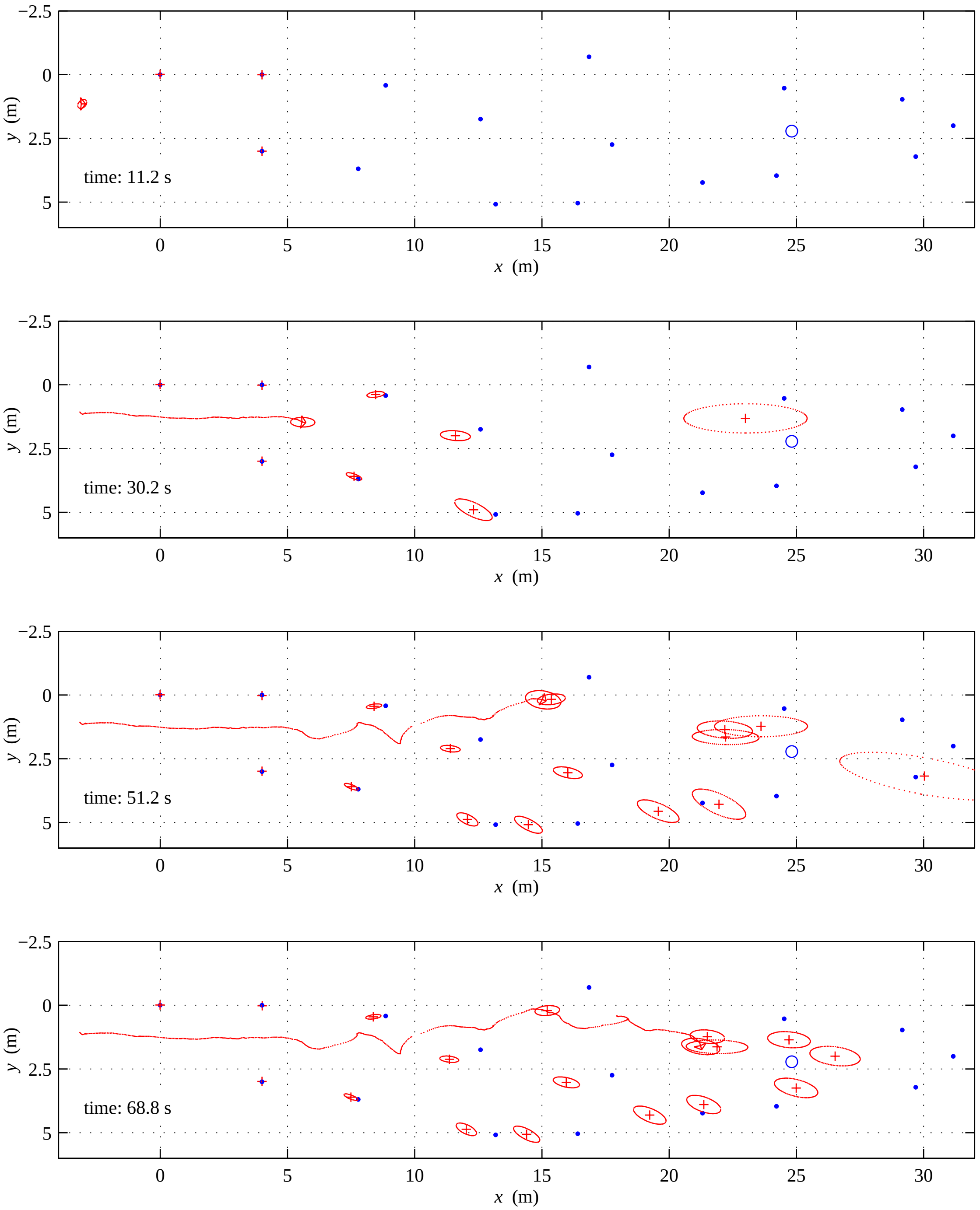

Figure 5.10: Absolute position estimates, run 1

Blue dots show absolute obstacle positions. The open blue circle shows true final vehicle position. The red $+$ with associated 3σ error ellipsoid shows estimated obstacle position, estimated vehicle position is shown by the red "wings" and associated 3σ error ellipsoid. The estimated vehicle path is shown by the red line.

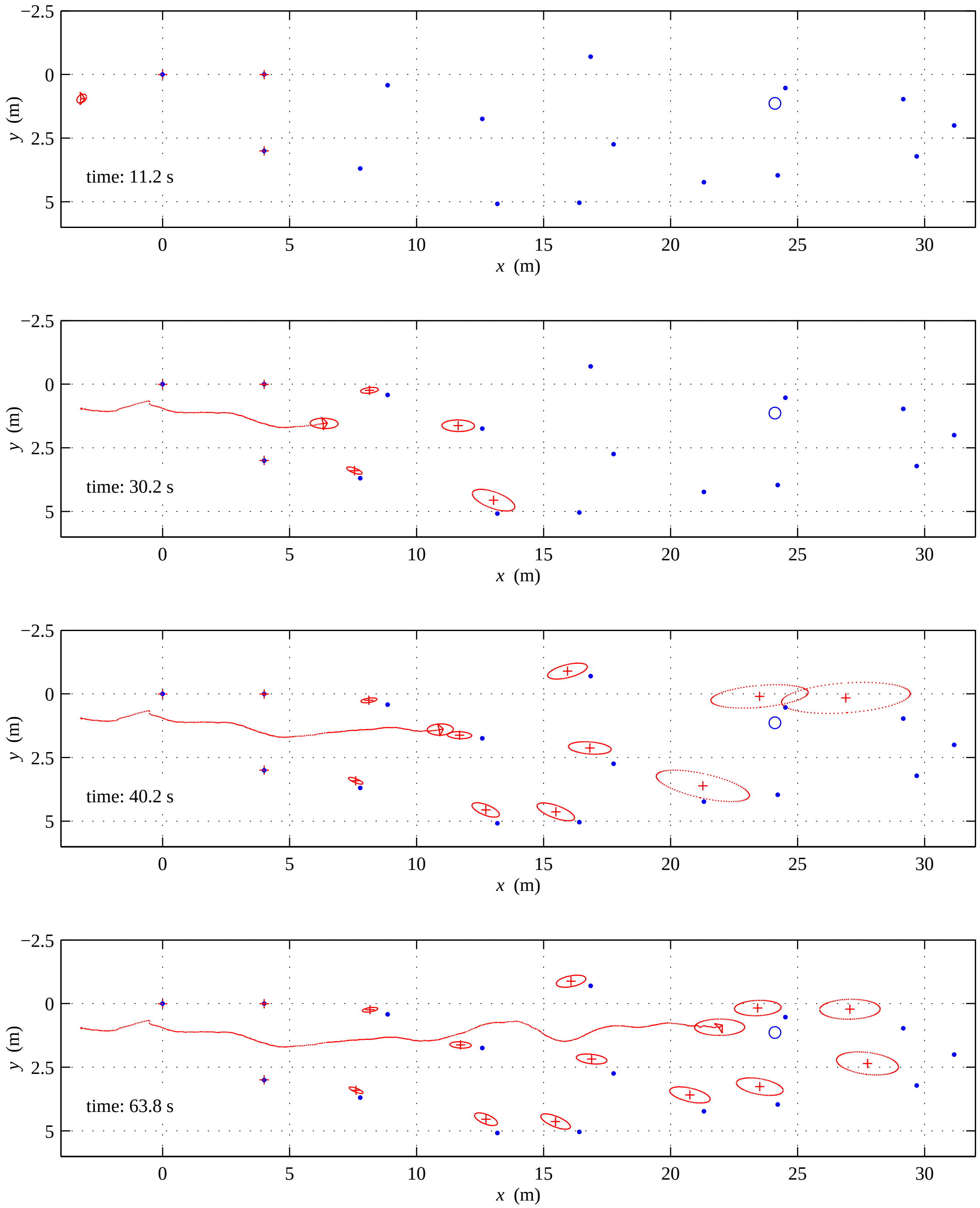

Figure 5.11: Absolute position estimates, run 2

Blue dots show absolute obstacle positions. The open blue circle shows true final vehicle position. The red $+$ *with associated* 3σ *error ellipsoid shows estimated obstacle position, estimated vehicle position is shown by the red “wings” and associated* 3σ *error ellipsoid. The estimated vehicle path is shown by the red line.*

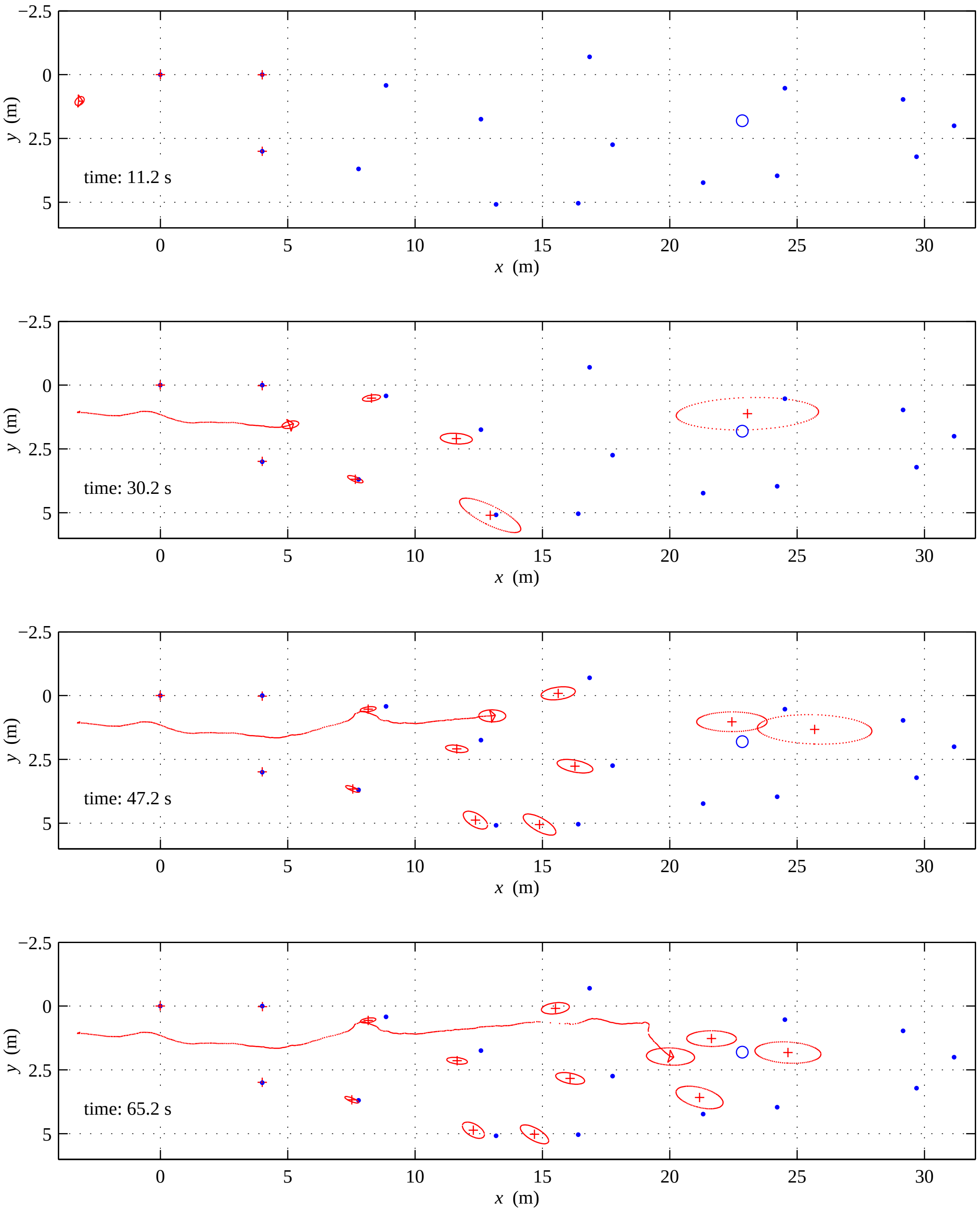

Figure 5.12: Absolute position estimates, run 3

Blue dots show absolute obstacle positions. The open blue circle shows true final vehicle position. The red $+$ *with associated* 3σ *error ellipsoid shows estimated obstacle position, estimated vehicle position is shown by the red "wings" and associated* 3σ *error ellipsoid. The estimated vehicle path is shown by the red line.*

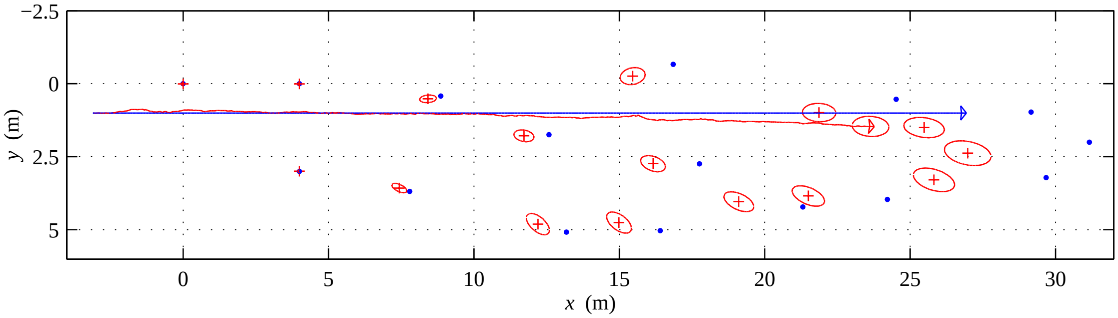

Figure 5.13: Simulation of error due to unmodeled camera pitch offset.

True obstacle locations shown as blue dots. True vehicle path shown as blue line, true final vehicle position shown by blue "wings". Estimated obstacle positions shown as red + with associated 3σ error ellipsoid. Estimated vehicle path shown as red line, estimated final vehicle position shown as red "wings" with associated 3σ error ellipsoid.

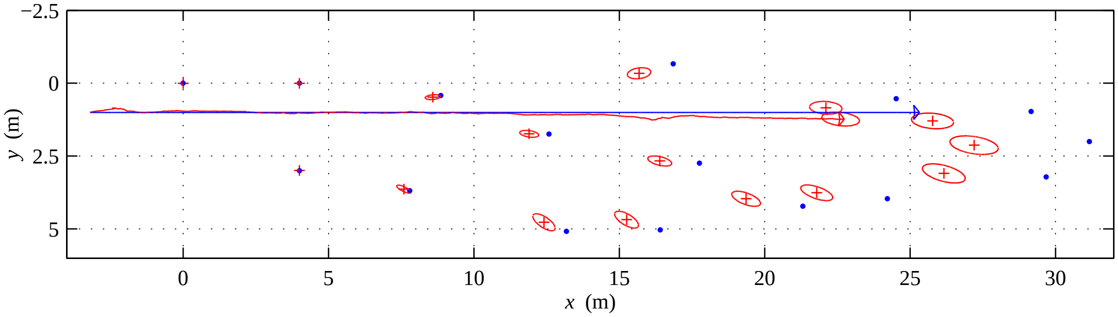

Figure 5.14: Simulation of error due to poor initial estimate of accelerometer bias.

True obstacle locations shown as blue dots. True vehicle path shown as blue line, true final vehicle position shown by blue "wings". Estimated obstacle positions shown as red + with associated 3σ error ellipsoid. Estimated vehicle path shown as red line, estimated final vehicle position shown as red "wings" with associated 3σ error ellipsoid.

drift over the course of the run. It is interesting to note that a 1° error in camera pitch results in an error of similar magnitude as was observed in the hardware test.

Figure 5.14 shows the effect of a 0.5m/s^2 error in the initial estimate of accelerometer bias in the body x direction. In the current hardware test setup, such an error would occur if the vehicle body is tilted by 3° in the pitch axis, as the projection of the acceleration due to gravity into the body axes would affect the computed bias. Since no effort was made to level the vehicle it is certainly feasible that it was rolled or pitched by a few degrees during IMU initialization.

As with the camera pitch offset, the map generated with initial error in accelerometer bias shows good initial map accuracy with a drift in position estimates that grows with distance traveled. Again the final vehicle position error is similar to that observed in hardware tests.

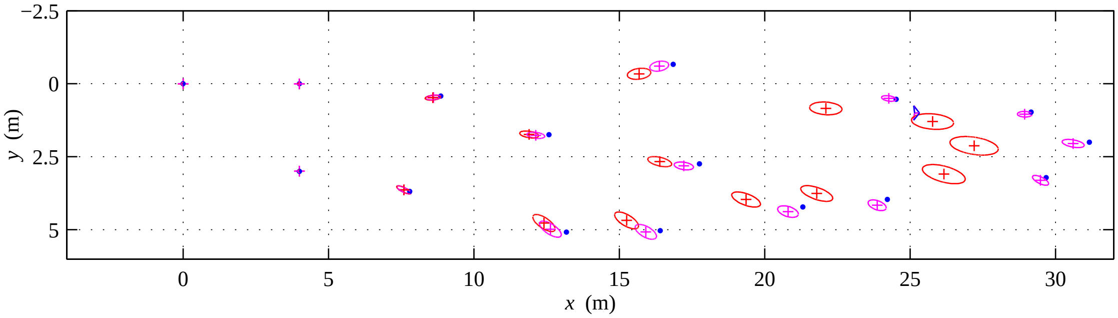

Figure 5.15: Map corrected using updated vehicle position.

True obstacle locations shown as blue dots, true final vehicle position shown by blue "wings". Uncorrected estimated obstacle positions shown as red + *with associated* 3σ *error ellipsoid. Corrected estimated obstacle positions shown as magenta* + *with associated* 3σ *error ellipsoid.*

5.5.1 Map Correction

Recall from Section 3.4 that the correction step requires the full covariance matrix at the time the correction is to occur. Hardware constraints precluded saving the full covariance matrix at each time step (only the diagonal blocks corresponding to state covariances could be saved due to disk access and real-time constraints) and the full covariance was not saved at the end of the run due to a programming oversight. Hardware test results can therefore not be used to demonstrate map correction. However, simulation results can illustrate the map correction step.

Figure 5.15 shows the correction step applied to the map of Figure 5.14. Additional information about the final vehicle position is used to correct the map, resulting in significantly higher accuracy.

The greatest improvement is obtained in the positions of landmarks that are currently in view of the vehicle, with less improvement in landmarks that have left the field of view. This suggests that unless absolute position updates are available at somewhat regular intervals, the system state vector should be augmented with past estimates of vehicle state. Choosing which past estimates to retain may depend on the current estimated uncertainty in vehicle position or some heuristic based on the number and geometry of the landmarks in view.

5.6 Summary

This section has presented results of a proof-of-concept demonstration using a small unmanned ground vehicle as test bed. The demonstration showed:

- **Vehicle state estimation:** The estimation of states required for flight control of a small UAV (altitude, roll, pitch) appears to be adequate to enable controlled flight.

- **Obstacle relative position estimation:** Estimates of obstacle relative position were internally consistent and adequate for obstacle avoidance.
- **Mapping:** Unmodeled system parameters (e.g. an offset in camera orientation) or poor initial estimates of inertial biases can cause significant drift in the mapping solution. This appears to be especially true of accelerometer bias in the x direction.

The drift in the mapping solution can be corrected by incorporation of additional information such as loop closure, observing a priori known landmarks or sporadic GPS updates.

Chapter 6

Conclusion

SAFE, AUTONOMOUS OPERATION in complex, cluttered environments is a critical challenge facing autonomous mobile systems. Significant advances in sensing, perception, estimation and data fusion, control, trajectory generation, and planning are required before truly autonomous systems can be deployed. This dissertation focused on the problem of state estimation using only an inertial measurement unit and a monocular camera.

The research in this dissertation was motivated by the problem of flying a small unmanned aerial vehicle (UAV) through a previously unsurveyed forest. The focus was on enabling three basic tasks: maintaining controlled flight while avoiding collisions with obstacles (i.e. the UAV can *aviate*); flying from a known start position to a known goal position (i.e. the UAV can *navigate*); providing knowledge of the environment– a map– to a human operator or other robots in the team (i.e. the UAV can *communicate*). Characteristics of both the environment and of the vehicle complicate these tasks.

In cluttered environments (such as natural and urban canyons or forests) signals from navigation beacons such as GPS may be frequently occluded. Direct measurements of vehicle position (necessary for navigation) are therefore unavailable. Additionally, payload limitations of small UAVs restrict both the mass and physical dimensions of sensors that can be carried on board.

Micro electromechanical inertial measurements units (IMUs) are well suited to small UAV applications and provide measurements of acceleration and angular rate. However, they do not provide information about nearby obstacles (needed for collision avoidance) and their noise and bias characteristics lead to unbounded growth in computed position. A monocular camera can provide bearings to nearby obstacles and landmarks. These bearings can be used both to enable obstacle avoidance and to aid navigation.

This research has been concerned with the development of a nonlinear recursive estimator which computes the state of a vehicle (its position, orientation and velocity) and the positions of obstacles in its environment using only a low-cost IMU and a monocular camera. Combined with a trajectory planner and a flight control system, the data from the estimator will enable a small UAV to *aviate* (maintain controlled flight while avoiding collisions with obstacles) and *navigate* (proceed to a goal) in an unknown, obstacle-strewn environment. The solution of the estimation problem focused on three main issues: design of an estimator able to provide consistent estimates of system state; data association; and landmark initialization.

The state estimation problem was cast in a framework of bearings-only Simultaneous Localization and Mapping (SLAM), with inertial measurements providing information about ego motion and bearings to landmarks (obtained from the vision system) providing information about the surroundings. The nonlinearities in system models combined with the likelihood of significant uncertainties in system states resulted in an estimation problem that could not be solved reliably using standard techniques. To address the problem of estimation in the face of nonlinearities and significant uncertainty, a Sigma Point Kalman Filter (SP-KF) was implemented and shown to provide consistent, reliable estimates of vehicle state and obstacle position, along with the associated covariance.

Landmarks are not uniquely labeled: therefore data association must be computed explicitly. In typical SLAM implementations data association is computed based on a comparison of the actual measurements with predictions computed from the current best estimate of vehicle position and landmark positions. In bearings-only SLAM applications (such as this one) data association is made more complex by the lack of full information provided by the measurements: the vision system projects a 3D world onto a 2D image plane. This measurement to map approach of data association is especially prone to failure when uncertainty in either vehicle state or landmark position is high,[1] and correct data association is a critical component of successful state estimation.

This dissertation has presented a two-step approach to data association. The first step compares current bearings with those obtained in the previous image frame to check frame to frame correspondence. The second step compares bearings with predictions based on landmarks in the current map. This approach is better able to perform data association when landmark position uncertainty is high and it is more robust to dropouts of both individual features (which may occur when a feature is occluded) and dropouts of an entire frame. Any bearing which is not associated with a mapped landmark is assumed to come from a new, previously unseen landmark.

When a landmark is seen for the first time, an initial estimate of range must be obtained. Like data association, this is complicated by the lack of sufficient measurements: a single bearing provides only enough information to localize a landmark along a ray but gives no information about distance. In this dissertation landmarks are assumed to lie on the ground plane. Using the estimate of aircraft position (including altitude) and orientation along with the measured bearing to the new landmark, an initial position estimate is computed at the intersection of the bearing and the ground plane.

[1] A landmark's position uncertainty is at its greatest when it is seen for the first time.

Simulations in 2D showed that the UKF-based estimator can provide consistent, reliable estimates of vehicle state and obstacle positions. Furthermore, these estimates can be used by a trajectory planner to generate safe trajectories through cluttered environments.

3D simulations were focused on error growth characteristics of the vehicle absolute position estimate. Since bearings only provide relative measurements, drift in estimated vehicle position is inevitable. In exploration flight this is manifested as an error which is approximately a constant percentage of distance traveled; in station keeping flight, where the same landmarks may be in continuous view, this is manifested as an error that varies cyclically with each orbit. Intuition further suggests that since each landmark provides independent bearing measurements, the estimated position error should vary inversely with the square root of the number of features in view. When data association is known a priori, this was observed in simulation.

When data association must be computed explicitly (which is the case for most real-world applications), the error in estimated vehicle position is smallest for relatively small numbers of landmarks in view. Too many landmarks in view increases the likelihood of errors in data association, leading to diverged estimates. The optimal number of landmarks which should be tracked is implementation dependent: for the simulations conducted here tracking approximately three landmarks resulted in the smallest error in vehicle position estimate.

Hardware tests and simulations were conducted for a small unmanned ground vehicle (UGV). While a UGV is nominally a 3DOF vehicle, estimation was performed for the full 6DOF inherent to a small UAV. Hardware tests showed that altitude was estimated with an average accuracy of 12cm, the estimated 1σ uncertainty was approximately 6cm. The estimated 1σ uncertainty for pitch and roll was approximately $0.3°$. If similar performance can be achieved on a small UAV, this is likely to be adequate for flight control.

Relative obstacle position estimation accuracy was examined by plotting estimated relative vehicle position with respect to true obstacle positions for obstacles near the vehicle. These generally agreed within estimated 3σ bounds, indicating that relative obstacle position estimation was successful.

The expected drift in absolute vehicle and landmark position was also observed in hardware tests. In each of the three runs the drift was of similar magnitude and direction and exceeded the estimated position uncertainty. This indicates the presence of a systemic bias, which can be explained by an unmodeled pitch offset in the camera or by poor initial estimates of IMU biases. Simulation results showed that the drift in absolute vehicle and obstacle positions can be corrected by smoothing.

6.1 Summary of Contributions

6.1.1 Framework for Inertial/Visual Control and Navigation

A framework which enables control and navigation of a small autonomous vehicle has been developed and implemented. This new system fuses data from a low-cost, low power MEMS inertial measurement unit and a light-weight CCD camera to reduce drift associated with pure inertial navigation solutions and to address the technical issues associated with monocular vision only navigation solutions.

6.1.2 Estimator Design

An estimator based on the Unscented Kalman Filter was developed in the context of this framework. Vehicle state (position, orientation, velocity), IMU biases and obstacle positions are estimated. This information was used by a trajectory planner to compute safe paths through a cluttered environment.

6.1.3 Performance Verification: Simulation

Results of Monte Carlo simulations of UAV flight in obstacle-strewn environments show that the UKF-based implementation provides a convergent, consistent solution to the estimation problem. Mean error is small and the error covariance is accurately predicted. Monte Carlo simulations investigating error growth characteristics were conducted for two classes of flight: exploration (where new terrain is being explored) and station keeping (where a set of landmarks may be in continuous view). For exploration flight the estimated vehicle position estimate error is an approximately constant percentage of distance traveled, for station keeping flight vehicle position estimate error is approximately constant. For both classes the magnitude of the error varies inversely with square root of the number of landmarks in view.

6.1.4 Performance Verification: Hardware

Navigation in a cluttered environment by a small Unmanned Ground Vehicle using only a low cost IMU and vision sensor was demonstrated. This showed successful state estimation on an operational system, with real sensor measurements and model and calibration errors. In addition, the hardware tests demonstrated real-time integration of the estimation algorithm with an obstacle avoidance and navigation algorithm.

6.2 Recommendations for Future Work

Research programs tend to generate more questions than answers, and this one was no exception. What follows is by no means an exhaustive list, and in most cases extensive research is already underway in the subjects mentioned.

6.2.1 Observability Analysis

Simulations have suggested that observability of inertial biases is strongly coupled with the translational degrees of freedom. Hence, the unavailability of direct position measurements leads to position uncertainty being strongly coupled with inertial biases. A careful analysis may provide insight into methods to improve observability through appropriate choice of landmarks, trajectories or additional sensors.

6.2.2 Trajectory Generation

Most trajectory generators assume perfect knowledge of the surrounding environment. In this case, not only is the knowledge imprecise, it is changing with time. The imprecision in knowledge is represented by the covariance of the state estimate and this can be used to compute a probability of collision. However, the change in uncertainty with vehicle motion suggests that new trajectories should be generated periodically. How often trajectories should be generated, and what should trigger generation of a new trajectory, remains an open question.

Additionally, the choice of trajectory has a strong effect on the accuracy of landmark position estimation, and this in turn couples with vehicle state estimation. This can be used to generate trajectories which optimize the accuracy of position estimates.

6.2.3 Alternate State Representations

This dissertation proposed estimating absolute obstacle positions as a means of reducing computational complexity. It was found that the number of landmarks that should be tracked is actually quite small (approximately five), and this in itself limits computational complexity. It is worth investigating the utility of estimating relative obstacle position, which is observable.

A possible approach is to estimate relative position for carefully chosen landmarks. Periodically these landmarks would be incorporated into a global map and used to aid in vehicle position estimation. How to perform this step is an area for research. Several methods have been proposed for scalable mapping in SLAM (e.g. [12], [5]), this approach may be applicable. Alternately, variants of correlation-based approaches as described in [14] or [45] may be suitable.

6.2.4 Additional Sensors/Data

In principle it would be straightforward to incorporate additional sensors in the framework and the estimator: it would only require the addition of measurement models to describe the sensors.

Range sensor

A range sensor such as a laser rangefinder should greatly improve overall estimator performance by improving data association, landmark initialization and state estimation. A laser rangefinder would add weight, increase power requirements and make the sensor package non-passive. However, the improvements may be worth the costs.

Multiple cameras

Adding a second camera (with the two cameras configured as a stereo pair) would give range to nearby landmarks. Far away landmarks could still be localized using vehicle motion, but the availability of range to nearby landmarks would greatly improve the estimates of motion between successive images, improving overall system observability.

An alternate approach is to mount cameras in such a way that field of view is maximized. This would still limit measurements to bearings, but the increased field of view will increase the length of time landmarks are in view. Additionally, bearings from side-pointing cameras will improve information available for estimating in-track motion. It is interesting to note that many small birds have eyes that point outwards, giving a wide field of view at the expense of stereo-based depth information in the forward direction.

Optical flow

There is a significant amount of information available in a stream of images that is not being used in this research. Optical flow could provide an independent estimate of vehicle velocity.

Air data sensors

Sensors of barometric altitude and airspeed would help with estimating altitude and speed. However, it is uncertain if the measurements will be accurate at low speed, and the uncertainty in barometric altitude (typically ±15 feet) reduces utility at low altitude.

Compass

A magnetometer provides measurements of heading and pitch, both of which would help the estimation process by fixing the directions of a local coordinate frame. However, measurements can be corrupted by local anomalies.

GPS

Global Positioning System measurements would provide absolute position measurements, removing the drift in the estimated vehicle and landmark position estimates. Measurements can be either tightly coupled (where pseudo-ranges are used directly) or loosely coupled, where a separate GPS positioning system computes position for incorporation as a ‘measurement’ in the state estimator. A tightly coupled system is more difficult to implement but has the advantage of using pseudo-ranges even when not enough satellites are visible to permit independent computation of position.

6.2.5 Other Vehicles and Other Environments

Implementation on other classes of vehicle (such as Autonomous Underwater Vehicles) is in principle straightforward. Issues will arise in the use of additional information that may become available due to vehicle-specific sensors or models. Two specific examples are navigation for planetary rovers and sea-floor navigation for Autonomous Underwater Vehicles.

Single-cycle instrument placement for Planetary Rovers

It currently takes three sols (Martian days) and multiple transmission of commands to place a science instrument on a rock from a start position 10m away from the target. A typical command sequence may consist of a command to drive forwards, followed by a turn, followed by a command to take pictures [9]. This is generated by Earth-based human operators using data transmitted by the rover. The Mars Exploration Rovers currently use a combination of inertial measurements, wheel odometry and visual odometry for navigation. This has been highly successful but periodic human intervention is still required [3].

Desired performance is single command, single sol instrument placement and the capability to sequence multiple science targets in a single command. An enormous amount of research has been done and is currently underway to enable this performance [41]. The research presented in this dissertation adds the capability to map landmarks in the environment. A command consisting of “Obtain measurements from rocks located at positions $(x_1\ y_1\ z_1)$ and $(x_2\ y_2\ z_2)$, return to $(x_0\ y_0\ z_0)$ and map any interesting features seen along the way” could then be given.

Benthic navigation for Underwater Vehicles

Autonomous underwater vehicles (AUVs) do not have access to GPS signals. Navigation systems such as arrays of acoustic transducers can be used, but they are expensive to deploy and maintain, and would require deployment in any area where AUV operations are required.

A Terrain Aided Approach using inertial measurements aided by multi-beam sonar and a map of the sea bed has been proposed in [38]. This requires a priori knowledge of the environment, and thus cannot be used in unsurveyed areas. A SLAM approach using sonar is described in [57].

Approaches using correlation of images from a downward looking camera are described in [14] and [45]. These methods rely on accurate measurements of vehicle orientation (through tilt sensors and magnetic compass), depth and altitude above the seafloor, and estimate vehicle xy position. These methods are not suitable for navigation in areas with significant relief (i.e. canyons, caves or among thermal vents). An approach using visual features combined with inertial measurements as described in this dissertation would allow sea floor navigation in areas with significant relief.

6.2.6 Multiple Vehicles

Applying this technology to multiple vehicles (especially a heterogeneous fleet of vehicles) will require a means to fuse maps. A difficult part of the map fusion problem is data association: which landmarks in a map correspond to landmarks in another map. A promising technique has been proposed in [51], but integration into the current system requires investigation.

6.3 Some Very Informal Final Thoughts

The dissertation proper ended with the previous section. This section is like the final scene in *Ferris Bueller's Day Off*, where Ferris comes out of the shower after the credits have rolled and says "Why are you still here? The movie is over. Go home."[2]

A common question I've been asked is "How did you come up with this topic?" This section attempts to answer the question (very informally) and then discusses a very difficult research problem which this dissertation did not address, but which must be solved if robots are to interact usefully with real-world environments.

How did I get started?

When I joined the ARL I began working on refurbishing and upgrading OTTER, a small, intervention capable Autonomous Underwater Vehicle. Aaron Plotnik and Kristof Richmond were also involved in this effort as we attempted to revive a vehicle that had lain dormant for some time. As part of the underwater research group I spent two days hanging over the rail of the Monterey Bay Aquarium Research Institute's ship R/V *Point Lobos* feeling very seasick[3] while the ROV *Ventana* was following jellyfish (Jason Rife's, and now Aaron Plotnik's thesis research) and making visual mosaics of the ocean floor (extending the lab's earlier work and starting Kristof's thesis research).

I was interested in the problem of performing tasks using teams of cooperating robots, for example assembling large, potentially delicate structures, and had thought about using OTTER as a

[2] Or it's like the post-credits scene in *Carrie* where the hand comes out of the grave for a final shock.

[3] Ginger tea doesn't really help nausea that much.

demonstration test bed. Earlier in the history of the ARL people had worked on cooperative manipulation using teams of free flying robots (see for example William Dickson's dissertation), and I was most interested in the problem of having a team of robots cooperatively estimate the position and orientation of the object so the control techniques developed earlier could be applied. This process of cooperative estimation would have to be robust to failures in communication between the robots and would have to be amenable to implementation in cases where significant limits on communication bandwidth exist (Wi-Fi is not available underwater). Applications of this technology also existed in construction of outposts on Mars, the Moon or in Earth orbit by teams of robots. Thus a project on cooperative manipulation slowly morphed into a project on cooperative estimation. Also, I had seen a few papers on flocking behavior by teams of robots (these all seemed to be strongly influenced by a paper written by Craig Reynolds and presented at SIGGRAPH in 1987). All these papers assumed that each robot had knowledge of itself, its flock mates and the environment. In real life this information would not always be available, further indicating that cooperative estimation was a necessary area of research. I began with cooperative estimation of obstacles by a team of mobile robots, but before I published anything the robot team turned into a single robot (doing something with a team before you can do it with a single robot seemed like putting the cart before the horse, unless I added several assumptions that for æsthetic reasons I didn't wish to make). So a team of robots cooperatively estimating the state of a single object turned into a single robot estimating the positions of many objects... and the forest flying project was born.

A hard problem

A critical and very difficult problem that pervades many aspects of autonomous operations and interaction with the environment is *perception*. By perception I mean the process of interpreting sensor data and extracting useful information. Just as research in control or planning generally assumes that knowledge of state is available, most research in estimation assumes that a sensing system provides a particular measurement without worrying specifically about how this measurement is produced. At the beginning of my work on forest flight I assumed that it would be rather easy for a machine vision algorithm to detect tree trunks in an image: it is certainly very easy for a human to see tree trunks in a picture of a forest like the one in Figure 1.1. Experience proved otherwise, however. Even performing reliable color segmentation in a natural environment, with its regions of bright sunlight and dark shadows, proved to be extremely difficult. Algorithms that worked well in uniformly lit indoor environments failed completely outdoors. Changing color spaces (normalized RGB to HSV) made a huge difference in performance, but not enough that reliable color segmentation could be performed outside, in a forest on a sunny day.

Reliable and repeatable feature extraction is thus a key issue with many implications. A useful landmark is recognizable (and distinguishable) from different points of view, from different distances and by different autonomous robots. Distinguishable landmarks obviate the need for explicit data association, both for progress in unexplored areas, realizing when previously explored areas are entered and for operations in fully mapped environments. Scale Invariant Feature Transform (SIFT) features show great promise, but do not explicitly connect a visual feature with what a human would consider a useful landmark. It may be that combining different features (such as a corner with a SIFT feature) would result in an easily recognizable landmark, one that can be used by different robots operating simultaneously or that can be easily described and recognized for robots operating in mapped areas.

Appendix A

Information Required for Flight Control

The information required for flight control is well known can can be obtained from any textbook dealing with flight control systems. This Appendix uses the Stanford DragonFly UAV [20] as an illustrative example (see Figure A.1).

For small perturbations about trimmed straight and level flight the equations of motion can be linearized. Furthermore, for aircraft that are symmetric about the xz plane the longitudinal and lateral modes are decoupled. For a symmetric aircraft in trimmed straight and level flight the equations of motion for the longitudinal and lateral dynamics, respectively, can be written in state space form as:

$$\begin{aligned}\begin{bmatrix} \delta \dot{v_T} \\ \delta\dot{\alpha} \\ \delta\dot{\theta} \\ \dot{q} \end{bmatrix} &= \begin{bmatrix} X_V & X_\alpha & -g\cos\gamma_e & 0 \\ Z_V & Z_\alpha & g\sin\gamma_e & 1+Z_q \\ 0 & 0 & 0 & 1 \\ M_V & M_\alpha & 0 & M_q \end{bmatrix} \begin{bmatrix} \delta v_T \\ \delta\alpha \\ \delta\theta \\ q \end{bmatrix} \\ &+ \begin{bmatrix} X_{\delta_e} & X_{\delta_t}\cos\alpha_e \\ Z_{\delta_e} & Z_{\delta_t}\sin\alpha_e \\ 0 & 0 \\ M_{\delta_e} & M_{\delta_t} \end{bmatrix} \begin{bmatrix} \Delta\delta_e \\ \Delta\delta_t \end{bmatrix}\end{aligned} \tag{A.1}$$

$$\begin{bmatrix} \delta\dot{\beta} \\ \dot{p} \\ \dot{r} \\ \delta\dot{\phi} \end{bmatrix} = \begin{bmatrix} Y'_\beta & Y'_p & 1-Y'_r & g\cos\theta_e/V_T \\ L_\beta & L_p & L_r & 0 \\ N_\beta & N_p & N_r & 0 \\ 0 & \cos\gamma_e\sec\theta_e & \sin\gamma_e\sec\theta_e & 0 \end{bmatrix} \begin{bmatrix} \delta\beta \\ p \\ r \\ \delta\phi \end{bmatrix}$$

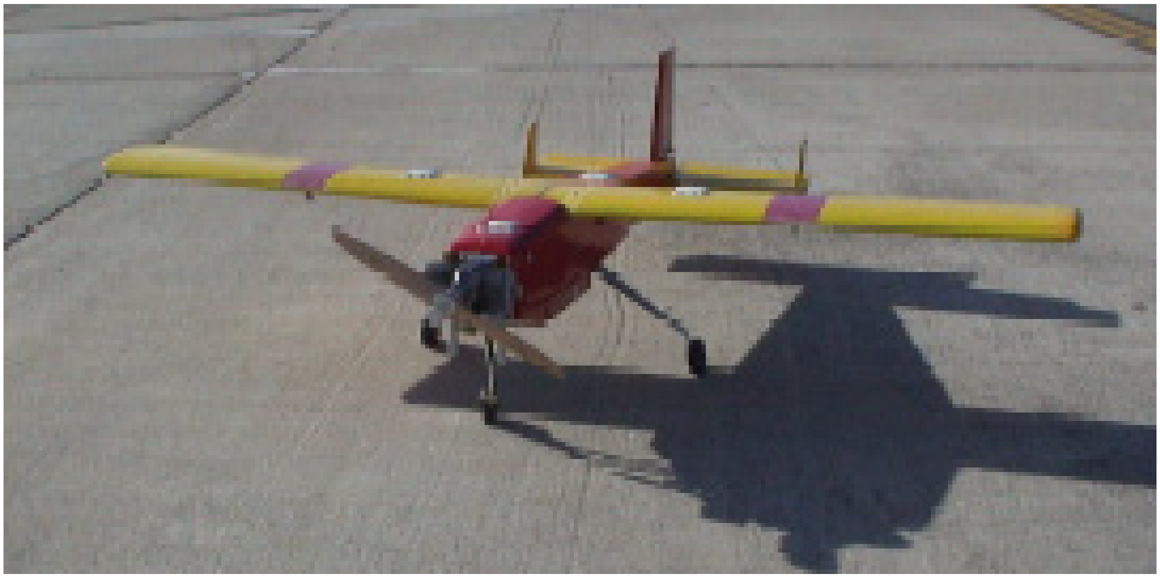

Figure A.1: The Stanford DragonFly UAV.

$$
+ \begin{bmatrix} Y'_{\delta_a} & Y'_{\delta_r} \\ L_{\delta_a} & L_{\delta_r} \\ N_{\delta_a} & N_{\delta_r} \\ 0 & 0 \end{bmatrix} \begin{bmatrix} \Delta\delta_a \\ \Delta\delta_r \end{bmatrix} \tag{A.2}
$$

The longitudinal state vector $[\delta v_T \ \delta\alpha \ \delta\theta \ q]^T$ represents small perturbations in airspeed, angle of attack, pitch angle and pitch rate; the lateral state vector $[\delta\beta \ p \ r \ \delta\phi]^T$ represents small perturbations in sideslip angle, roll rate, yaw rate and roll angle respectively. Control inputs are $[\Delta\delta_e \ \Delta\delta_t]^T$ representing small perturbations in elevator angle and throttle, respectively and $[\Delta\delta_a \ \Delta\delta_r]^T$ representing small perturbations in aileron angle and rudder angle, respectively. Terms such as X_V represent stability derivatives, which must be obtained through analysis or flight testing.

The eigenvalues of the state transition matrix represent the poles of the stick-fixed aircraft, i.e. the natural modes of the aircraft. The corresponding eigenvectors represent the mode shapes, i.e. the degrees of freedom which are excited by the particular mode. In order to detect (and hence control) a given mode, a measurement or estimate of highly excited degrees of freedom should be available. Hence examining the mode shapes gives an idea of the sensors or estimates required to control the aircraft.

Table A.1 gives longitudinal modes for the Stanford Dragonfly UAV (from Jang [20]). The short period mode occurs at high frequency with fairly low damping and consists primarily of excitation of the pitch rate q. The phugoid mode occurs at lower frequency with higher damping and consists primarily of excitation of airspeed.

Table A.1: Longitudinal modes for Dragonfly UAV.

Computed from data given in Jang [20]. Mode shape is the magnitude of the complex eigenvector associated with an eigenvalue.

	Short Period	**Phugoid**
Pole	$-2.88 \pm 6.82i$	$-0.15 \pm 0.20i$
ω (rad/s)	7.4	0.25
ζ	0.4	0.6
shape $[\delta v_T \ \delta\alpha \ \delta\theta \ q]^T$	$[0.314 \ 0.295 \ 0.121 \ 0.895]^T$	$[0.999 \ 0.003 \ 0.027 \ 0.007]^T$

Table A.2: Lateral modes for Dragonfly UAV

Computed from data given in Jang [20]. Mode shape is the magnitude of the complex eigenvector associated with an eigenvalue.

	Dutch Roll	**Roll**	**Spiral**
Pole	$-1.14 \pm 3.774i$	-5.36	-0.019
ω (rad/s)	3.9		
ζ	0.29	$\tau = 0.19$	$\tau = 52.6$
shape $[\delta\beta \ p \ r \ \delta\phi]^T$	$[0.19 \ 0.64 \ 0.76 \ 0.15]^T$	$[0.01 \ 0.98 \ 0.05 \ 0.18]^T$	$[0.03 \ 0.02 \ 0.31 \ 0.95]^T$

Table A.2 gives lateral modes for the Stanford Dragonfly UAV (from Jang [20]). Dutch roll consists primarily of excitation of roll rate p and yaw rate r. Roll subsidence is a stable, short time constant first order mode with primarily roll rate excitation. The spiral mode is a long time constant first order excitation primarily of roll angle ϕ. In this case the spiral mode is stable but in many aircraft the spiral mode is divergent.

Thus for flight control angular rates p, q, r, airspeed and roll angle ϕ are required. For more complex tasks (such as altitude hold or heading hold) more information is required.

Appendix B

Estimator Summary

This appendix summarizes all the equations necessary for the estimator described in Section 3.1 and provides initialization and noise parameters for the simulations described in Section 4.2.

B.1 Estimator Equations

Given the state vector

$$\mathbf{x} = \begin{bmatrix} \mathbf{x}_v \\ \mathbf{x}_o \end{bmatrix} \tag{B.1}$$

where

$$\mathbf{x}_v = \begin{bmatrix} x & y & z & \phi & \theta & \psi & u & v & w & \boldsymbol{\alpha}^T & \mathbf{b}_a^T & \mathbf{b}_\omega^T \end{bmatrix}^T \tag{B.2}$$

and

$$\mathbf{x}_o = \begin{bmatrix} \mathbf{x}_1^T & \mathbf{x}_2^T & \cdots & \mathbf{x}_m^T \end{bmatrix}^T \tag{B.3}$$

The system is described by a kinematic process model

$$\dot{\mathbf{x}} = f(\mathbf{x}, \mathbf{u}) \tag{B.4}$$

(defined in Equations 2.13–2.18) and a measurement model

$$\mathbf{z}_{imu} = g_1(\mathbf{x}, \mathbf{u}) \tag{B.5}$$

$$\mathbf{z}_{cam} = g_2(\mathbf{x}) \tag{B.6}$$

which is defined in Equations 2.24, 2.20, and 2.29.

B.1.1 Kinematics

Substituting the inertial measurement model g_1 into the process model gives

$$\dot{\mathbf{x}} = \begin{bmatrix} \dot{\mathbf{x}}_v \\ \dot{\mathbf{x}}_o \end{bmatrix} = \begin{bmatrix} f_v(\mathbf{x}_v, \mathbf{z}_{imu}) \\ 0 \end{bmatrix} + \begin{bmatrix} \mathbf{n}_{ext} \\ 0 \end{bmatrix} \tag{B.7}$$

where $\mathbf{z}_{imu} = [z_x \; z_y \; z_z \; z_p \; z_q \; z_r]^T$. Landmarks are assumed to be stationary. Expanding the vehicle kinematics $\dot{\mathbf{x}}_v = f_v(\mathbf{x}_v, \mathbf{z}_{imu})$ gives

$$\dot{x} = \cos\theta\cos\psi\, u + (\sin\phi\sin\theta\cos\psi - \cos\phi\sin\psi)\, v + (\cos\phi\sin\theta\cos\psi + \sin\phi\sin\psi)\, w \tag{B.8}$$

$$\dot{y} = \cos\theta\sin\psi\, u + (\sin\phi\sin\theta\sin\psi + \cos\phi\cos\psi)\, v + (\cos\phi\sin\theta\sin\psi - \sin\phi\cos\psi)\, w \tag{B.9}$$

$$\dot{z} = -\sin\theta\, u + \sin\phi\cos\theta\, v + \cos\phi\cos\theta\, w \tag{B.10}$$

$$\dot{\phi} = (z_p - b_p) + \tan\theta \sin\phi (z_q - b_q) - \tan\theta \cos\phi (z_r - b_r) \tag{B.11}$$

$$\dot{\theta} = \cos\phi (z_q - b_q) - \sin\phi (z_r - b_r) \tag{B.12}$$

$$\dot{\psi} = \frac{\sin\phi}{\cos\theta}(z_q - b_q) + \frac{\cos\phi}{\cos\theta}(z_r - b_r) \tag{B.13}$$

$$\dot{u} = \frac{z_x}{\alpha_x} - g \sin\theta - b_x - (z_q - b_q)w + (z_r - b_r)v - b_x(\boldsymbol{\rho}) \tag{B.14}$$

$$\dot{v} = \frac{z_y}{\alpha_y} + g \cos\theta \sin\phi - b_y - (z_r - b_r)u + (z_p - b_p)w - b_y(\boldsymbol{\rho}) \tag{B.15}$$

$$\dot{w} = \frac{z_z}{\alpha_z} + g \cos\theta \cos\phi - b_z - (z_p - b_p)v + (z_q - b_q)u - b_z(\boldsymbol{\rho}) \tag{B.16}$$

$$\dot{\alpha}_x = 0 \tag{B.17}$$

$$\dot{\alpha}_y = 0 \tag{B.18}$$

$$\dot{\alpha}_z = 0 \tag{B.19}$$

$$\dot{b}_x = 0 \tag{B.20}$$

$$\dot{b}_y = 0 \tag{B.21}$$

$$\dot{b}_z = 0 \tag{B.22}$$

$$\dot{b}_p = 0 \tag{B.23}$$

$$\dot{b}_q = 0 \tag{B.24}$$

$$\dot{b}_r = 0 \tag{B.25}$$

This is converted to discrete form using a first order Euler integration, i.e.

$$\mathbf{x}_{k+1} = \begin{bmatrix} \mathbf{x}_{v,k+1} \\ \mathbf{x}_{o,k+1} \end{bmatrix} = \begin{bmatrix} \mathbf{x}_{v,k} + \delta t f_v(\mathbf{x}_{v,k}, \mathbf{z}_{imu,k}) \\ \mathbf{x}_{o,k} \end{bmatrix} + \begin{bmatrix} \mathbf{n}_{ext} \\ 0 \end{bmatrix} \tag{B.26}$$

where δt is the time step (50Hz in both simulation and hardware tests in this dissertation). The external noise term $\mathbf{n}_{ext}$ (whose symbol has been overloaded in the conversion to discrete time) includes the assumed noise of the random walk model for the IMU scale factor and bias drift. Using the superscript d to indicate the discrete process model,

$$\begin{bmatrix} \mathbf{x}_{v,k+1} \\ \mathbf{x}_{o,k+1} \end{bmatrix} = \begin{bmatrix} f_v^d(\mathbf{x}_{v,k}, \mathbf{z}_{imu,k}) \\ \mathbf{x}_{o,k} \end{bmatrix} + \begin{bmatrix} \mathbf{n}_{ext} \\ 0 \end{bmatrix} \tag{B.27}$$

The process noise is dependent on the IMU measurement noise and on the external noise $\mathbf{n}_{ext}$.

$$\mathbf{Q}_k = \begin{bmatrix} \mathbf{F}_z \Sigma_{imu} \mathbf{F}_z^T + \Sigma_{ext} & 0 \\ 0 & 0 \end{bmatrix} \tag{B.28}$$

where $\mathbf{F}_z = \nabla_{\mathbf{z}_{imu}} f_v^d$ (the Jacobian of the discrete process model with respect to the inertial measurements), Σ_{imu} is the covariance matrix describing the IMU measurement noise, and Σ_{ext} is the covariance describing the external noise, including drift of the IMU biases. In this dissertation no external disturbances was assumed to act on the vehicle, hence

$$\Sigma_{ext} = \begin{bmatrix} 0 & 0 \\ 0 & \Sigma_{biases} \end{bmatrix} \tag{B.29}$$

B.1.2 Vision Measurements

Bearing measurements to the i^{th} landmark are

$$\mathbf{z}_{cam,i} = \begin{bmatrix} \arctan \frac{s_{i,y}}{s_{i,x}} \\ \arctan \frac{s_{i,z}}{s_{i,x}} \end{bmatrix} + \mathbf{n}_c \tag{B.30}$$

The measurement is corrupted by zero-mean Gaussian noise $\mathbf{n}_c \sim \mathcal{N}(0, \mathbf{R}_{cam})$. $\mathbf{s}_i$ represents the vector from the camera to the i^{th} tree, expressed in the camera frame:

$$\mathbf{s}_i = \mathbf{T}_{cam} \left[\mathbf{T} \begin{bmatrix} x_i - x \\ y_i - y \\ z_i - z \end{bmatrix} - \triangle \mathbf{s} \right] \tag{B.31}$$

where $\triangle \mathbf{s}$ is the offset from the camera to the vehicle CG, expressed in the body frame. The transformation matrix $\mathbf{T}_{cam}$ defines the transformation of a vector expressed in the body frame into the camera frame. The matrix $\mathbf{T}$ defines the transformation of a vector expressed in the inertial frame into the body frame, and is given by

$$\mathbf{T} = \begin{bmatrix} \cos\theta\cos\psi & \cos\theta\sin\psi & -\sin\theta \\ \sin\phi\sin\theta\cos\psi - \cos\phi\sin\psi & \sin\phi\sin\theta\sin\psi + \cos\phi\cos\psi & \sin\phi\cos\theta \\ \cos\phi\sin\theta\cos\psi + \sin\phi\sin\psi & \cos\phi\sin\theta\sin\psi - \sin\phi\cos\psi & \cos\phi\cos\theta \end{bmatrix} \tag{B.32}$$

B.2 Simulation Parameters

This section provides the initialization and noise parameters for the simulations presented in Section 4.2.

Exploration

Initial vehicle state:

$$\mathbf{x}_{v,0} = \begin{bmatrix} 0 & -40 & -5 & 0.7955 & 0 & 0 & 10 & 0 & 0 & 1 & 1 & 1 & 0 & 0 & 0 & 0 & 0 & 0 \end{bmatrix}^T \tag{B.33}$$

Input (required acceleration and $\boldsymbol{\omega}$ to maintain circular flight)

$$\mathbf{u} = \begin{bmatrix} 0 & 0 & 0 & 0 & 0.3571 & 0.35 \end{bmatrix}^T \tag{B.34}$$

Station Keeping

Initial vehicle state:

$$\mathbf{x}_{v,0} = \begin{bmatrix} 0 & -200 & -100 & 0.2013 & 0 & 0 & 20 & 0 & 0 & 1 & 1 & 1 & 0 & 0 & 0 & 0 & 0 & 0 \end{bmatrix}^T \tag{B.35}$$

Input (required acceleration and $\boldsymbol{\omega}$ to maintain circular flight)

$$\mathbf{u} = \begin{bmatrix} 0 & 0 & 0 & 0 & 0.02 & 0.098 \end{bmatrix}^T \tag{B.36}$$

Initial State and Noise Covariance

In the following equations $\mathbf{I}_{3\times3}$ denotes the 3×3 identity matrix. 0 is the zero matrix of appropriate dimension.

Initial state covariance:

$$\mathbf{P}_0 = \begin{bmatrix} 0.01^2\mathbf{I}_{3\times3} & 0 & 0 & 0 & 0 & 0 \\ 0 & 0.001^2\mathbf{I}_{3\times3} & 0 & 0 & 0 & 0 \\ 0 & 0 & 0.01^2\mathbf{I}_{3\times3} & 0 & 0 & 0 \\ 0 & 0 & 0 & 0.01^2\mathbf{I}_{3\times3} & 0 & 0 \\ 0 & 0 & 0 & 0 & 0.025^2\mathbf{I}_{3\times3} & 0 \\ 0 & 0 & 0 & 0 & 0 & 0.001^2\mathbf{I}_{3\times3} \end{bmatrix} \tag{B.37}$$

IMU bias drift covariance:

$$\Sigma_{biases} = \begin{bmatrix} 0.001^2\mathbf{I}_{3\times3} & 0 & 0 \\ 0 & 0.001^2\mathbf{I}_{3\times3} & 0 \\ 0 & 0 & 0.0001^2\mathbf{I}_{3\times3} \end{bmatrix} \tag{B.38}$$

IMU measurement noise covariance:

$$\Sigma_{imu} = \begin{bmatrix} 0.08^2\mathbf{I}_{3\times3} & 0 \\ 0 & 0.008^2\mathbf{I}_{3\times3} \end{bmatrix} \tag{B.39}$$

Vision measurement noise covariance (equivalent to 1° error in bearing):

$$\mathbf{R}_{cam} = \begin{bmatrix} 0.0175^2 & 0 \\ 0 & 0.0175^2 \end{bmatrix} \tag{B.40}$$

Bibliography

[1] Omead Amidi. *An Autonomous Vision Guided Helicopter*. PhD thesis, Carnegie Mellon University, Pittsburgh, PA, August 1996.

[2] Tim Bailey. Constrained initialisation for bearing-only SLAM. In *IEEE International Conference on Robotics and Automation (ICRA)*, Taipei, Taiwan, 2003. IEEE.

[3] J. Biesiadecki, C. Leger, and M. Maimone. Tradeoffs between directed and autonomous driving on the Mars Exploration Rovers. In *International Symposium of Robotics Research*, San Francisco, California, October 2005.

[4] John H. Blakelock. *Automatic Control of Aircraft and Missiles*. Wiley Interscience, New York, 2nd edition, 1991.

[5] M. Bosse, P. Newman, J. Leonard, M. Soika, W. Feiten, and S. Teller. An atlas framework for scalable mapping. In *Proceedings of the IEEE International Conference on Robotics and Automation (ICRA)*, 2003.

[6] Jean-Yves Bouget. Camera calibration toolbox for matlab. http://www.vision.caltech.edu /bouguetj/calib_doc/index.html.

[7] Arthur E. Bryson. *Control of Spacecraft and Aircraft*. Princeton University Press, Princeton, New Jersey, 1994.

[8] Darius Burschka and Gregory D. Hager. V-GPS(SLAM): Vision based inertial system for mobile robots. In *IEEE International Conference on Robotics and Automation*, New Orleans, LA, April 2004.

[9] Yang Cheng, Mark Maimone, and Larry Matthies. Visual odometry on the Mars Exploration Rovers. In *IEEE Conference on Systems, Man and Cybernetics*, The Big Island, Hawaii, October 2005.

[10] Andrew J. Davison. Real-time simultaneous localisation and mapping with a single camera. In *International Conference on Computer Vision*, Nice, France, October 2003.

[11] David D. Diel, Paul DeBitetto, and Seth Teller. Epipolar constraints for vision-aided inertial navigation. In *IEEE Workshop on Motion and Video Computing*. IEEE, 2005.

[12] Gamini Dissanayake, Stefan B. Williams, Hugh Durrant-Whyte, and Tim Bailey. Map management for efficient simultaneous localization and mapping (SLAM). In *Autonomous Robots 12*, pages 267–286, 2002.

[13] Bernard Etkin and Lloyd Duff Reid. *Dynamics of Flight: Stability and Control*. John Wiley & Sons, New York, 3rd edition, 1996.

[14] R. Eustice, H. Singh, J. Leonard, M. Walter, and R. Ballard. Visually navigating the RMS Titanic with SLAM information filters. In *Proceedings of Robotics: Science and Systems (RSS)*, Cambridge, MA, USA, June 2005.

[15] Trevor Fitzgibbons and Eduardo Nebot. Bearing only SLAM using colour-based feature tracking. In *2002 Australasian Conference on Robotics and Automation*, Auckland, New Zealand, 2002.

[16] Eric Foxlin and Leonid Naimark. Vis-tracker: A wearable vision-inertial self-tracker. In *IEEE VR2003*, Los Angeles, California USA, March 2003. IEEE, IEEE.

[17] D. Hsu, R. Kindel, J. C. Latombe, and S. Rock. Randomized kinodynamic motion planning with moving obstacles. *International Journal of Robotics Research*, 21(3):233–255, March 2002.

[18] Andreas Huster and Steve Rock. Relative position sensing by fusing monocular vision and inertial rate sensors. In *11th International Conference on Advanced Robotics (ICAR)*, 2003.

[19] Joam Sola i Ortega, Thomas Lemaire, Michel Decy, Simon Lacroix, and Andre Monin. Delayed vs undelayed landmark initialization for bearing only SLAM. In *Workshop on Simulateous Localisation and Mapping, International Conference on Robotics and Automation*, Barcelona, Spain, 2005.

[20] Jung Soon Jang. *Nonlinear Control Using Discrete Time Dynamic Inversion Under Input Saturation: Theory and Experiment on the Stanford Dragonfly UAVs*. PhD thesis, Stanford University, Department of Aeronautics and Astronautics, December 2003.

[21] S. J. Julier and J. K. Uhlmann. A new extension of the Kalman filter to nonlinear systems. In *AeroSense: The 11th Symposium on Aerospace/Defence Sensing, Simulation and Controls*, Orlando, Florida, 1997.

[22] Simon Julier and Jeffrey Uhlmann. Reduced sigma point filters for the propagation of means and covariances through nonlinear transformations. In *American Controls Conference*, Anchorage, Alaska, May 2002.

[23] Simon Julier, Jeffrey Uhlmann, and Hugh F. Durrant-Whyte. A new method for the nonlinear transformation of means and covariances in filters and estimators. *IEEE Transactions on Automatic Control*, 45(3):477–482, March 2000.

[24] T. Kailath, A. H. Sayed, and B. Hassibi. *Linear Estimation*. Prentice-Hall, 1st edition, March 2000.

[25] Jong Hyuk Kim and Salah Sukkarieh. Airborne simultaneous localisation and map building. In *IEEE International Conference on Robotics and Automation (ICRA)*, Taipei, Taiwan, 2003. IEEE.

[26] Jong Hyuk Kim and Salah Sukkarieh. Recasting SLAM–towards improving efficiency and platform independency. In *11th International Symposium of Robotics Research (ISRR)*, Siena, Italy, 2003.

[27] Jonghyuk Kim and Salah Sukkarieh. Autonomous airborne navigation in unknown environments. *IEEE Transactions on Aerospace and Electronic Systems*, 40(3):1031–1045, July 2004.

[28] N. M. Kwok and G. Dissanayake. An efficient multiple hypothesis filter for bearing-only SLAM. In *Interational Conference on Intelligent Robots and Systems*, Sendai, Japan, 2004.

[29] K. N. Leabourne, S. M. Rock, S. D. Fleischer, and R. L. Burton. Station keeping of an ROV using vision technology. In *OCEANS 97 Conference*, volume 1, pages 634–640, Halifax, Nova Scotia, October 1997. MTS/IEEE.

[30] Yufeng Liu and Sebastian Thrun. Results for outdoor-SLAM using sparse extended information filters. In *IEEE International Conference on Robotics and Automation (ICRA)*, Taipei, Taiwan, 2003. IEEE.

[31] Jorge Lobo and Jorge Dias. Integration of inertial information with vision. In *24th Conference of IEEE Industrial Electronics Society (IECON)*, pages 1263–1267, Aachen, Germany, 1998. IEEE.

[32] Richard L. Marks. *Experiments in Visual Sensing for Automatic Control of an Underwater Robot*. Ph.d. thesis, Stanford University, Department of Aeronautics and Astronautics, Stanford CA 94305, June 1995. Also published as SUDAAR 681.

[33] Marci Meingast, Christopher Geyer, and Shankar Sastry. Vision based terrain recovery for landing unmanned aerial vehicles. In *Conference on Decision and Control*, Bahamas, December 2005. IEEE.

[34] Luis Montesano, Jose Gaspar, Jose Santos-Victor, and Luis Montano. Fusing vision-based bearing measurements and motion to localize pairs of robots. In *International Conference on Robotics and Automation*, Barcelona, Spain, 2005.

[35] José Neira, Maria Isabel Ribeiro, and Juan Domingo Tardós. Mobile robot localization and map building using monocular vision. In *Fifth International Symposium on Intelligent Robotic Systems*, Stockholm, Sweden, 1997.

[36] José Neira and Juan D. Tardós. Data association in stochastic mapping using the joint compatibility test. *IEEE Transactions on Robotics and Automation*, 17(6):890–897, December 2001.

[37] Thomas Netter and Nicolas Franceschini. A robotic aircraft that follows terrain using a neuromorphic eye. In *IEEE/RSJ International Conference on Intelligent Robots and Systems (IROS)*, Lausanne, Switzerland, 2002.

[38] Ingemar Nygren. *Terrain Navigation for Underwater Vehicles*. Ph.d. thesis, Royal Institute of Technology (KTH, Stockholm, Sweden, 2005.

[39] O-Navi. http://www.o-navi.com.

[40] O-Navi, LLC, PO Box 27213, San Diego CA 92198-1213. *Phoenix/AX 6DOF/GPS Sensor Module Quick Start Guide*, rev. x10 edition, April 2004.

[41] L. Pedersen, M. Bualat, D. Lees, D. Smith, and R. Washington. Integrated demonstration of instrument placement, robust execution and contingency planning. In *iSAIRAS*, Nara, Japan, 2003.

[42] M. Pollefeys, L. Van Gool, M. Vergauwen, K. Cornelis, F. Verbiest, and J. Tops. 3D capture of archaeology and architecture with a hand-held camera. In *ISPRS workshop on Vision Techniques for Digital Architectural and Archaeological Archives*, pages 262–267, Ancona, Italy, July 2003.

[43] Richard J. Prazenica, Adam Watkins, Andrew J. Kurdila, Qi Fa Ke, and Takeo Kanade. Vision-based Kalman filtering for aircraft state estimation and structure from motion. In *AIAA Guidance, Navigation and Control Conference*, San Francisco, California, August 2005. American Institute of Aeronautics and Astronautics.

[44] Alison Proctor and Eric N. Johnson. Vision-only approach and landing. In *AIAA Guidance, Navigation and Control Conference*, San Francisco, California, August 2005. American Institute of Aeronautics and Astronautics.

[45] Kristof Richmond and Stephen Rock. A real-time visual mosaicking and navigation system. In *Unmanned Untethered Submersible Technology*, Durham, New Hampshire, August 2005. AUSI.

[46] Jonathan M. Roberts, Peter I. Corke, and Gregg Buskey. Low-cost flight control system for a small autonomous helicopter. In *2002 Australasian Conference on Robotics and Automation*, Auckland, New Zealand, November 2002. ARAA.

[47] Stergios I. Roumeliotis, Andrew E. Johnson, and James F. Montgomery. Augmenting inertial navigation with image-based motion estimation. In *IEEE International Conference on Robotics and Automation (ICRA)*, Washington, DC, 2002. IEEE.

[48] Srikanth Saripalli, James F. Montgomery, and Gaurav S. Sukhatme. Vision-based autonomous landing of an unmanned aerial vehicle. In *International Conference on Robotics and Automation*, pages 2799–2804, Washington DC, May 2002. IEEE.

[49] Bruno Sinopoli, Mario Micheli, Gianluca Donato, and T. John Koo. Vision based navigation for an unmanned aerial vehicle. In *IEEE International Conference on Robotics and Automation (ICRA)*. IEEE, 2001.

[50] R. C. Smith and P. Cheeseman. On the respresentation and estimation of spatial uncertainty. *International Journal of Robotic Research*, 4(5), 1986.

[51] S. Thrun and Y. Liu. Multi-robot SLAM with sparse extended information filers. In *Proceedings of the 11th International Symposium of Robotics Research (ISRR'03)*, Sienna, Italy, 2003. Springer.

[52] Sebastian Thrun, Wolfram Burgard, and Dieter Fox. A real-time algorithm for mobile robot mapping with applications to multi-robot and 3d mapping. In *IEEE International Conference on Robotics and Automation (ICRA)*, San Francisco, CA, 2000. IEEE.

[53] Sebastian Thrun, Dieter Fox, and Wolfram Burgard. *Probabilistic Robotics*. MIT Press, September 2005.

[54] R. van der Merwe and E. Wan. The square-root unscented Kalman filter for state and parameter-estimation. In *IEEE International Conference on Acoustics, Speech and Signal Processing*, Salt Lake City, UT, 2001. IEEE.

[55] Rudolph van der Merwe, Eric Wan, and Simon Julier. Sigma point Kalman filters for nonlinear estimation and sensor fusion: Applications to integrated navigation. In *AIAA Guidance, Navigation and Controls Conference*, Providence, RI USA, August 2004. American Institute of Aeronautics and Astronautics.

[56] Thomas P. Webb, Richard J. Prazenica, Andrew J. Kurdila, and Rick Lind. Vision-based state estimation for uninhabited aerial vehicles. In *AIAA Guidance, Navigation and Control Conference*, San Francisco, California, August 2005. American Institute of Aeronautics and Astronautics.

[57] Stefan B. Williams, Gamini Dissanayake, and Hugh Durrant-Whyte. Field deployment of the simultaneous localisation and mapping algorithm. In *15th IFAC World Congress on Automatic Control*, Barcelona, Spain, June 2002.

[58] Allen D. Wu, Eric N. Johnson, and Alison A. Proctor. Vision-aided inertial navigation for flight control. In *AIAA Guidance, Navigation and Control Conference*, San Francisco, California, August 2005. American Institute of Aeronautics and Astronautics.